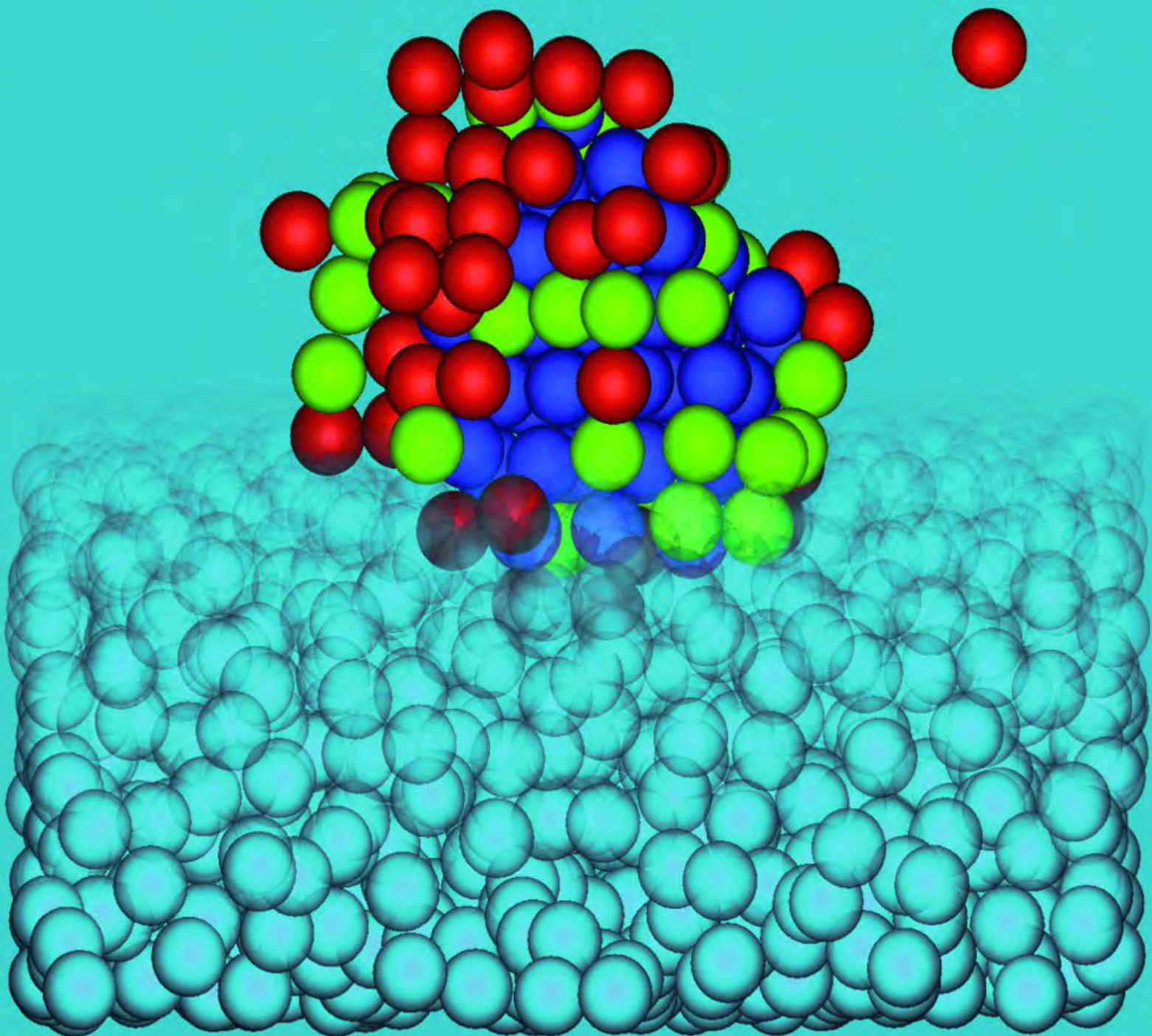


Hard Spheres out of Equilibrium



Michiel Hermes

Hard spheres out of equilibrium

Cover: Hard sphere crystal nucleus.

PhD thesis, Utrecht University, the Netherlands, May 2010.

ISBN: 978-90-393-5363-9

A digital version of this thesis is available at <http://www.colloid.nl>

Hard spheres out of equilibrium

Harde bollen uit evenwicht

(met een samenvatting in het Nederlands)

Proefschrift

ter verkrijging van de graad van doctor aan de Universiteit Utrecht op gezag van de rector magnificus, prof. dr. J.C. Stoof, ingevolge het besluit van het college voor promoties in het openbaar te verdedigen op maandag 31 mei 2010 des middags te 2.30 uur

door

Michiel Hermes

geboren op 7 oktober 1980 te Nijmegen.

Promotoren: Prof. dr. A. van Blaaderen
Prof. dr. ir. M. Dijkstra

Contents

1	Introduction	1
1.1	Colloidal hard spheres	1
1.2	External fields	2
1.3	Simulations	3
1.4	Glasses	4
1.5	Order parameters	6
1.5.1	Crystalline particles	6
1.5.2	Different domains	9
2	Thermodynamic signature of the dynamic glass transition	11
2.1	Introduction	12
2.2	Method	13
2.3	Results	13
2.4	Conclusion	18
2.5	Acknowledgments	18
3	Jamming of polydisperse hard spheres	19
3.1	Introduction	20
3.2	Methods	21
3.3	Results	21
3.4	Conclusion	27
3.5	Acknowledgments	29
4	Compression of hard spheres by gravity and electric field gradients	31
4.1	Introduction	32
4.2	Methods	33
4.3	Results and Discussion	35
4.3.1	Averaging out the effects of gravity	35
4.3.2	Influence of gravity	37
4.3.3	Slowly growing crystals	40
4.4	Conclusion	40
5	Homogeneous nucleation	43
5.1	Introduction	44
5.2	Methods	46
5.2.1	Classical nucleation theory	46
5.2.2	Order Parameters	46

5.2.3	Molecular Dynamics	47
5.2.4	Umbrella Sampling	48
5.2.5	Kinetic prefactor	49
5.3	Results	50
5.3.1	Gibbs free energy barriers	50
5.3.2	Nuclei	51
5.3.3	Kinetic prefactor	53
5.3.4	Rates	54
5.4	Conclusions	57
5.5	Acknowledgements	57
6	Nucleation on configurable seed structures	59
6.1	Introduction	60
6.2	Methods	61
6.3	Results	62
6.4	Conclusion	69
6.5	Acknowledgements	70
7	Shear induced order	71
7.1	Introduction	72
7.1.1	Steady shear	73
7.1.2	Oscillatory shear	73
7.2	Methods	75
7.3	Results	77
7.3.1	Sliding layer and twin FCC phase	77
7.3.2	String phase and tilted layer phase	82
7.3.3	Non equilibrium phase diagram	85
7.4	Conclusions	86
7.5	Acknowledgements	87
8	Depletion forces between spherical particles with a rough surface	89
8.1	Introduction	90
8.2	Model and effective interactions	92
8.3	Results	96
8.3.1	Effect of surface coverage	97
8.3.2	Effect of polymer size	97
8.3.3	Rough dumbbells	99
8.3.4	Effect of charge stabilization	101
8.4	Conclusion	103
8.5	Acknowledgements	103
	References	105
	Summary	114
	Samenvatting	116

Dankwoord	118
Curriculum Vitae	119

Introduction

Hard-sphere systems are one of the simplest systems for studying interacting particles (off lattice). Their equilibrium phase behaviour can be fully described with a single parameter: the density. In this thesis the density is measured as η , the fraction of the volume that is occupied by the particles. This volume fraction is then $\eta = V_{\text{particles}}/V_{\text{total}}$, where V_{total} is the volume of the system and $V_{\text{particles}}$ is the total volume of all the particles. At low volume fractions the equilibrium phase is a fluid phase and at high volume fractions the equilibrium phase is a face-centered-cubic (FCC) crystal. The stable fluid and solid phases are separated by a two-phase region with $\eta = 0.494$ and $\eta = 0.545$ the volume fractions of the coexisting fluid and FCC phase respectively [1].

The equilibrium behaviour of this very simple hard-sphere system is well understood, however, the non-equilibrium behaviour is not. There are several interesting dynamical regions in the hard-sphere system. The first one, which we discuss in chapter 2, is the dynamic glass transition. In chapter 3, we show that the dynamic glass transition is connected with the jamming of the random close packed states at infinite pressure. In these two chapters, we used polydisperse hard spheres to avoid crystallization. In chapter 4, we investigate another interesting dynamic property of the hard-sphere system, namely crystal nucleation and specifically the crystal nucleation rate. We seed the nucleation with a template and study the nucleation and growth of the crystal on this template in chapter 5. In chapter 6, we investigate both nucleation and the glass transition in an experiment where we vary the compression speed. We drive the system out of equilibrium using oscillatory shear and investigate what the effect of shear is on the phase behaviour and on the dynamics of nucleation and melting in chapter 7. Finally, chapter 8 is on a slightly different subject than the dynamics of hard spheres. Here we calculate the effect of roughness on the depletion interaction between hard spheres in the presence of polymers.

1.1 Colloidal hard spheres

Colloidal suspensions consist of particles, which are suspended in a medium of a different material. This medium does not have to be a liquid, for example smoke particles can also be regarded as colloidal particles. The particles do not have to be solid as for example oil

droplets in water or water droplets in air can also be considered as colloidal. Colloids have to be much larger than the particles (molecules) of the medium such that the medium can be regarded as a continuous background. The maximum size of colloids is basically given by the patience of the experimentalist and the strength of any external force. Colloids have to be sufficiently small so that due to their kinetic energy the particles can explore phase space within the available time. Usually people give a size range for colloidal particles of several nanometers to several micrometers. For example a glass marble will simply fall to the bottom of a pool of water and lay still without any significant Brownian motion within any reasonable time. But if a 1 cm glass marble in water is placed in space such that gravity does not play a role and the marble could be followed for ten thousand years it would on average have moved approximately one diameter. These thermal movements are essential for colloids as a model system, since these allow the particles to explore phase space and to reach thermal equilibrium.

Colloids are ubiquitous in everyday life. They appear in blood, milk, paint, clay, fog, smoke and cosmetics. Colloids appear in all shapes imaginable from rod shaped viruses and spherical emulsion droplets, to plate shaped clay particles and everything in between. Colloidal crystals also appear in nature; opals are the most beautiful example.

The interactions between colloids can be from nearly hard to very long range. The most common interactions are hard core repulsion, electrostatic interactions, Van der Waals attraction, steric interactions and entropic forces resulting from the solvent. In this thesis we try to keep our colloids as close to hard spheres as possible, with the exception of the last chapter. In our experiments we reduce the effects of the inevitable charge of our colloids, by adding salt to the solvent. The charged salt ions in the solvent screen the charges on the particles resulting in a short ranged interaction. The colloids we use in this thesis are stabilized by a steric layer of polymers grafted on their surface. This layer of polymers is needed to keep the colloids stable against aggregation by the Van der Waals attraction. In the last chapter we consider what happens when non-adsorbing polymers are added to the solvent. We investigate theoretically how the short range attraction induced by the polymers can be reduced by making the surface of the colloids rough.

The movement of colloids is determined by the collisions with the solvent molecules. These collisions cause the colloids to have Brownian motion. The time scales on which colloids move can be tuned by modifying the size of the colloids and the viscosity of the solvent. The time scales can be tuned such that the interesting behaviour takes place on time scales which are within the experimentally accessible time window. When the colloids are large enough, individual colloids can be observed in a regular light microscope. When the refractive index of the solvent is close to that of the particles, a fluorescently dyed particle can be observed in three dimensions using a confocal microscope. The ability to observe the dynamics of individual particles in three dimensions combined with the well-controlled interactions make colloids an interesting model system.

1.2 External fields

Due to the size of colloids, external fields have a large effect on their behaviour. For example, the gravitational energy colloids gain by sedimenting one diameter is easily on

the order of the thermal energy, while for atoms and small molecules this can only be achieved at extremely low temperatures. This is both an advantage and a disadvantage of colloids. The sensitivity to external fields offers opportunities to control and manipulate colloids. However, sometimes experiments need to be performed in space to obtain results which are not influenced by gravity.

Electric fields can also be used to manipulate colloids. When colloids with a dielectric constant different from that of the solvent are placed in an external field they acquire a dipole moment parallel to the field. When the dipole moment is strong the colloids form strings and body-centered-tetragonal (BCT) crystals [2, 3]. When the electric field is not homogeneous there is also a force pushing the colloids towards or away from regions of high field strength [4]. This effect is used in chapter 4 and 6 to compress a colloidal dispersion in a controlled manner.

When the solvent and the particles have a sufficiently different refractive index they can also be manipulated using light. When light travels through a particle with a refractive index different from that of the solvent it is deflected and consequently transfers part of its momentum to the particle. This can be used to trap particles in the focus of a laser beam [5]. This is in principle the same effect as the effect described in the previous paragraph but now using the electromagnetic field of the laser. This is used in chapter 6 to produce seed structures in the bulk of a supersaturated fluid.

1.3 Simulations

Various simulation techniques were used throughout this thesis. Monte Carlo simulations were used to investigate the equilibrium behavior, Molecular Dynamics (MD) and kinetic Monte Carlo simulations were used to investigate the dynamics. Here we discuss these methods briefly and explain the differences between the methods.

Metropolis sampling Monte Carlo (MC) simulations are simulations in which the phase space is sampled according to the Boltzmann weight. The route through phase space that the system follows is determined by random moves from one point in phase space to another point in phase space. These random moves through phase space can resemble normal dynamics but they can also contain unphysical moves in which for example a large number of particles is moved at once or two particles are interchanged. Monte Carlo simulations can be performed in different statistical ensembles, in this thesis only two different ensembles have been used: the NVT and the NPT ensemble. More details about MC simulations and different ensembles can be found in references [6, 7].

MC simulations only sample according to the Boltzmann weight when they are run long enough that they are equilibrated and have had the chance to sample a sufficiently large part of phase space. When the initial configurations are not drawn according to the Boltzmann distribution the simulations can get stuck in a metastable state for a very long time. This is, for example, the case for a slightly supersaturated hard-sphere fluid that is separated from the solid by a high free energy barrier. When a crystal nucleus is formed in the supersaturated fluid the system gains free energy from the bulk of the nucleus but the formation of the interface between the solid and the fluid costs free energy. The surface grows with the radius of the nucleus squared whereas the volume grows with the

radius cubed so for large clusters the volume term always overcomes the surface term. If the system is in a well defined metastable state Monte Carlo simulations can still be used to sample the properties of the metastable phase.

Rare events such as the formation of a critical nucleus are not sampled efficiently in a Metropolis Monte Carlo simulation because the simulation spends most of its time in the metastable fluid phase. To obtain a good sampling over these unlikely configurations an umbrella sampling simulation can be used. In umbrella sampling MC simulations a bias potential is added to the real potential to force the simulation to spend time in interesting parts of phase space. All quantities measured should then be weighted with the inverse Boltzmann weight of the bias potential to obtain the value for the unbiased simulation [8].

To investigate the dynamics two simulation techniques are used in this thesis. When Metropolis sampling MC simulations are performed with only single particle displacements with small steps Δt it is called kinetic Monte Carlo [9]. When the limit of the step size $\Delta t \rightarrow 0$ is taken, the simulations resemble Brownian dynamics and can be used to investigate the dynamics of Brownian particles in the absence of hydrodynamics. Molecular Dynamics simulations are simulations of particles (molecules) in vacuum. The difference with the previous simulation techniques is that a particle will not exhibit Brownian motion but ballistic motion between interactions with other particles. The advantage is that MD is very fast for hard particles compared to BD. Technically Brownian dynamics is impossible to simulate for perfect hard spheres. When MD is used to simulate colloids a thermostat can be used to obtain Brownian-like dynamics, however, a lot of the speed advantage is lost when a realistic time scale is chosen for the collision frequency of the thermostat.

The equilibrium crystal structure of hard spheres is an FCC crystal. However, the HCP crystal has a free energy that is only $0.0009 k_B T$ per particle higher than the FCC crystal [10]. Both the FCC and the HCP crystal consist of hexagonal layers stacked on top of each other, they only differ in the order in which these layers are stacked. In the case of horizontal FCC layers, the layer below and the layer above one hexagonal layer are shifted with respect to each other while in HCP the particles in the layer above and below are right on top of each other. Most colloidal hard-sphere crystals have been grown too fast to sample this minute free energy difference and therefore form randomly stacked crystals.

1.4 Glasses

It is difficult to find a good definition of a glass and many different definitions are used in the literature. However, there are several characteristic properties that glasses should have according to most definitions. Firstly, glasses have long relaxation times, where long is not strictly defined and depends on the observation time. The result of this dependence on observation time is that a configuration of nanometer sized colloids can be called a metastable fluid while an identical configuration of micrometer sized colloids is called a glass. A consequence of this slow relaxation is that glasses are often very viscous. Frequently glasses are defined by a viscosity threshold which is also chosen depending on

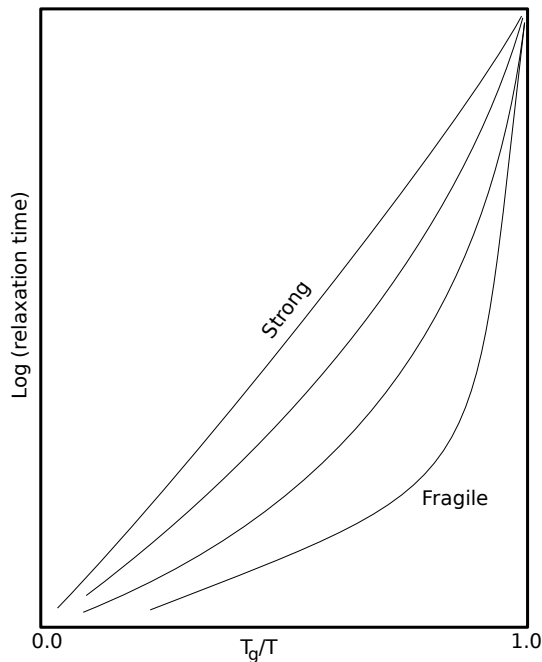


Figure 1.1: A sketch of the relaxation time or viscosity as a function of temperature relative to the glass transition temperature for strong and for fragile glasses. Some examples of glass forming liquids are SiO_2 which is a strong glass former, glycerol which is in between strong and fragile and ortho-terphenyl which is very fragile. Water is very complex and shows both strong and fragile behaviour.

the observation time.

Glasses can be categorised according to their fragility [11]. Fragile glass formers show a steep increase in relaxation times on approaching the glass transition while strong glass formers show a more gradual increase in the relaxation times when they approach the glass transition. The glass transition is most frequently defined by a viscosity or relaxation time threshold. In Fig. 1.1 we plot the viscosity as function of inverse temperature scaled to the glass transition temperature. For molecular glass formers the parameter most frequently used to approach the glass transition is the temperature but in principle a similar plot can be made for a compression quench. When the volume fraction is mapped to the temperature, colloids can also be categorised according to their glass forming behaviour. When this is done hard spheres turn out to be fragile glass formers while soft particles are strong glass formers [12].

A second characteristic of glasses is that glasses are amorphous, the crystalline order should be below a certain threshold. When a fluid that contains small regions of crystalline order, is quenched rapidly, this crystalline order remains present in the glass. In chapter 4 we discuss this transition from glass to crystal and show that there is no clear criterion to distinguish a glass from a crystal with small domains. A third, often used criterion is that a glass has to be metastable. If given enough time it should go to a different phase through a (first order) phase transition, however, the time scale on which this takes place has to be longer than the observation time. This again depends on the timescale on which

the system is studied. Many glasses crystallize when studied on geological time scales.

There exists also an ideal glass. An ideal glass has infinitely long relaxation times. This means that an ideal glass never crystallizes and that the self intermediate scattering function never decays to zero. It is unlikely that hard spheres can be made into an ideal glass at finite pressure in the thermodynamic limit. Osada has shown that the average long time diffusion of a Brownian hard-sphere system [13] at finite pressure is non zero. However, in small confined systems ideal glass states do exist in which the system can get trapped indefinitely. For example two spheres in a cubic box with hard walls are trapped in a corner already above volume fraction 0.21 (the maximum is 0.38).

The slowly changing of the properties of a glass over times is called ageing. When a glass is made by a fast temperature quench or compression the system ends up in a jammed state which can have locally very high stresses. When the glass ages these high stresses relax. When a hard-sphere system is studied at constant volume fraction the pressure drops slowly over time, whereas at constant pressure the density slowly increases over time as the glass ages. This has also been observed for dense colloidal dispersions sedimenting under gravity in which the density continually increases.

1.5 Order parameters

We used various order parameters throughout this thesis for analysing both experimental data and on simulation data. When three dimensional coordinates were available we used three dimensional bond order parameters. When we were unable to obtain reliable coordinates we calculated two dimensional order parameters Ψ_6 obtained from two dimensional data. Here we will discuss the three dimensional order parameters used in this thesis.

1.5.1 Crystalline particles

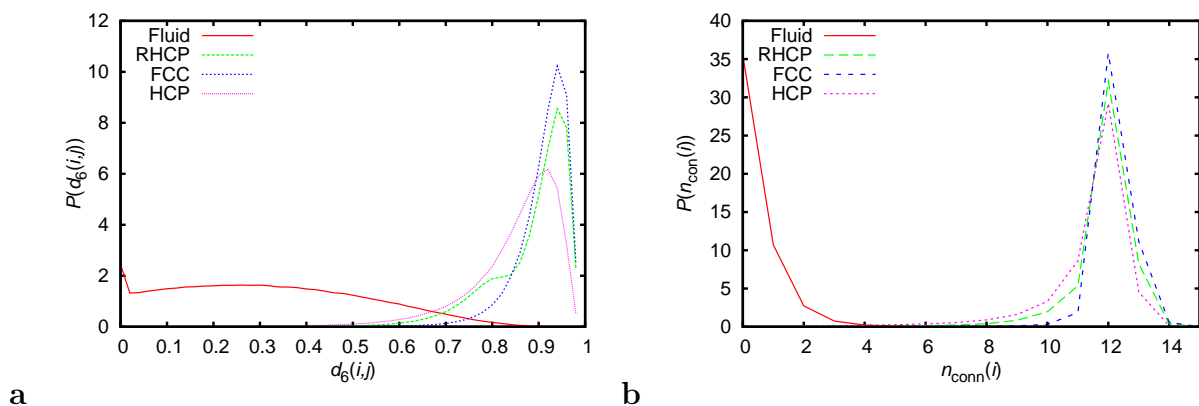


Figure 1.2: a) A histogram of the bond order correlation d_6 in different hard sphere systems of 1500-2000 particles at the coexistence pressure. b) A histogram of the number of correlated bonds n_{con} in different hard sphere systems of 1500-2000 particles at the coexistence pressure.

In nearly all of the chapters in this thesis we need to be able to distinguish fluid particles from solid particles. To determine which particles are part of a crystal and which particles are part of the fluid we have calculated the three dimensional bond order parameters $q_{l,m}$ [14]. In the calculation of the bond order parameter a list of “neighbours” is determined for each particle. The neighbours of particle i include all particles within a radial distance r_c of particle i , and the total number of neighbours is denoted $N_b(i)$. A bond orientational order parameter $q_{l,m}(i)$ for each particle is then defined as

$$q_{l,m}(i) = \frac{1}{N_b(i)} \sum_{j=1}^{N_b(i)} Y_{l,m}(\theta_{i,j}, \phi_{i,j}) \quad (1.1)$$

where $\theta_{i,j}$ and $\phi_{i,j}$ are the inclination and azimuth of the bond between i and j and $Y_{l,m}(\theta, \phi)$ are the spherical harmonics with $m \in [-l, l]$. Solid-like particles are identified [15] as particles for which the number of connections per particle $n_{\text{con}}(i)$ is greater than a critical number denoted n_{con}^c and where

$$n_{\text{con}}(i) = \sum_{j=1}^{N_b(i)} H(d_l(i, j) - d_c), \quad (1.2)$$

H is the Heaviside step function, d_c is a threshold value, and $d_l(i, j)$ is the correlation between the bond orientational order of particle i and j given by

$$d_l(i, j) = \frac{\sum_{m=-l}^l q_{l,m}(i) q_{l,m}^*(j)}{\left(\sum_{m=-l}^l |q_{l,m}(i)|^2 \right)^{1/2} \left(\sum_{m=-l}^l |q_{l,m}(j)|^2 \right)^{1/2}}. \quad (1.3)$$

To determine which cut off values work best to distinguish fluid from solid particles for a system of hard spheres we plot a histogram of the dot product $d_6(i, j)$ in Fig. 1.2a. The fluid and the random stacked crystal cross at a value of approximately 0.7. The FCC crystal has a higher value for the dot product than the HCP crystal and the random stacked crystal is as expected in between the FCC and HCP crystals. In Fig. 1.2b we plot the histogram of the number of ordered connections (as given by equation 1.2) per particle for $d_c = 0.7$. The fluid has very rarely more than 2 ordered bonds per particle. The FCC crystal has mostly 12 and rarely less than 11 ordered bonds. The HCP crystal also has mostly 12 bonds, however, the tail at low numbers of bonds is much longer than for FCC and extends towards 9 bonds per particle. When we need to choose n_c any value between 4 and 9 will successfully distinguish between a bulk fluid and a bulk solid.

To investigate the effect of the choice of n_c we measured the number of correlated bonds per particle at a liquid-solid interface. We generated a configuration in the coexistence regime in an elongated box by attaching a box containing an equilibrated RHCP crystal to a box containing an equilibrated fluid. Both the fluid and the crystal were equilibrated at the coexistence pressure in an NPT simulation. After we attached both boxes we removed overlap and equilibrated the configuration in an NVT simulation. We oriented the RHCP crystal such that the hexagonal layers are parallel to the interface. In Fig. 1.3

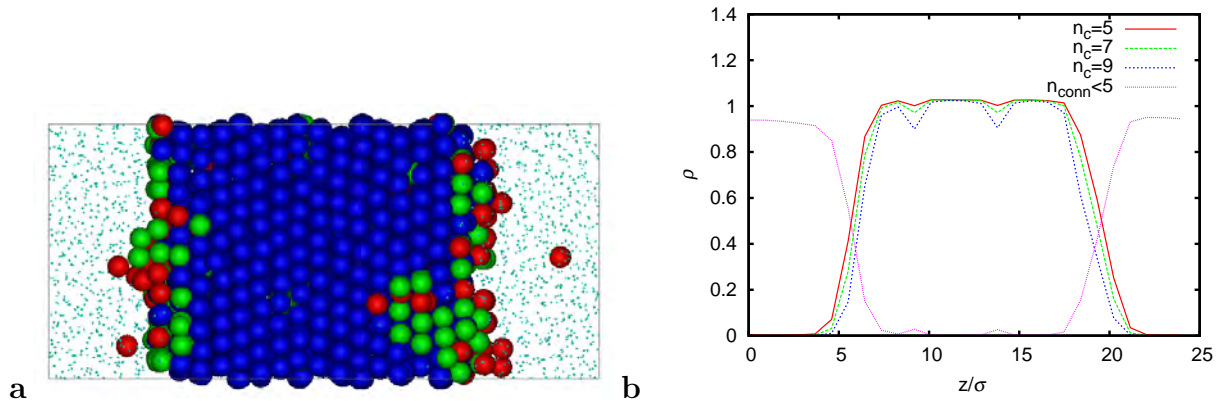


Figure 1.3: a) A snapshot of a hard sphere system of 3432 hard spheres in the coexistence regime. The middle of the box is crystalline and the rest is fluid. The blue particles have 9 or more crystalline bonds, the green particles 7 or 8 and the red particles have 5 or 6 crystalline bonds. There are two HCP stacked layers present. b) The density profile of particles with a minimum number of neighbors for different n_c . The dips correspond with HCP stacked layers.

we show a snapshot of the configuration and the crystalline particles according to three different criteria for crystallinity $n_c = 5$, $n_c = 7$ and $n_c = 9$. All three criteria succeed in distinguishing the fluid from the solid. All three criteria find roughly the same interface width but the location of the interface is shifted. The interface is shifted on average 0.5 diameters between the $n_c = 5$ and the $n_c = 9$ criteria. In Fig. 1.2 we already saw that q_6 is more sensitive to fluctuations in the HCP crystal than in the FCC crystal. The two HCP stacked layers in Fig. 1.3 are located at the two dips in the order parameter. The stricter criteria show more pronounced dips. Thus when an order parameter is required that does not discriminate between FCC and HCP a lower value of n_c is better.

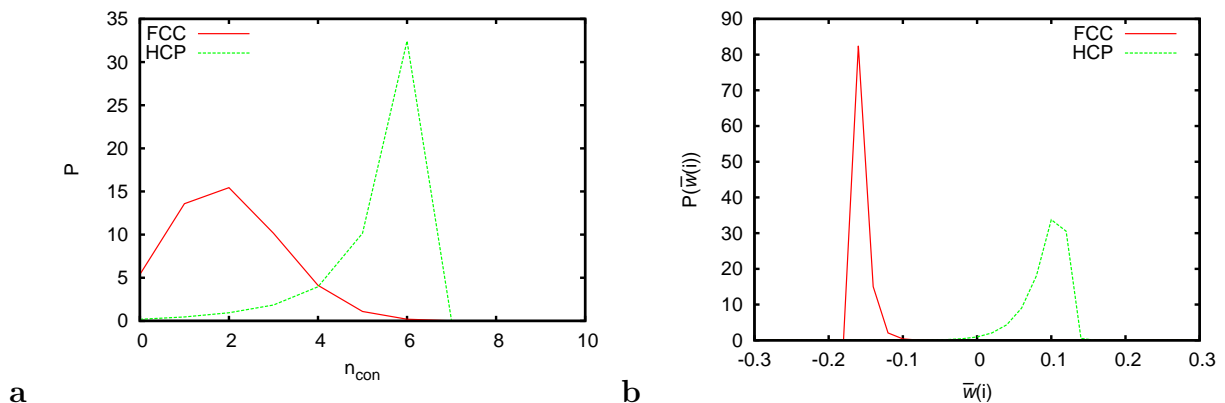


Figure 1.4: a) The distribution of n_c for an hard sphere FCC and HCP crystal using q_5 with $d_c = 0.5$ b) The separation between FCC and HCP using \bar{w}_4 .

It is often useful to be able to distinguish FCC from HCP stacked particles. We have first used q_5 correlations with parameter $d_c = 0.5$ and $n_c = 4$. More recently we used a more accurate $\bar{w}_4(i)$ criterion [16]. A crystalline particle i is identified as FCC stacked

when $\bar{w}_4(i) > \bar{w}_c$ and HCP stacked otherwise where \bar{w} is defined as follows

$$\bar{w}_l(i) = \frac{\sum_{m_1+m_2+m_3=0} \begin{pmatrix} l & l & l \\ m_1 & m_2 & m_3 \end{pmatrix} \bar{q}_{l,m_1}(i) \bar{q}_{l,m_2}(i) \bar{q}_{l,m_3}(i)}{\left(\sum_{m=-l}^l |\bar{q}_{l,m}(i)|^2 \right)^{3/2}}, \quad (1.4)$$

with

$$\bar{q}_{l,m}(i) = \frac{1}{\tilde{N}_b(i)} \sum_{k=1}^{\tilde{N}_b(i)} q_{l,m}(k), \quad (1.5)$$

and

$$\begin{pmatrix} l & l & l \\ m_1 & m_2 & m_3 \end{pmatrix}, \quad (1.6)$$

are the Wigner $3j$ symbols. The sum over $\tilde{N}_b(i)$ denotes a sum over the neighbors of particles i including the particle itself. This definition of $\bar{w}_l(i)$ is identical to the one introduced by Steinhardt [14] except that here the averaged $\bar{q}_{l,m}$ are used instead. This averaging makes this method much more robust. In Fig. 1.4 the distribution of the number of q_5 crystalline bonds and of \bar{w}_4 are shown. At coexistence the q_5 criterion has a substantial overlap between the number of bonds for FCC and for HCP while the \bar{w}_4 method has almost no overlap. All results obtained in this thesis were later checked using the \bar{w}_4 criterion with $\bar{w}_c = 0.0$ and none were found to change significantly.

1.5.2 Different domains

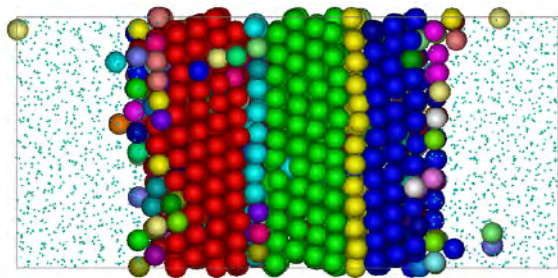


Figure 1.5: The domains of a similar configuration as used in Fig 1.3. We used $d_d = 0.91$. The three different FCC domains and the two HCP stacked layers can be distinguished.

It is often useful to be able to distinguish different crystal domains from each other. To do this we determine which particles are crystalline with the algorithm described in the previous section. After we have determined which particles are crystalline we need to find out if they belong to the same domain or not. We do this by again calculating the dot product $d_l(i, j)$ between a particle and its (crystalline) neighbors. If $d_l(i, j) > d_d$ particle i is part of the same domain as particles j . We determine this recursively for all crystalline particles until we have found all domains. The value of d_d determines the amount of order that should be present within a single domain. A disadvantage of this method is that

a single particle can connect two large domains fortunately this does not happen often. Fig. 1.5 shows the domains in a hard sphere RHCP crystal in coexistence with a fluid. The FCC domains and the HCP domains can be distinguished. The particles near the interface do not have many correlated bonds and show up as single particle domains. The colors are chosen randomly such that the large clusters all have a different color and are otherwise random.

Thermodynamic signature of the dynamic glass transition

We use extensive event-driven Molecular Dynamics simulations to study the thermodynamic, structural, and dynamic properties of hard sphere glasses. We determine the equation of state of the metastable fluid branch for hard spheres with a size polydispersity of 10%. Our results show a clear jump in the slope of the isothermal compressibility. The observation of a thermodynamic signature at the transition from a metastable fluid to a glassy state is analogous to the abrupt change in the specific heat or thermal expansion coefficient as observed for molecular liquids at the glass transition. The dynamic glass transition becomes more pronounced and shifts to higher densities for longer equilibration times.

2.1 Introduction

The amorphous or glassy state, a property of nearly all condensed matter systems, can be achieved by cooling or compressing the (supersaturated) liquid sufficiently rapidly beyond the glass transition. Glasses have a structure that is nearly indistinguishable from that of the liquid phase, but they can have dramatically different dynamical properties: molecules in a glass can move 10^{13} times slower than in a liquid phase [17]. How this is possible and whether this transition is gradual or sharp and accompanied by a structural change and diverging length scale is one of the main mysteries of glassy materials. Despite the huge amount of work devoted to glasses, the nature of the glass transition remains one of the deepest and most interesting unresolved problems in condensed-matter physics [18].

Already in the 1930-1940s, it was shown by experiments that many molecular liquids show, at the glass transition, a rather abrupt change in measured thermodynamic quantities like the specific heat, thermal expansion coefficient, and the isothermal compressibility [19]. The sudden drop in these so-called thermodynamic susceptibilities, which are directly related to thermodynamic fluctuations of the system or the long-wavelength static correlation functions, is found in many glass forming systems, although it seems to be absent or very small in some others [20]. In the liquid phase, the particles vibrate at short times in the cages formed by their neighbors, while at longer times, cooperative structural relaxation occurs. The latter relaxation slows down at the glass transition, and the corresponding fluctuations no longer contribute to the thermodynamic susceptibilities of the system. The mechanism behind the freezing out of certain degrees of freedom can be thermodynamic or dynamic of origin. The thermodynamic mechanism arises from a structural change in the system, and the dynamic mechanism occurs because the observation time is too short for the system to reach equilibrium. According to Kauzmann, one can distinguish the thermodynamic from the dynamic mechanism by prolonging the observation time and studying whether the change in the thermodynamic quantities is still present at infinitely long times [19]. Whether the glass transition is of dynamical or thermodynamic origin has been hotly debated since then and has still not been settled.

In order to understand the glass transition, many investigations have been devoted to idealized model systems in which the particles behave as hard spheres. One might suppose that the issue is settled for such a simple model by computer simulations. While early simulation studies predict a thermodynamic transition [21, 22], as there is a discontinuity in the third or second derivative of the free energy, more recent studies show no discontinuity at all [23–25]. In these recent studies, large-scale Molecular Dynamics simulations were performed for long equilibration times, while monitoring the local crystalline order to obtain well-equilibrated, truly random configurations along the metastable fluid branch. No evidence of a second order or ideal glass transition was observed for the well-equilibrated fluid state points. The existence of a thermodynamic glass transition is, on the other hand, proposed for hard spheres to avoid the paradox that the continuation of the equation of state of the stable liquid phase exhibits a divergence at unphysically high packing fractions, while one expects a divergence at random close packing ($\eta \simeq 0.64$) [26]. Experiments on colloidal hard spheres with diameter σ under earth gravity exhibit a glass transition at a volume fraction $\eta = \pi\sigma^3 N/6V \simeq 0.58$ with N the number of spheres and V the volume [27], while no glass transition is found without gravity [28, 29]. An ergodicity

breaking transition is predicted by mode coupling theory due to slow relaxation [30]. It remains an open question as to whether there is in the case of hard spheres an abrupt change in a thermodynamic quantity at the glass transition, which one would expect on the basis of molecular glasses.

In this Chapter, we use extensive computer simulations to study the thermodynamic, dynamic, and structural properties of hard sphere glasses. Our results show evidence of a thermodynamic signature, i.e., an abrupt change in the slope of the isothermal compressibility, at the dynamic glass transition. Our findings are analogous to the abrupt change that has been found in the specific heat or thermal expansion coefficients at the glass transition of molecular liquids.

2.2 Method

We consider a system of hard spheres with a Gaussian diameter distribution yielding a size polydispersity of 10% to prevent crystallization. The distribution was cut off at five standard deviations. We have checked the formation of crystalline order by measuring the crystallinity [31]. We find no sign of crystalline order or fractionation in our simulations, which allows us to study the system for long times. We stress that simulations of pure hard spheres (and smaller polydispersities) do show crystallization for packing fractions $0.52 < \eta < 0.63$ [32], and that for sufficiently long times and large system sizes, systems with a size polydispersity of 10% and $\eta > 0.54$ should partially crystallize as well [33].

We perform event driven molecular dynamics (MD) simulations with fixed volume, energy and number of particles. We measure the pressure using the virial theorem [34]. We have checked that our results for the pressure agree with the pressures obtained from the collision rate method and the value obtained from the contact value of the radial distribution function within the statistical error. For our initial configuration, we employ the mechanical contraction method, which generates densely packed and highly jammed configurations [35]. The initial velocities of the particles are randomly chosen from a Maxwell-Boltzmann distribution. The time t is measured in MD time units defined as $\sqrt{m\sigma^2/k_B T}$ where $\sigma = (\sum_{i=1}^N \sigma_i^3/N)^{1/3}$ is the average diameter, σ_i is the diameter of particle i , and m is the mass of the particles.

2.3 Results

First, we study the equation of state of the metastable liquid branch. We perform simulations of 10^3 hard spheres for varying packing fractions. We measure the pressure $\beta P(t, \eta)\sigma^3$ as a function of time and we repeat the procedure for up to 100 independent starting configurations. In Fig. 1a, we observe that the averaged pressure depends strongly on the age of the sample. The initial pressure is relatively high as the spheres are highly jammed in the initial configuration, but as the system evolves in time the particles rearrange to obtain more free volume and the pressure decreases rapidly. At a later stage, the particles diffuse less quickly as they are more caged and the pressure decays more slowly. We observe that only the short-time aging behaviour is affected by the fine details of the protocol that is used to generate the initial configurations. The results obtained from

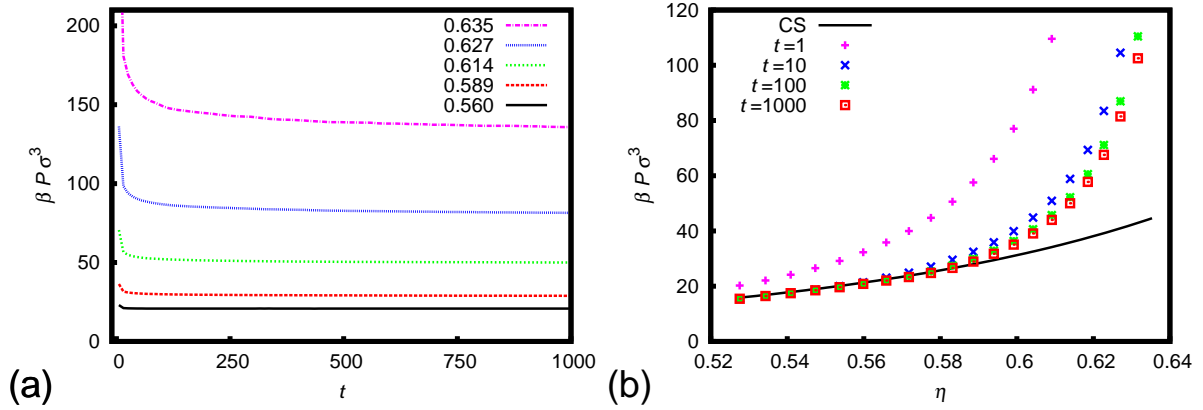


Figure 2.1: **a)** The pressure $\beta P(t, \eta) \sigma^3$ of hard spheres with a polydispersity of 10 percent as a function of t in MD time units for varying packing fraction η (as labeled). **b)** The pressure $\beta P(t, \eta) \sigma^3$ versus packing fraction η for varying time $t = 1, 10, 100, \text{ and } 1000$. The solid line denotes the Carnahan-Starling (CS) equation of state.

an initial configuration generated with the event driven Lubachevsky Stillinger algorithm [36] yield long-time behavior which is indistinguishable from the simulations started with an initial configuration generated with the mechanical contraction method.

In Fig. 1b, we plot the equation of state for different times obtained from Fig. 2.1a. For comparison, we also plot the Carnahan-Starling (CS) equation of state for pure hard spheres [37]. At low η , our simulations for polydisperse hard spheres are almost indistinguishable from CS. Surprisingly, we find a clear deviation of our pressure data from CS, which shifts to higher packing fractions and becomes sharper when the system ages.

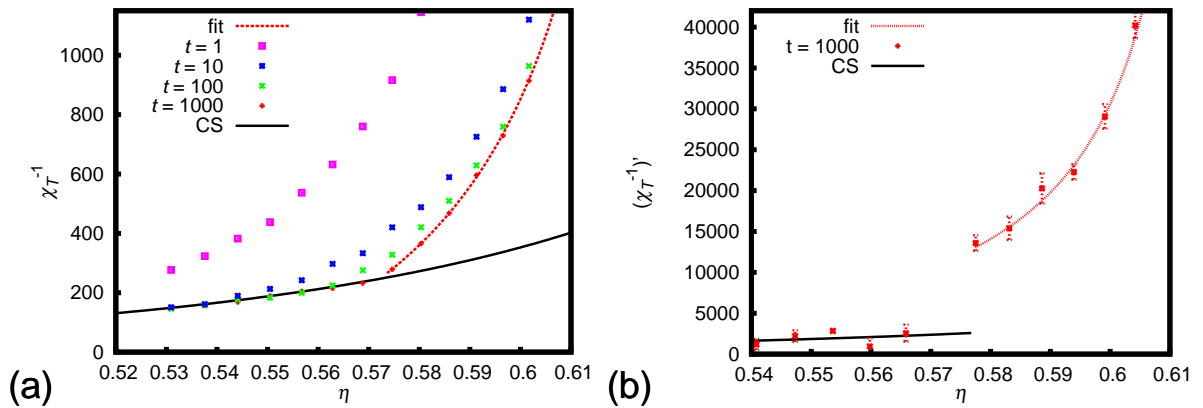


Figure 2.2: **a)** The inverse compressibility χ_T^{-1} as a function of packing fraction η for time $t = 1, 10, 100 \text{ and } 1000$. The solid line denotes χ_T^{-1} obtained from the Carnahan-Starling equation of state, the dashed lines are fits to guide the eye. The statistical error is smaller than the symbol size. **b)** The slope of the compressibility $(\chi_T^{-1})'$ as a function of η for time $t = 1000$. The solid line denotes $(\chi_T^{-1})'$ obtained from the Carnahan-Starling equation of state.

To investigate this deviation, we calculate numerically the derivative of our equation of state. The simplest form of a numerical derivative was used $df(x)/dx \approx (f(x+\Delta) - f(x -$

Δ))/(2Δ) to obtain the inverse compressibility $\chi_T^{-1} = \rho(\partial\beta P\sigma^3/\partial\rho)$ and its derivative for time $t = 1, 10, 100$ and 1000 . We plot χ_T^{-1} versus η in Fig. 2.2a. For comparison, we also plot χ_T^{-1} obtained from CS. We observe a sharp deviation from CS in the isothermal compressibility in Fig. 2.2a which becomes more pronounced and shift to higher densities for longer aging times. In Fig. 2.2b, we plot the derivative of the inverse compressibility $(\chi_T^{-1})'$ as a function of η for time $t = 1000$. We clearly observe a jump of nearly one order of magnitude in the slope of the compressibility, i.e., the third-order derivative of the free energy at $\eta \simeq 0.575$, which corresponds with the dynamic glass transition as observed experimentally [27]. The error bars were obtained by calculating the standard error of independent sets of simulations.

We wish to make a few remarks here. Instead of a jump in a second-order derivative of the free energy (e.g., the isothermal compressibility, specific heat) as in the case of many molecular glasses, we find indications of a jump in the third-order derivative of the free energy. In Ref. [21], it is speculated that the change in order of the transition is related to the absence of potential energy contributions in the case of hard spheres. The isothermal compressibility is related to density fluctuations, which consists of diffusional and vibrational contributions. At the glass transition, diffusional contributions tend to zero, and hence, the slope of the isothermal compressibility will change. For molecular glasses, potential energy fluctuations will disappear at the transition, yielding a discontinuity in the isothermal compressibility itself. It is interesting to investigate whether soft repulsive and attractive spheres yield a jump in a second-order derivative of the free energy (work along these lines is in progress). This might mean that the actual order of the dynamic glass transition is different for soft/attractive systems.

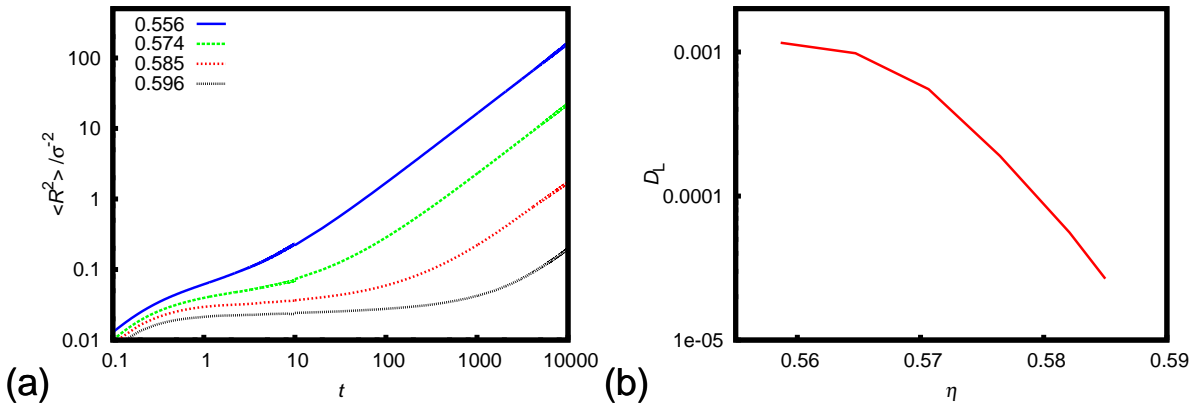


Figure 2.3: **a)** The mean squared displacement $\langle R^2 \rangle / \sigma^2$ as a function of time in MD units for waiting time $t_w = 1.10^5$ and varying packing fractions η as labeled. **b)** The long time diffusion coefficient D_L in units of $\sigma\sqrt{k_B T/m}$ as function of η obtained from the mean squared displacements.

The next question is to determine which degrees of freedom are frozen at the glass transition. To this end, we determine the mean square displacement (MSD) $\langle R^2 \rangle / \sigma^2$ with $\langle \dots \rangle$ denoting an ensemble over all particles and configurations. From the MSD we obtained the long time diffusion coefficients D_L for "aged" systems, i.e. the measurement has been carried out after a waiting time $t_w = 1 \cdot 10^5$. Fig. 2.3a shows that for sufficiently

high η the MSD develops a plateau as the structural relaxation slows down. However, the plateau is finite for all η that we tested, which is to be expected as the equilibration times for these statepoints are shorter than $t = 10^5$. Fig. 2.3b shows that D_L decreases upon increasing η , but it does not tend to zero at $\eta \simeq 0.58$, as was observed in experiments on colloidal systems in gravity [30]. Since gravity plays an important role in the formation of glasses [28, 29], the discrepancy is most likely caused by the absence of gravity in our simulations.

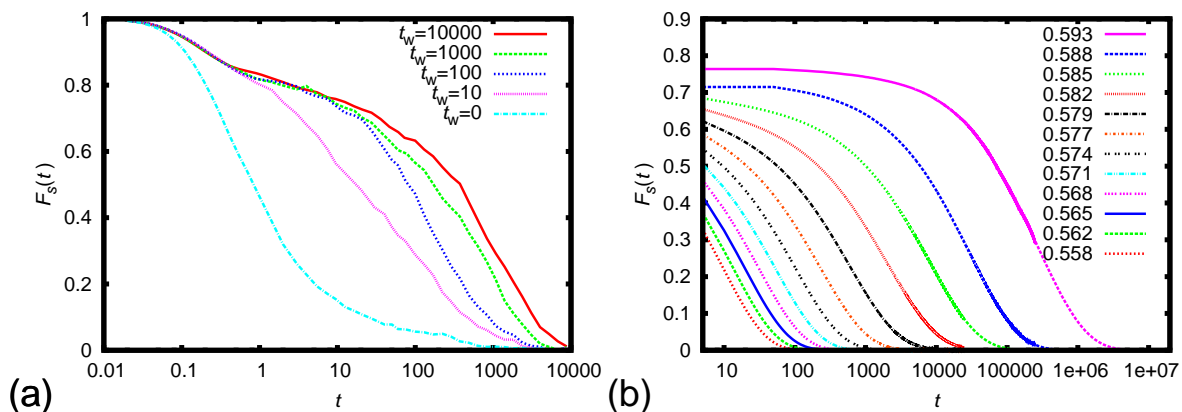


Figure 2.4: **a)** The self intermediate scattering function at a volume fraction of $\eta = 0.58$ for varying t_w (see labels). **b)** The self intermediate scattering function $F_s(t)$ for "aged" systems ($t_w = 1.10^5$ or 1.10^6) for varying η (see labels) and for $k\sigma \approx 8.2$.

In addition, we calculate the self-intermediate scattering function $F_s(t)$ for a wave vector close to the main peak of the static structure factor, i.e. $k\sigma \approx 8.2$. We perform simulations of 2000 hard spheres with a polydispersity of 10%. Fig 2.4a shows that $F_s(t)$ has a clear aging behaviour: the structural relaxation slows down dramatically for longer waiting times as the time window of the plateau of the correlation function increases. The particles get more arrested or caged upon prolonging the waiting time and the plateau in $F_s(t)$ grows in, temporal extent, when the system ages. For $\eta = 0.58$, $F_s(t)$ no longer changes between $t_w = 1.10^5$ and $t_w = 1.10^6$, and it is tempting to argue that the system reached the "equilibrium" (but metastable with respect to a fractionated crystal phase) state. In order to eliminate the aging behaviour, we perform long simulations of 1.10^7 time units. Fig. 2.4b shows $F_s(t)$ for $k\sigma = 8.2$ and varying η for "aged" systems ($t_w = 1.10^5$ or 1.10^6). We clearly observe the development of a plateau, which is characteristic of structural relaxation, but the correlation function seems to decay to zero for all η . We note that the correlation function decays to zero within $t \simeq 1000$ for $\eta = 0.58$. However, for lower values of the wave vector $k\sigma$, the relaxation of $F_s(t)$ from the plateau value becomes slower and the time window of the plateau increases in contrast with the predictions of simple mode coupling theory.

As we find a strong aging behaviour in the equation of state and its derivatives, we plot in Fig. 2.5a the packing fraction η_g corresponding to the kink in the isothermal compressibility as a function of "waiting" time. As the kink in the isothermal compressibility corresponds to a dynamic glass transition from a metastable fluid phase to a metastable glass state, one can identify the "waiting" time as the time that is required to equilibrate

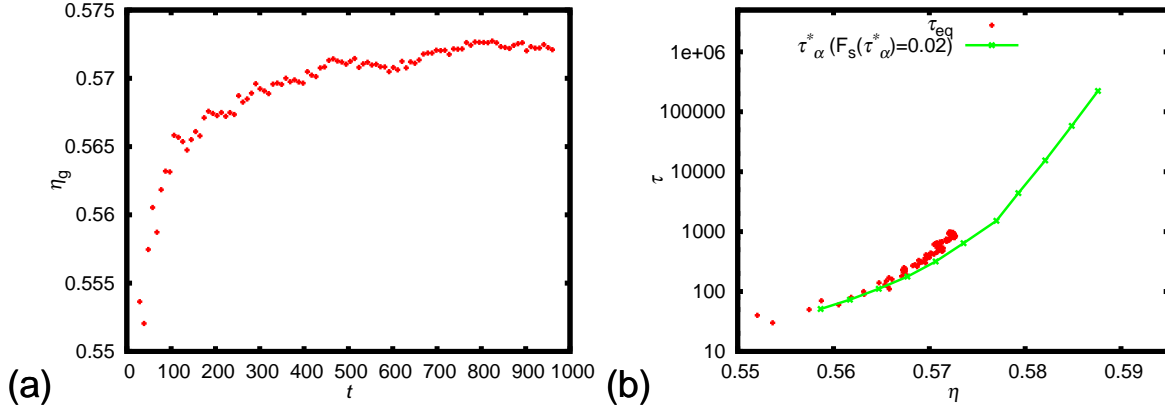


Figure 2.5: **a)** The packing fraction $\eta_g(t)$ corresponding to the kink in χ_T^{-1} as a function of time t . **b)** The equilibration time τ_{eq} and the relaxation time τ_α^* as a function of packing fraction η .

the metastable fluid at $\eta \simeq \eta_g$. Fig. 2.5b clearly shows that a longer "waiting" time is required to equilibrate a system at increasing η_g . We now compare the equilibration time with the relaxation time τ_α^* as defined by $F_s(\tau_\alpha^*) = 0.02$ for $k\sigma = 8.2$. We plot the equilibration time as a function of η along with τ_α^* in Fig. 5b. We find that the equilibration time of the system as obtained from the kink in the isothermal compressibility (see Fig. 5a) agrees well with the relaxation time as obtained from the intermediate scattering function as shown in Figure 2.4b. We note that the normal definition of the relaxation time where $F_s(\tau_\alpha) = e^{-1}$ is always lower than the equilibration time obtained from the equation of state.

In conclusion, we find a clear jump in the slope of the compressibility, which becomes more pronounced and shifts to higher densities for longer aging times. According to Kauzmann, the glass transition is of thermodynamic origin, if the change in thermodynamics remains at infinite times. A thermodynamic ideal glass transition has been predicted at a Kauzmann packing fraction $\eta_K = 0.617$ on the metastable fluid branch in Ref. [26] using the replica method. However, the existence of a thermodynamic ideal glass transition is heavily debated. Our results show a nonequilibrium glass transition at a density range of 0.55-0.59, which is far below the theoretical predictions for the ideal glass transition. This is to be expected as the relaxation time diverges on approaching the ideal glass transition [38], and hence, it is impossible to reach η_K , since already at lower densities, the fluid gets arrested in a nonequilibrium glass as the relaxation time becomes longer than the simulation time.

Although the simulations discussed here were based on polydisperse hard spheres, similar results were obtained with pure hard spheres: The pressure decays with a power law until crystallization sets in and diverges at a volume fraction that is slightly lower than the polydisperse case. At densities well below and above the glass transition we were able to obtain similar pressure data as for polydisperse hard spheres but close to the glass transition crystallization is so fast that we were not able to obtain accurate results for sufficiently long times.

The search for a structural change or a diverging length scale at the glass transition

has been going on for a long time, but has not yielded any definite results. However there is some evidence for a diverging length scale in dynamic correlation functions at the glass transition. For example, Weeks *et al.* [39] have observed experimentally that clusters of fast moving colloidal particles are much larger in the metastable fluid than in the glass and that there is a sudden drop in cluster size at the glass transition. Benneman *et al.* have found a diverging length scale of correlated motion at the glass transition in simulations of a polymer melt [39].

As we provide evidence for a clear thermodynamic signature at the dynamic glass transition, i.e. an abrupt change in the third-order derivative of the free energy, one might expect to find a structural change in one of the higher-body correlation functions when the system falls out of equilibrium. This can be understood from the virial expression that relates the pressure to the contact value of the pair correlation function. Subsequently, the first or second derivative of the pressure, i.e., the inverse compressibility or its slope, can then be expressed in terms of (the contact values of) a four-body or higher-body correlation function, respectively. In order to detect a discontinuity in the contact value of one of these higher-body correlation functions, which is a very subtle effect, one has to calculate these higher body correlations with sufficient statistical accuracy so that one can extrapolate these correlation functions to the contact value with high precision. Unfortunately, our efforts to calculate these higher-body correlation functions were not sufficiently accurate close to the dynamic glass transition that we could detect such a discontinuity in the contact value. The main problem that we encounter is that close to the dynamic glass transition, the system ages faster than that we were able to accumulate decent statistics for the correlation functions. When we try to increase our statistics by longer simulation times, the dynamic glass transition simply moves to higher packing fractions.

2.4 Conclusion

We have used extensive event-driven Molecular Dynamics simulations to study the thermodynamic, structural, and dynamic properties of hard sphere glasses. We have determined the equation of state of the metastable fluid branch for hard spheres with a size polydispersity of 10%. We demonstrated that the dynamic hard sphere glass transition has a thermodynamic signature, i.e., there is an abrupt change in the second derivative of the equation state. Hence, we have shown that the dynamic glass transition can be located by measuring the equation of state or derivatives thereof as was already known for molecular glasses. Further we demonstrated that the equilibration time of the equation of state corresponds to the relaxation time as obtained from the self intermediate scattering function.

2.5 Acknowledgments

We gratefully thank L. Berthier for stimulating discussions.

Jamming of polydisperse hard spheres

We study jammed configurations of polydisperse colloidal hard spheres with a well-defined temperature (constant kinetic energy) as a function of compression speed and size polydispersity. To this end, we employ event-driven molecular dynamics simulations at fixed temperature, using an algorithm that strictly prohibits particle overlaps. We find a strong dependence of the jamming density on the compression rate that cannot be explained by crystallization. Additionally, we find that during the compression, the pressure follows the metastable liquid branch until the system gets kinetically arrested. Our results show that further compression yields jammed configurations that can be regarded as the infinite pressure limit of glassy states and that different glasses can jam at different jamming densities depending on the compression rate. We present accurate data for the jamming density as a function of compression rate and size polydispersity.

3.1 Introduction

Colloidal hard spheres have proven their value as a model system for the study of liquids, glasses, crystals and powders. In 2005, Hales proved Kepler's conjecture that the densest packing of N identical hard spheres in a volume V is achieved by the stacking of close-packed hexagonal planes yielding a packing fraction $\eta = \pi\sigma^3 N/6V \approx 0.74$ [40]. When a colloidal system is compressed slowly it indeed forms this close-packed crystal phase [27]. However, when a system of hard spherical colloids is compressed quickly it does not reach this maximum density and it forms a jammed configuration at a lower density as further compression leads to particle overlaps or deformation [41]. Jamming phenomena are generic since atomic, colloidal and granular systems can all be jammed in a state out of equilibrium by quickly cooling, compressing or unloading [42]. In experiments on colloidal systems, which are inherently polydisperse in size, the packing fraction is often determined by centrifuging the sample and equating the packing fraction of the sediment [43–46] to the jamming or random close packing density η_{rcp} , and hence requires an accurate value of η_{rcp} .

Many authors speculate that $\eta_{\text{rcp}} \sim 0.64$ of hard spheres is well-defined [47] although its precise value is unknown. On the other hand, Torquato *et al* [48] argued that η_{rcp} is ill-defined as the jamming density depends strongly on the compression rate. These authors showed by simulations of pure hard spheres and binary hard-disk mixtures that the jamming density increases with slower compressions due to crystallization (and demixing) [24, 48]. They resolved this issue by defining a maximally random jammed state which only takes into account systems that do not have any crystalline order and find that the equation of state (EOS) of the metastable fluid diverges at $\eta_{\text{rcp}} \sim 0.644$ [49].

Crystallization can be avoided by introducing size polydispersity. In this Chapter, we study the jamming density as a function of compression rate for polydisperse colloidal hard spheres. We find that the jamming density increases by lowering the compression speed without introducing any *crystalline order* into the system in contrast with previous results [24, 48]. Moreover, our results contrasts the idea that η_{rcp} is well-defined and can be regarded as the infinite pressure limit of the metastable extension of the equilibrium liquid branch [47–49].

Others made the assumption that jammed configurations can be regarded as the infinite pressure limit of glassy states [26, 50–52]. Speedy [51] showed that different hard-sphere glasses can be generated with different jamming densities due to irreversible relaxation. Recent simulations on binary hard-sphere mixtures also confirm this assumption [53, 54]. To investigate whether our observed range of jamming densities can be explained by the idea that different glasses jam at different densities, we monitor the pressure during compression. Our results provide evidence that jammed configurations of polydisperse hard spheres can be regarded as the infinite pressure limit of glassy states and that indeed different glasses can be formed for different compression rates that jam at varying jamming densities.

Additionally, we give accurate data for the jamming density as a function of compression rate and size polydispersity, which is important for experiments on colloidal systems, where the packing fraction is often determined by equating the packing fraction of the centrifuged sediment to η_{rcp} obtained from simulations [55, 56]. However, it was already

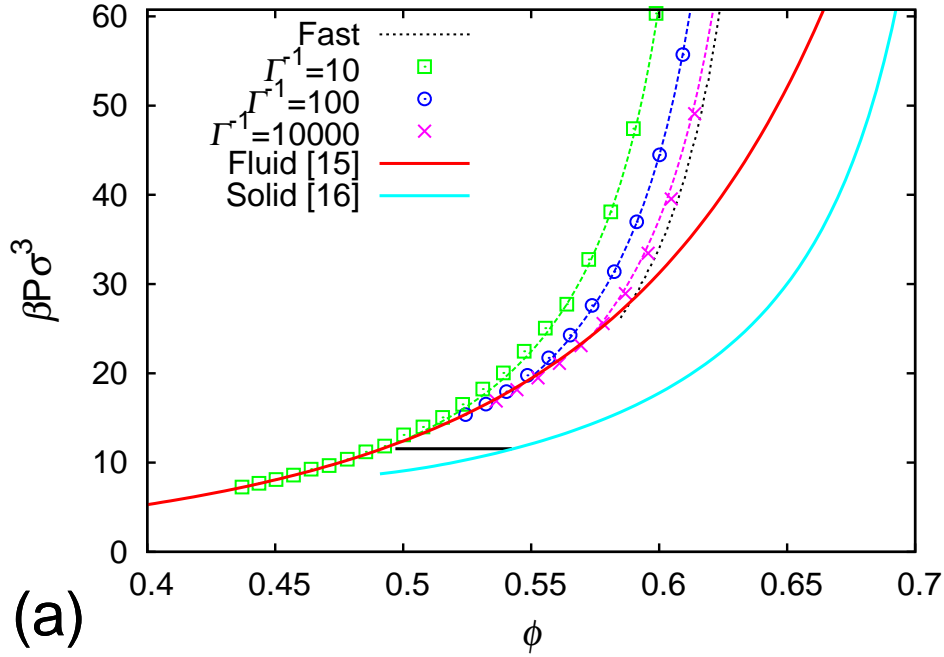
pointed out in [57] that these simulation results are inaccurate, thereby casting doubts on the determination of the volume fractions in these experiments [43–46]. Additionally, these simulations do not take any compression rate (or centrifugal speed) dependence into account. As our results show that the jamming density strongly depends on the compression rate, we denote the density of the jammed configuration with η_J rather than the random-close-packing density η_{rcp} . We also note that jammed configurations are defined here as infinite pressure states as further compression would result in particle overlaps; it does not mean that particles can not displace anymore or can not move collectively.

3.2 Methods

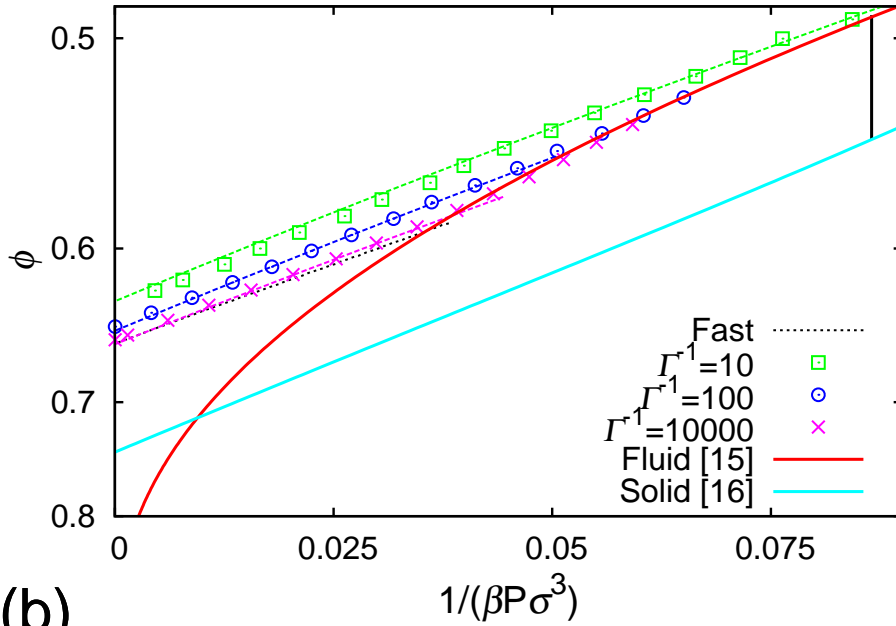
As the focus of our work is on colloidal hard spheres with a well-defined temperature, and where the particles cannot be deformed or overlap, we restrict ourselves to simulations that strictly prohibits particle overlaps. In addition, we kept the temperature and hence, the kinetic energy of all particles fixed. This is an important difference with the work on soft particles [58–60]. To this end, we perform event-driven Molecular Dynamics MD simulations using the Lubachevsky-Stillinger algorithm [36]. Modifications were made to fix the temperature of the system and to define a compression rate $\Gamma = d \sigma \rho^{1/3} / dt$, where we use the MD time as our unit of time [61]. The temperature was kept constant by monitoring the build up of kinetic energy and by rescaling the particle velocities. When we rescaled the velocities we also rescaled the system size such that the average diameter of the particles was kept fixed. So the algorithm runs for a certain number of collisions while the temperature rises and the particles grow. The algorithm was adapted to keep the polydispersity constant during the particle growth [62]. When the temperature of the system rises too much or the particles become too large, the system is rescaled to the desired temperature and particle sizes. The polydispersity was sampled from a log-normal distribution, which is nearly identical to a normal (Gaussian) distribution for small polydispersities, but has the advantage that it is zero for negative diameters.

3.3 Results

We determine the EOS from simulations of 2000 particles with a size polydispersity of 10%. We average our results over 50 different runs. To check for finite size effects we perform simulations with up to 2×10^5 particles and we find good agreement within the statistical accuracy. We plot the EOS for varying Γ in Fig. 3.1a along with the equilibrium Carnahan-Starling (CS) EOS for the fluid [63] and the EOS of the solid phase [51]. During the simulations with 10% polydispersity, we carefully checked for crystallization, but we did not find any crystalline order in any of our compression runs. The global bond-orientational order parameter Q_6 remains < 0.02 during compression for all Γ , and the pressure does not show any drops that correspond with partial crystallization. We also calculated local and global Q_4 , Q_6 and Q_8 bond-orientational order parameters, which did not show any local and global crystalline order. Additionally, the spatial correlation function of Q_6 [31] did not detect any crystalline clusters. We also checked for demixing by calculating the number of particles that are smaller or larger than the averaged size around



(a)



(b)

Figure 3.1: **a)** Pressure $\beta P \sigma^3$ as a function of packing fraction η for a system of hard spheres with 10% size polydispersity and for varying compression rates Γ as labeled. The dotted black line is a fast compression of a well-equilibrated fluid of $\eta = 0.585$. The red and blue (dark and light solid) lines denote the equilibrium equation of state for the fluid and solid phase [51, 63], respectively, while the horizontal line denotes fluid-solid coexistence. The dashed lines denote the fits to the simulation data (symbols) using Eq. (1). **b)** As in **a)** but now plotted as a function of η and $1/(\beta P \sigma^3)$ so that the infinite pressure limit is clearly visible.

each particle during the simulation. As this number remains constant, we conclude that we did not find any sign of demixing. The pressure initially follows the equilibrium CS-EOS of the metastable fluid phase until the system becomes kinetically arrested as the relaxation time of the system exceeds the compression rate. At this density, the pressure increases much faster than that of the equilibrium fluid EOS upon further compression. The density of the jammed configuration at infinite pressure increases with slower compressions. The reason is that the system has more time to equilibrate for slow compressions, and hence the system falls out of equilibrium at a higher density on the metastable fluid branch. Further compression of this glass phase yields a higher jamming density. Therefore we find a finite range of jamming densities depending on Γ . Our results provide strong support that jammed configurations can be identified with the infinite pressure limit of glassy states and that different glasses can be generated as a function of compression rate that jam at different densities. We note that Fig. 3.1a shows remarkable resemblance to Fig. 7 of [54], where the existence of multiple EOS for the unequilibrated binary hard-sphere glasses has been established, all diverging at different jamming densities. In addition, they construct a one-to-one correspondence between the density where the system falls out-of-equilibrium and the density where the pressure diverges by equilibrating metastable fluid configurations at various initial densities and compressing them rapidly to very high pressures so that structural relaxation is prevented. In this work, we keep the compression rate fixed during the compressions as this is closer to the experimental conditions of colloidal systems. Appreciable relaxation and aging behaviour might be expected during our compressions when the system departs the equilibrium EOS. However, we do not find any noticeable effect on the jamming density if we increase the compression rate when the system leaves the equilibrium liquid branch.

The concept of multiple glasses is well known for molecular glasses [64]. Indeed, Fig. 3.1a resembles the picture that is found for molecular glasses with η and $1/(\beta P\sigma^3)$ playing the role of the inverse of the specific volume and the temperature, respectively. To this end, we plot our results in Fig. 3.1b in the $\eta - 1/(\beta P\sigma^3)$ representation, where $\beta = 1/k_B T$ with k_B Boltzmann's constant. We now find striking similarities with the sketched phase diagrams in Refs. [26, 52]. Theoretical calculations using the replica method [26] predict also that different glasses can jam at different densities upon compression, and that the pressure of the glass phase close to jamming is well-described by a power law $\beta P/\rho \propto 1/(\eta_J - \eta)$ with η_J the jamming density at infinite pressure [26]. We observe in Fig. 3.1b an almost linear behavior for the inverse pressure as a function of η for the glass phase, which we can fit remarkably well as shown in Fig. 3.1 over the full range using the free volume scaling [47]:

$$\beta P\sigma^3 = a \frac{\eta_J^{1/3} \eta^{2/3}}{(\eta_J/\eta)^{1/3} - 1}, \quad (3.1)$$

where a and η_J are fitting parameters. The leading order term of Eq. (1) yields the power law as predicted in [26] close to jamming. In addition, the theory predicts an ideal glass transition at a Kauzmann packing fraction $\eta_K = 0.617$ on the metastable fluid branch, yielding a jammed configuration upon compression of this ideal glass with a random close packing density of $\eta_{\text{rcp}} = 0.683$ [26]. However, the existence of a thermodynamic ideal glass transition is heavily debated. We note that our results do not depend on the (non-

)existence of such a glass transition. Our results show a nonequilibrium glass transition at a density range of 0.50-0.59, which is far below the theoretical predictions for the ideal glass. This is to be expected as the structural relaxation time diverges on approaching the ideal glass transition [54]. Hence, it is impossible to reach η_K , since already at lower densities, the fluid gets arrested in a nonequilibrium glass as the relaxation time becomes longer than the simulation time.

In order to investigate the divergence of the structural relaxation time on approaching η_K , and to estimate what the maximum density is at which we can still equilibrate a state on the metastable fluid branch, we perform constant volume simulations of a system of 2×10^4 spheres with 10% size polydispersity and varying η . We start our runs with an initial configuration obtained from a fast compression. Fig. 3.2 shows the pressure difference with respect to the CS-EOS as a function of time. We clearly observe that the pressure initially decays towards an intermediate state for all η . Subsequently, large collective rearrangements are required to relax the system further. Finally, we observe that the pressure reaches the value predicted by the equilibrium CS-EOS. The time scale for the system to equilibrate to the equilibrium fluid phase is comparable to the relaxation time τ_α that can be determined from the self-part of the intermediate scattering function $F_s(q, t)$, where we define τ_α by $F_s(\tau_\alpha) = 0.1$ for $q\sigma = 6.5$. In Fig. 3.2b we plot $F_s(t)$ for varying η and the inset of Fig. 3.2a shows τ_α along with the equilibration time τ defined as $\beta(P(\tau) - P_{CS})\sigma^3 = 0.1$. We clearly observe that both times are remarkably close. The equilibration time of a system with 2×10^4 particles at $\eta = 0.585$ is more than 10^5 MD steps, which is equivalent to 2 weeks on a desktop PC. The equilibration time for $\eta = 0.59$ is expected to be more than 20 weeks. Hence, the ideal glass at η_K , and the corresponding random close packing are both inaccessible. Instead the system will fall out of equilibrium into a non-equilibrium glass state at a density that depends strongly on the compression rate. Additionally, we compress at high Γ our well-equilibrated fluid configuration of $\eta = 0.585$ to very high pressures as in [54]. Fig. 1 shows that the EOS is similar to the other compression runs, providing again support that jammed configurations are infinite pressure limits of glassy states.

In order to study whether the final configurations are locally or collectively jammed, we calculate the coordination number of the final configuration of the monodisperse compression runs. To calculate the coordination number we perform a short event driven MD simulation, initialized with the final configuration of the compression run, while we keep track of the collisions of all particles. In Fig. 3.3a we plot the averaged number of neighboring particles with which each particle has collided as a function of time. For very fast compressions, the particles can still move out of their cage and collide with new particles, while for slower compressions, the cage formed by on average 6 neighbors gets tighter. Hence, it takes longer till a particle can escape out of its cage and collide with more than 6 particles. The slowest compressions result in a nearly rectangular graph where the particles can only collide with the 6 particles of its cage. As the averaged coordination number is always larger than 4 and the cage-trapping plateau of the mean square displacement is always much smaller than σ^2 , we conclude that the configurations are at least locally jammed [65].

However, for all compression speeds the particles are still able to escape their cages by collective rearrangements, although this takes longer for slower compressions. We

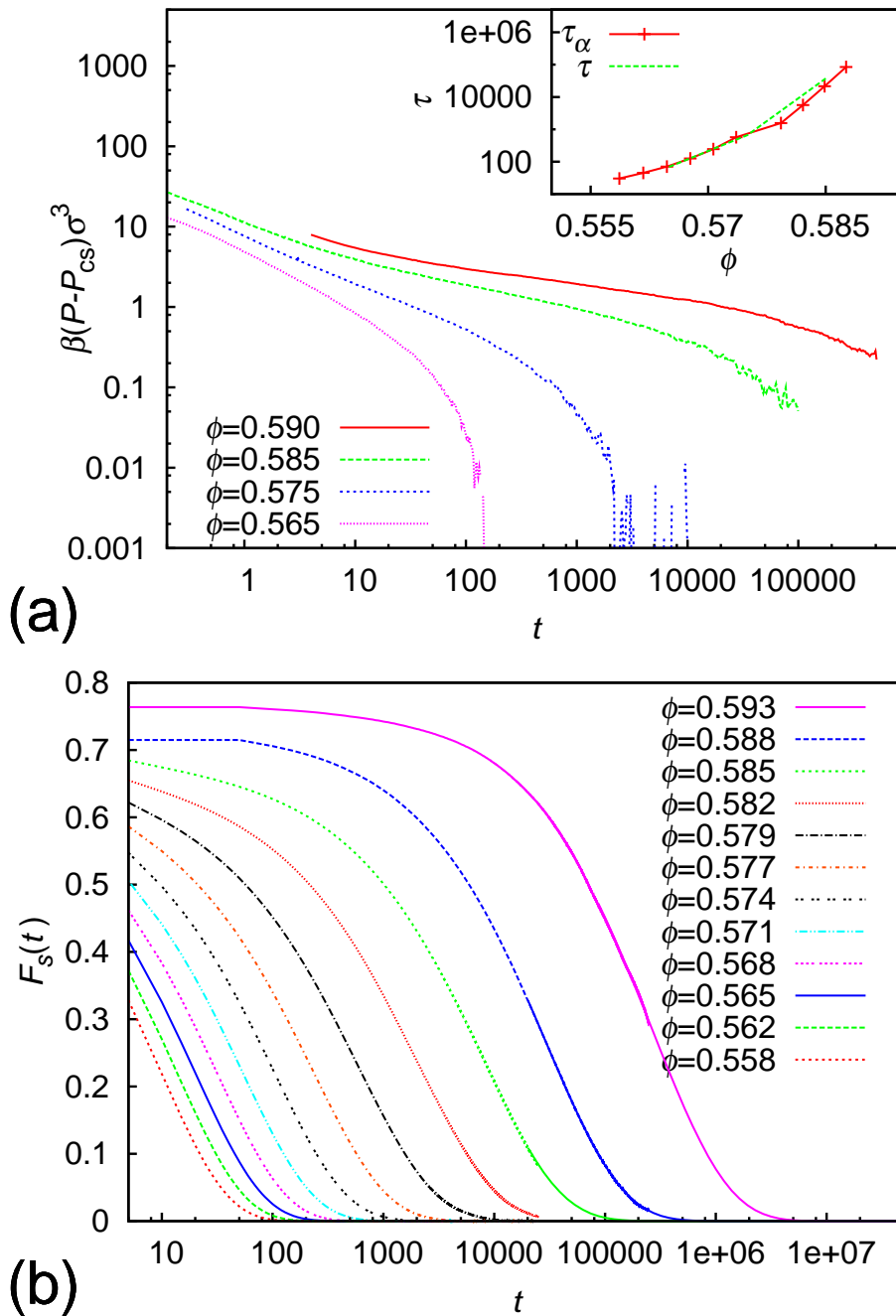


Figure 3.2: **a)** Pressure difference $\beta(P(t) - P_{CS})\sigma^3$ with respect to the Carnahan-Starling equation of state P_{CS} as a function of MD time for a system of hard spheres with 10 % size polydispersity. Inset) The relaxation time τ_α and τ of the self intermediate scattering function $F_s(t)$ and $P(t)$, respectively. **b)** $F_s(t)$ as a function of MD time.

can read of the number of particles that have escaped their cage from Fig. 3.3, when we assume that particles are caged by maximally 6 neighbors and all particles that have collided with a 7th particle have escaped their cage. The fact that we do not observe collectively jammed configurations is consistent with work of Donev et al. [66] who have

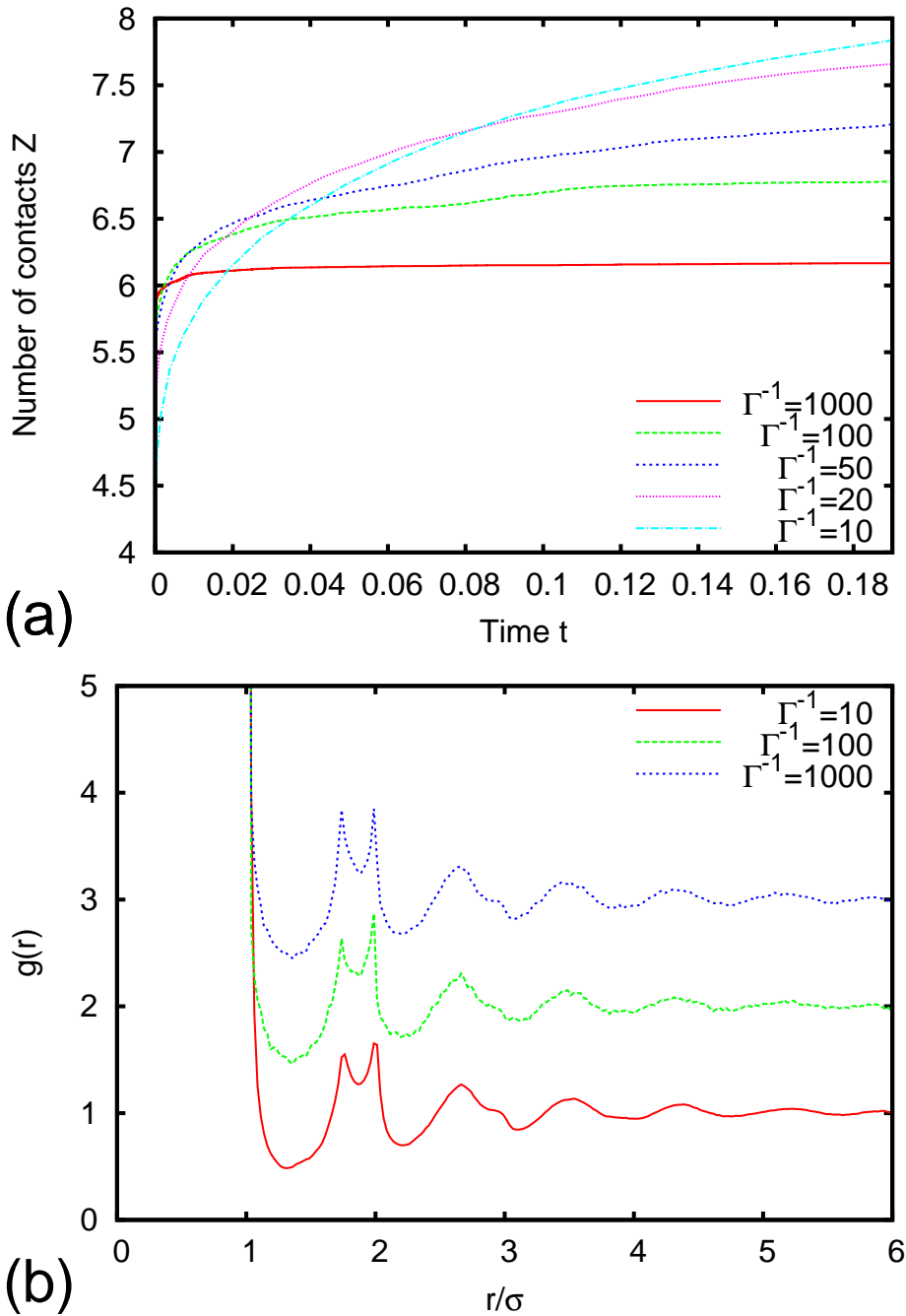


Figure 3.3: **a)** The coordination number obtained from the number of different particles a particle has collided with after time t in MD units. The simulations were started with the final configuration of a monodisperse compression run. **b)** The radial distribution functions of the final configurations of the monodisperse compression runs for varying Γ^{-1} as labeled.

demonstrated that it is difficult to generate large collectively jammed systems and H. Osada [13] and Salsburg et al. [67], who have proven that it is impossible to have an infinitely large collectively jammed system of Brownian particles at finite pressure. Our system contains 2000 particles which is most likely too large to result in a collectively

jammed configuration at the pressures we have reached.

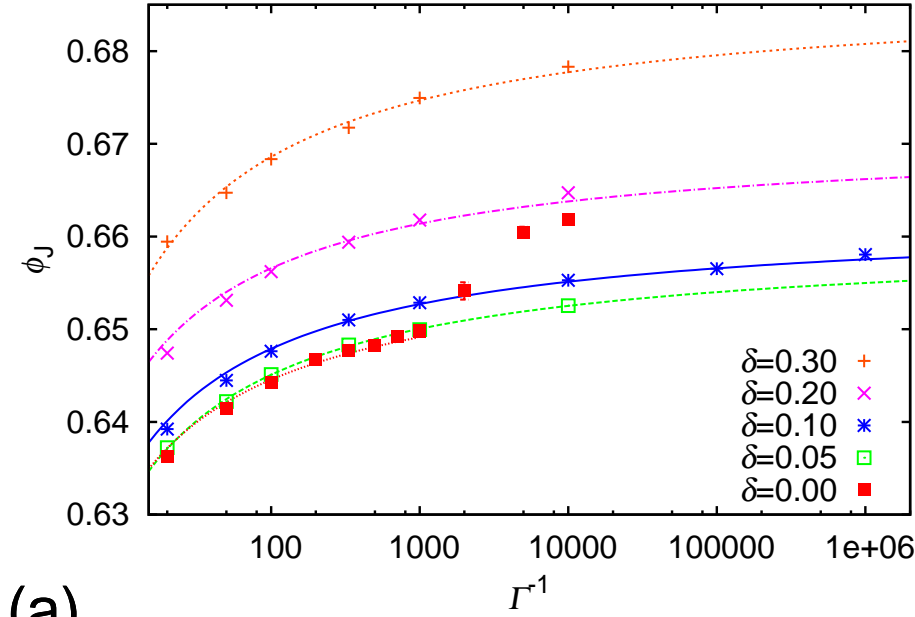
Our results differ significantly from studies on collectively jammed configurations of soft particles at temperature $T = 0$, where a well-defined jamming point or random close packing density is found in the thermodynamic limit [58, 59]. In these studies, although they might yield overlap-free final configurations, will follow a path through phase space that can not be followed by hard particles without generating particle overlaps. Recent work shows, however, that these soft particle systems yield a range of jamming densities as the compression is performed at finite temperature [60].

To investigate whether there is a structural difference between the different compression speeds we calculated the radial distribution function of the monodisperse final configurations in Fig 3.3b. The radial distribution functions of these different configurations are nearly independent of the compression speed and show all the typical features observed for dense random packings of spheres, i.e., split second peak, oscillatory decay, averaged coordination number larger than 4, etc. [68].

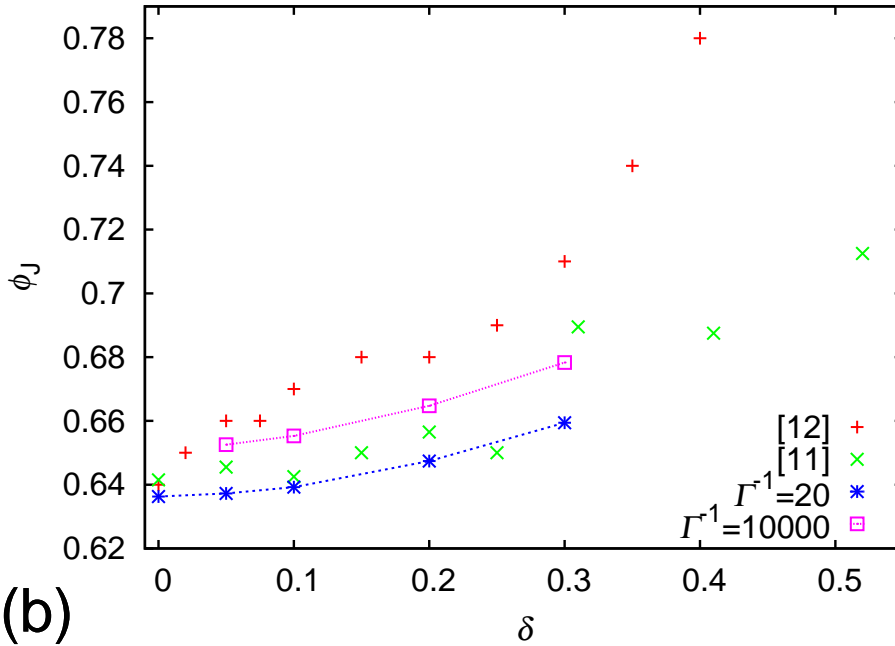
Finally, we study the jamming density as a function of Γ for several size polydispersities δ . We perform simulations of 2000 particles using varying Γ and we terminate the simulations when the time between successive collisions becomes of the same order of magnitude as our numerical accuracy, yielding $\beta P \sigma^3 \sim 10^5$ for slow compressions. To determine the jamming density η_J , we fit the EOS close to jamming (the last few volume percent) with Eq. (1). We average our results over 50 different runs. Fig. 3.4a shows η_J as a function of Γ^{-1} for varying δ . We have fitted these extrapolations with $\eta = a + b/\log(\Gamma)$, where a and b are fitting parameters. The jamming density η_J for pure hard spheres ranges from 0.635 – 0.645 for $10 \leq \Gamma^{-1} \leq 1000$. For faster compressions $\Gamma^{-1} < 10$, the simulations do not yield jammed configurations and the system (partially) crystallizes for $\Gamma^{-1} > 1000$ as can be observed in Fig. 3.4 as η_J increases rapidly, which is consistent with [48]. We also observe that η_J increases with increasing δ . For $\delta = 10\%$, we find that η_J varies from 0.638 – 0.658. As polydispersity prevents crystallization, we are now able to study η_J for five orders of magnitude of Γ . Although the slope of the curves decreases with increasing Γ^{-1} (slower compressions), it is hard to justify an extrapolation to infinitely slow compression rates. Fig. 3.4b shows η_J as a function of δ for $\Gamma^{-1} = 20$ and 10^4 . For comparison, we also plot data from Nolan [56] and Schaertl [55]. Our results are close to [56], but the results of [55], which are obtained from single runs with low accuracy, deviate from our data. The strong Γ -dependence of η_J explains the range of densities that has been found in the literature obtained by different authors and algorithms. Our results show that a size polydispersity of up to 5% does not increase the jamming density significantly from the monodisperse case. A much larger dependence on δ is often used in the experiments [43–46] based on Ref. [55], casting doubts on the precise values for the volume fractions determined in experiments via this route.

3.4 Conclusion

In conclusion, we studied the jamming density of colloidal hard spheres as a function of compression rate for a wide range of size polydispersities. As the focus of our work is on jamming in systems of colloidal hard spheres with a well-defined temperature, we



(a)



(b)

Figure 3.4: **a)** Jamming density η_J as a function of the inverse compression rate Γ^{-1} for polydispersities δ as labeled. The lines denote fits to our results (see text). **b)** η_J vs. δ for $\Gamma^{-1} = 20$ and 10^4 . Data from [55, 56] are denoted by crosses and plusses.

employed event-driven MD simulations at finite temperature (fixed kinetic energy) using an algorithm that strictly prohibits particle overlaps. We find a range of jamming densities as a function of compression rate. We show that the increase in jamming density can not be explained by crystallization effects in contrast with [48]. In addition, our results contrasts the idea that the jamming or random-close-packing density η_{rcp} is well-defined

and can be regarded as the infinite pressure limit of the metastable liquid branch [47–49]. Instead we find that jammed configurations of polydisperse hard spheres can be identified as the infinite pressure limit of glassy states and that different glasses can be formed that jam at different jamming densities as a function of the compression rate. Our work demonstrates nicely the compression rate dependence of η_J for a wide range of size polydispersities and complement recent work that showed the existence of multiple glassy states and jamming densities for binary mixtures of hard spheres [53, 54].

3.5 Acknowledgments

We gratefully thank L. Berthier and S. Torquato for stimulating discussions.

Compression of hard spheres by gravity and electric field gradients

We studied the effects of different compression rates exerted by electric field gradients and a gravitational field on the crystallization and glass formation of colloidal hard spheres in experiments. We show that for hard spheres with a polydispersity of 3% and compressed from higher volume fractions (30%) the glass transition becomes intermixed with the processes of crystal nucleation and growth and thus strongly depended on compression rate. In addition, we explain under what conditions wetting of hard-sphere crystals at smooth walls is prevented to interfere with the glass transition by gravity effects. The effect of gravity can be reduced by density matching the solvent to the density of the colloidal particles. This, however, requires accurate temperature control. Here we choose to slowly rotate the samples (as proposed by Pusey and Bartlett [69]) instead of density matching the solvent while compressing them in an electric bottle. This has two advantages: the temperature does not need to be controlled and gravity can be "switched on" without changing the solvent (and hence the interactions).

4.1 Introduction

One of the simplest systems for investigating the phase behaviour of many particle systems is the hard-sphere system. Colloidal hard spheres are an ideal model system with their experimentally accessible time and length scales. Equilibrium hard-sphere fluids and crystals have been extensively studied by scattering and real-space experiments on colloidal hard spheres as well as in computer simulations. Nevertheless, it is only known since a few years that the equilibrium crystal structure is FCC [10] and that this crystal wets a smooth hard wall [70]. The result of this effort is that the equilibrium properties of hard spheres are now well understood. Hard spheres have also been studied out of equilibrium and hard-sphere glasses are starting to yield their secrets. However, when a monodisperse hard-sphere system is compressed at intermediate compression speeds it does not form a glass or a crystal but an intermediate state, a glass with crystalline domains or a crystal with small domains and thick grain boundaries. Not much is known about these structures which are half glass and half crystal. The competing effects of crystal nucleation and growth with a liquid that is falling out of equilibrium make that the glass transition depends on the speed of compression [51]. We fabricated those intermediate structures and demonstrated how the transition from a perfect crystal to a glass without local (crystalline) order takes place. Since gravity is known to play an important role in the formation of colloidal glasses and crystals, we also investigate the effect of gravity and compare compression by gravity with compression by electric field gradients in a so-called dielectrophoretic bottle [4, 71].

When the dielectric constant ϵ_c of colloidal particles is different from that of the medium ϵ_m , in which they are suspended, the colloids will acquire a dipole moment in an external electric field. This dipole is then attracted ($\epsilon_c > \epsilon_m$) or repelled ($\epsilon_c < \epsilon_m$) from regions with a stronger electric field. Polymethylmetacrylate (PMMA) particles have a lower dielectric constant ($\epsilon_{\text{PMMA}} \approx 2.6$) than CHB and cis-decalin ($\epsilon_m \approx 6 - 7$) so they will be driven towards the regions with a weak electric field. This is an advantage since in these regions the dipole-dipole interactions will also be weak. For this system Leunissen has already demonstrated that it is possible to compress large particles fast enough so that they form a glass [72].

Colloidal hard-sphere glasses have first been characterized in real space by Van Blaaderen [73]. Van Blaaderen demonstrated that when hard spheres with a low polydispersity are compressed by high gravitational forces the glasses that are formed do not have long range correlations. Hermes and Dijkstra [74] have shown using event driven MD simulations that a compression speed of $\Gamma\sigma\sqrt{m/(k_B T)} \geq 1 \cdot 10^{-3}$ results in a configuration that does indeed not have any significant crystalline order. However, when the system was compressed more slowly the crystalline order did increase.

Bulk nucleation can happen at any volume fraction above the coexistence volume fraction of 0.494. However, when the supersaturation is small and the volume fraction is only slightly above that of bulk coexistence the critical nuclei are large and the probability of bulk nucleation is extremely small. For higher densities the rate increases until a volume fraction of approximately 0.57 at which the system starts to slow down significantly and the time it takes the system to go from fluid to crystal starts to increase again [75]. It is very unlikely that a system that has not yet nucleated at a volume fraction of 0.58 will

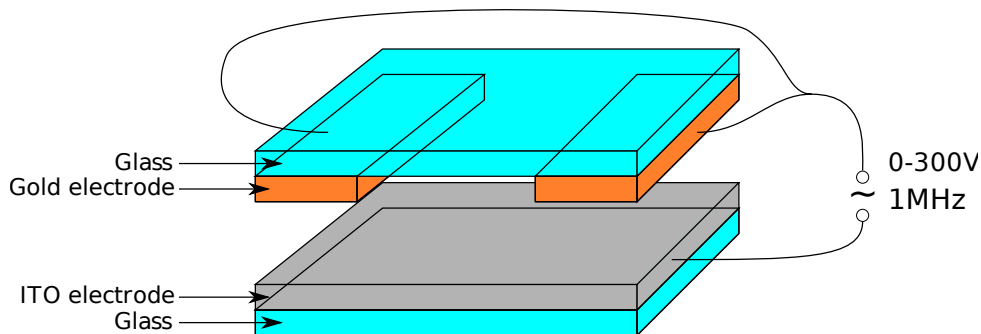


Figure 4.1: Schematic drawing of the slit cell. The thick glass walls and thin electrodes are not drawn to scale. The two top electrodes are both connected to the same output of the source and the bottom electrode is connected to the other output. The spacing between the electrodes is 80-100 μm .

nucleate at a higher volume fraction (when the compression rate is not decreased).

It is known that gravity plays an important role in falling out of equilibrium at the glass transition and the freezing transition of colloidal suspensions. Pusey and Van Meegen [27] have shown that only the top of a suspension of volume fraction 0.62 crystallized while the bottom remained glassy for very long times. Zhu et al. [28] have shown that such a dense suspension will crystallize fully when it is taken into micro gravity. Kegel [76] has shown that even denser suspensions at a volume fraction of 0.631 will also completely crystallize when the density of the particles is matched to that of the solvent. To investigate the effect of gravity we performed experiments in gravity and in a rotating device that removed the effect of gravity by constant rotation. Such a rotation device was first used by Bartlett et al. [69, 77] to investigate the effect of gravity on the formation of colloidal crystals.

Computer simulations have been used to study the effect of different compression rates on the crystalline order of the jammed configurations. Torquato et al. [48] used event driven simulations with different compression speeds to obtain a range of configurations in between a maximally random glass and a crystal. Jin et al. [78] have analysed these computer generated configurations and found that the equilibrium coexistence regime can be frozen in by sufficient fast compression. When a system was first equilibrated in the coexistence regime and afterwards compressed rapidly the liquid became glassy while the crystal remained crystalline. This resulted in a phase transition that is frozen in.

4.2 Methods

In our experiments we used 5.3 μm polymethylmetacrylate (PMMA) particles dyed with 7-nitrobenzo-2-oxa-1,3-diazol (NBD) and a polydispersity of less than 3%. These particles were dispersed in cyclohexyl bromide (CHB) that was saturated with the salt tetrabutylammonium bromide (TBAB) (to approximately 260 μM). The screening length $\kappa^{-1} \approx 50$ nm in CHB saturated with TBAB [72] resulting in fairly hard spheres. The particles have a lower density than the solvent and their Peclet number $\text{Pe} = \Delta\rho\pi\sigma^4g/(6k_B T) = 147$. The Brownian diffusion time $\tau_B = \sigma^2/(6D) \approx 130$ sec which is the average time it takes a particle to diffuse over a distance that equals its own diameter at low density.

The sample cell was a dielectrophoretic bottle with a indium tin oxide (ITO) bottom electrode and a gold electrode with a slit shaped electrode free region at the top as illustrated in Fig. 4.1. The spacing between the top and bottom electrodes was approximately $80 \mu\text{m}$. The sample cell was 3 cm by 1 cm. The slit had a width of approximately $170 \mu\text{m}$ wide. More details on these cells and their construction can be found in [72].

Particle coordinates were obtained using an implementation of the algorithm described by Crocker and Grier [79] adapted to 3D. The large particles made the tracking possible in 3D without the need to resort to fluorescent core-shell particles and the coordinates obtained are accurate to approximately $0.1 \mu\text{m}$ in the z direction. The volume fractions were obtained from the tracking data and are accurate to 0.01th of a volume fraction (one volume percent). The voxel size we used was on average $0.2 \times 0.2 \times 0.6 \mu\text{m}$.

To investigate the crystalline order the three-dimensional bond order parameters Q_m were calculated [14, 80]. In the calculation of the bond order parameter a list of ‘‘neighbours’’ is determined for each particle. The neighbours of particle i include all particles within a radial distance r_c of particle i , and the total number of neighbours is denoted $N_b(i)$. A bond orientational order parameter $\mathbf{q}_{l,m}(i)$ for each particle is then defined as

$$\mathbf{q}_{l,m}(i) = \frac{\frac{1}{N_b(i)} \sum_{j=1}^{N_b(i)} Y_{l,m}(\theta_{i,j}, \phi_{i,j})}{\left(\sum_{m=-l}^l |\mathbf{q}_{l,m}|^2\right)^{1/2}} \quad (4.1)$$

where $\theta_{i,j}$ and $\phi_{i,j}$ are the inclination and azimuth of the bond between i and j and $Y_{l,m}(\theta, \phi)$ are the spherical harmonics with $m \in [-l, l]$. Solid-like particles are identified[31] as particles for which the number of connections per particle $n_{\text{con}}(i)$ is greater than a critical number denoted n_{con}^c and where

$$n_{\text{con}}(i) = \sum_{j=1}^{N_b(i)} H(d_l(i, j) - d_c), \quad (4.2)$$

H is the Heaviside step function, d_c is a threshold value, and

$$d_l(i, j) = \sum_{m=-l}^l \mathbf{q}_{l,m}(i) \cdot \mathbf{q}_{l,m}^*(j). \quad (4.3)$$

We used $m = 6$, $r_c = 1.4$, $d_c = 0.7$ and $n_c = 6$ to determine whether a particle is crystalline. To determine if a particle is HCP or FCC stacked we used $m = 5$, $d_c = 0.5$ and $n_c = 4$. More details about the order parameter can be found in the introduction.

The average crystalline domain size was measured by a weighted average over the size of the domains where we weighted each domain with its size. A fluid contained always many small crystal domains of one or two particles that would otherwise dominate the average. In this way the average crystalline domain size is the expectation value of the domain size of a randomly chosen crystalline particle.

The rotating device, that we used in our experimental setup, consists of a electro motor that rotates the sample at a tunable angular velocity. The axis of rotation was placed exactly horizontal. The electric field was supplied through a mercury contact to provide an uninterrupted connection. The samples shown in this chapter were all rotated

at approximately 1 cycle per minute. We also performed experiments with 0.1 cycle per minute and 2 cycles per minute and did not observe significant differences in the formed structures.

4.3 Results and Discussion

4.3.1 Averaging out the effects of gravity

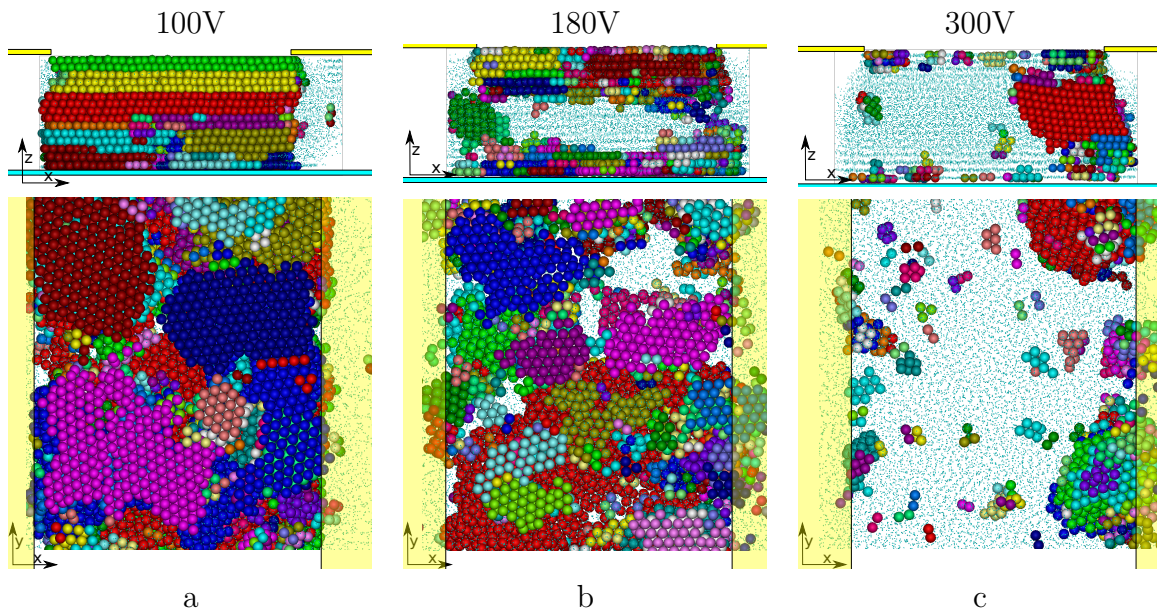


Figure 4.2: *The crystalline domains of samples that were rotated while being compressed. The top row contains side views of the samples along the slit and the bottom row shows views from the bottom. The samples are all top/bottom symmetric because of the absence of sedimentation. a) The compression was performed at 100 V and the entire sample was filled with crystalline domains. b) The compression was performed at 180 V and the sample was crystalline at the top and at the bottom but mostly consisted of glass in the middle. c) The compression was performed at 300 V and most of the sample consisted of glass except two large and many small bulk nuclei.*

We investigated samples that have been compressed with the dielectrophoretic bottle using electrical field gradients of increasing strength. The field was switched on while the sample was homogeneous and had been rotating for many hours. We are interested in the competition between glass formation and heterogeneously and homogeneously nucleated crystals as a function of the compression speed. We are especially interested in the properties of the intermediate stages that are partly crystalline and partly glassy. The initial volume fraction was 0.3.

When the system was compressed slowly at 100 V it crystallized mostly from the walls towards the middle of the sample. Nucleation in the bulk apparently was too slow at this speed. Since the hard-sphere crystal is known to wet the smooth hard walls crystallization starts already below the bulk coexistence density at the wall [70] when the probability of

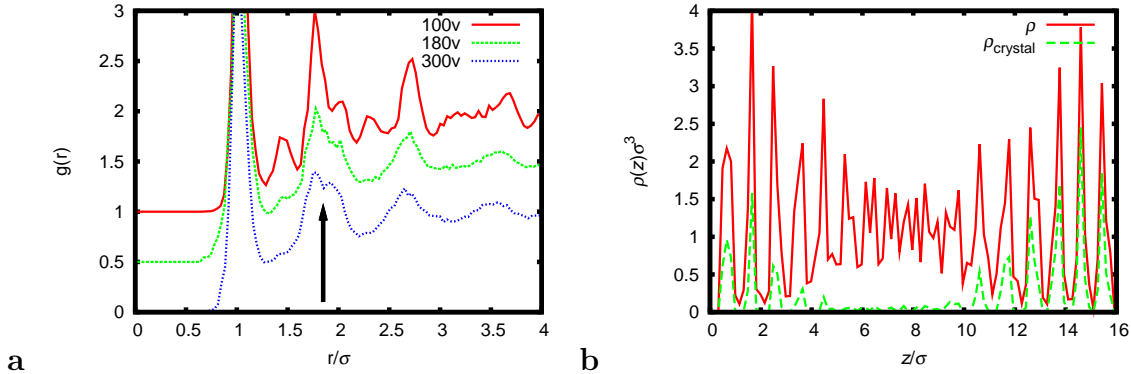


Figure 4.3: **a)** The radial distribution function $g(r)$ of the samples compressed at different speeds. The $g(r)$'s were averaged over all particles in multiple stacks more than one diameter away from the two walls. The arrow indicates the split second peak. **b)** The number density of all particles and of crystalline particles as function of height for a sample compressed at 180 Volt.

spontaneous nucleation in the bulk was still too low with respect to the compression rate. Upon slowly increasing the density, the crystals grew from the walls. The fluid in the bulk never reached a density at which bulk nucleation was fast enough to compete with the growth of the wall nucleated crystals. It is remarkable that such crystals nucleate and grow at the walls, which have almost never been reported before for hard-sphere systems. In Fig. 4.2a we show the crystalline particles after 30 minutes of compression. The hexagonal planes of the crystals were parallel to the walls and were randomly stacked. The orientation of the close packed lines in the different hexagonal stacks was random with respect to each other. The domains often spanned the height and width of the slit and consisted of $1 \cdot 10^4$ particles. There seemed to be a slight preference for FCC stacking and approximately 60% of the particles were in a FCC neighborhood and 40% of the particles were in a HCP neighborhood according to the Q_5 analysis. On average 75% of the particles was crystalline according to the Q_6 bond order correlation parameter. The final volume fraction was $\eta = 0.70$. The radial distribution function, shown in Fig. 4.3a, shows the characteristic peaks of a RHCP crystal.

When the compression was performed with a voltage of 180 V the compression was faster and the wall induced crystal domains were smaller. The grain boundaries were also wider and domains that grew from the top were no longer able to merge with the domains that grew from the bottom wall. The stacking of the nuclei was random with 50% of the particle in an FCC neighbourhood and 50% in an HCP neighbourhood. Since the crystals growing from the walls could not keep up with the density increase, bulk nucleation also started to play a role resulting in small nuclei with a random orientation in the middle of the sample. The radial distribution in Fig. 4.3a shows still many of the peaks of the RHCP crystal but the higher order peaks have disappeared and a split second peak has become visible, which is characteristic for dense amorphous sphere packings[81]. The final volume fraction is on average $\eta = 0.68$.

When the voltage was set to 300 V the compression was so fast that most of the sample

became glassy. Only the two layers at the top wall and the two layers at the bottom wall contained crystalline domains. These hexagonal domains were approximately six particle diameters wide and irregularly distributed. The radial distribution function showed the characteristic split second peak and only the first few crystalline peaks were visible. The volume fraction decreased to $\eta = 0.67$

To investigate the effect of the walls on the structure, the density profile of a sample compressed at 180 V is plotted in Fig. 4.3b. The middle of the sample was not very structured while close to the walls strong layering could be seen. The crystalline particles were located in these layers, however, the glass on top of these crystalline structures also showed strong layering. It is apparently possible to have a strongly layered structure in a glass with not significantly more crystalline order than a bulk glass.

Torquato et al. [48] already showed using MD simulations that compressions at intermediate compression rates result in configurations with intermediate densities. In these configurations only a fraction of the particles is crystalline. Our experiments confirm these observations and demonstrate that these intermediate structures can indeed be formed.

4.3.2 Influence of gravity

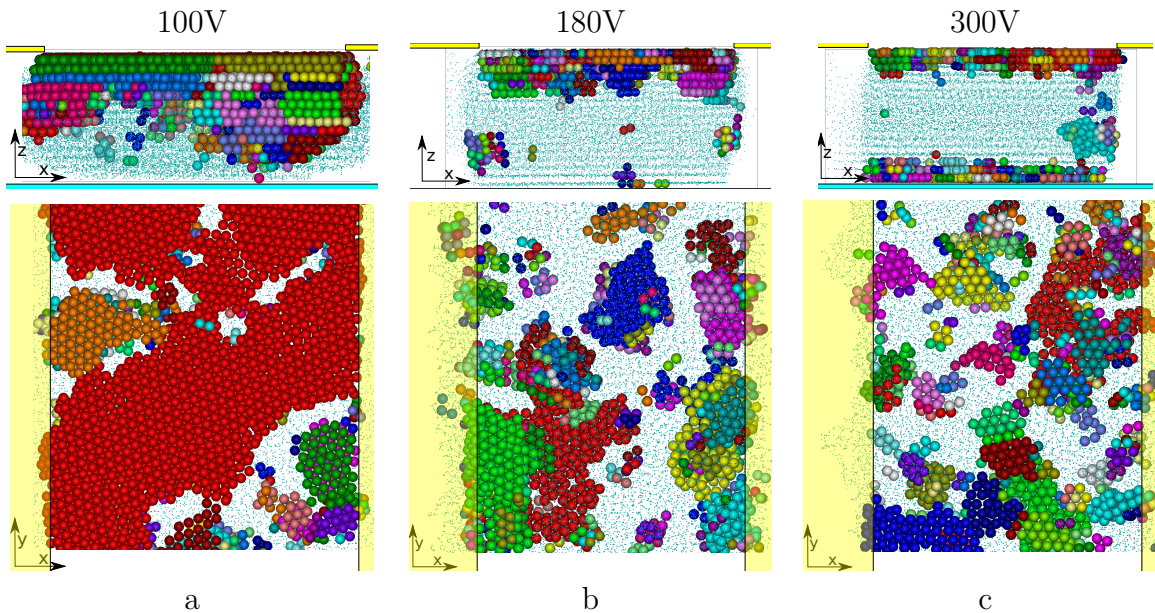


Figure 4.4: *The crystalline domains of a sample that sedimented while being compressed. At the top are side views of the samples along the slit and at the bottom are views from the bottom. The particles are lighter than the solvent so they go towards the top of the sample. a) The compression was performed at 100 V and the entire sample is filled with crystalline domains. The compression is so slow that we did not wait long enough for the entire slit to be filled with particles. b) The compression was performed at 180 V and the sample is crystalline at the top and glassy at the bottom. c) The compression was performed at 300 V and most of the sample contained glass except a thin layer of crystal on both walls. Also some bulk nuclei can be seen.*

To investigate the effect of gravity we also performed the same experiment on a sample

that was homogenised by rotating but taken out of the rotation device when the field was turned on. We expect that the additional compression resulting from gravity will decrease the fraction of the sample that is crystalline. Since our particles were lighter than the solvent they creamed towards the top of the sample.

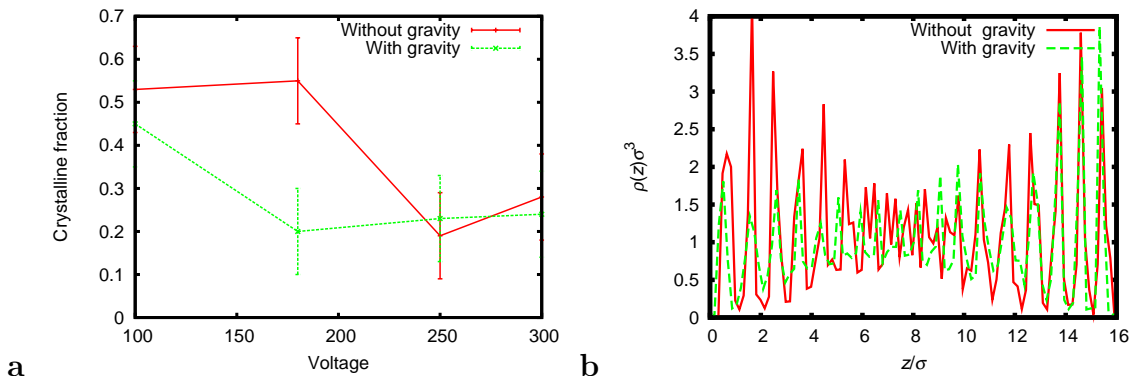


Figure 4.5: **a)** The fraction of crystalline particles as function of the voltage on the dielectrophoretic bottle with and without gravity. **b)** The number density as function of height for the same compression with and without gravity at 180 Volts. The ITO electrode is located at the bottom at $z=0$, the top electrode is located at the top at $z=16$ (the particles cream to the top).

In Fig. 4.4a we depict the crystalline particles of a sample compressed at 100 V. The compression was not strong and fast enough to fill the slit from top to bottom within 30 minutes. At the top wall the sample was crystalline but at the bottom wall the sample was dilute with a total volume fraction of 0.5 at the time of the snapshot. The slit filled up more slowly than before since the electrical field had to push the particles against gravity. The crystal that formed had a preference for FCC with $60 \pm 10\%$ FCC and $40 \pm 10\%$ of the particles HCP stacked. We do not have enough statistics to conclude about a possible preference for FCC or HCP stacking as seen by Hoogenboom et al. [82]. The lack of statistics is caused by large fluctuations in the stacking between different positions in the sample and different samples.

When we homogenised the sample and performed the compression with 180 V the density became more homogeneous as can be seen in Fig. 4.4b. The field induced compression easily overcame gravity and filled the entire slit with particles. However, the top of the sample contained crystalline regions while the bottom remained glassy, apparently the creaming effect caused by gravity did prevent crystallization induced by the lower wall. The crystalline domains were approximately 6 particles in diameter. The final volume fraction was 0.67.

In Fig. 4.4c we depict the crystalline particles of a sample compressed with a high compression rate at 300 V. The middle of the sample was mostly amorphous whereas the top and the bottom wall nucleated only two crystalline layers and there were only a few small nuclei in the bulk of the sample, of which the close packed planes had random orientations with respect to the walls. The average diameter of a crystalline domain was only 5 particle diameters. The final volume fraction was 0.65.

In Fig. 4.5a we compare the fraction of the samples that was crystalline after 30 min for

different compression speeds and for samples under the influence of gravity and samples that were rotated. We averaged over five to ten stacks each containing $2 \cdot 10^4$ particles. The sedimenting samples showed a smaller percentage of crystalline particles for all compression speeds up to 250 V where the compression was so fast that sedimentation did not have a chance to compress the system significantly as well. For 100 V the difference was caused by the low overall density, however, at 180V the system became nearly completely crystalline when rotated and only close to the top wall when under the influence of gravity.

In Fig. 4.5b the density profile is plotted for a system that was compressed with gravity and for a system that was compressed without gravity. Both systems show strong layering at both walls. The system compressed with gravity only had crystalline particles near the top plate while the system compressed without gravity had crystalline particles at both top and bottom wall.

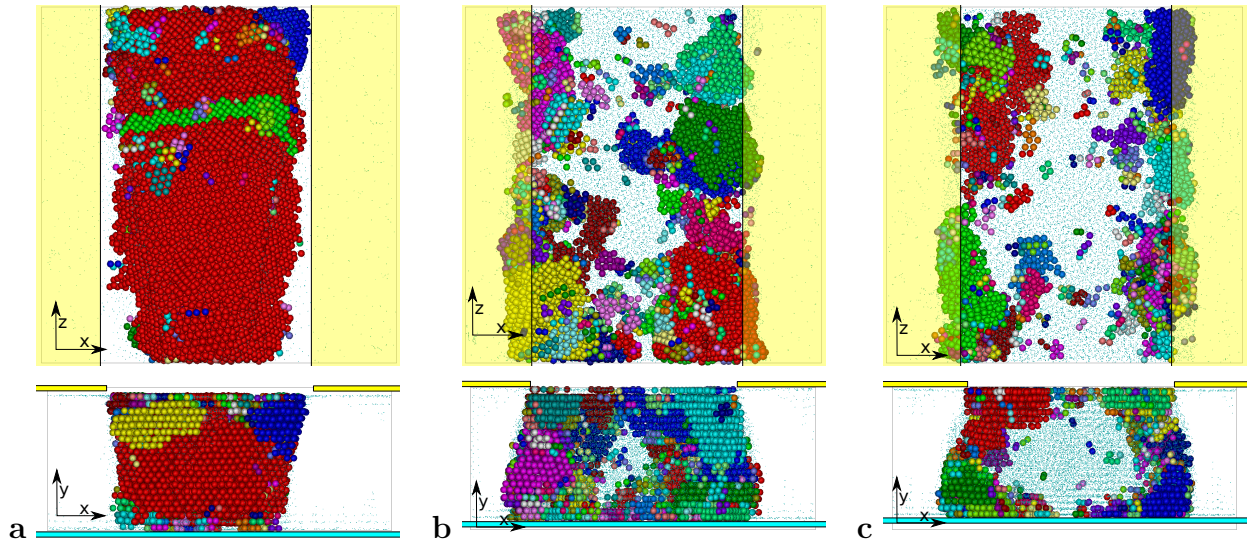


Figure 4.6: A sample compressed using 65 V with gravity parallel to the slit. The yellow planes indicate the positions of the gold electrodes. **a)** The top of the inverted mountain of particles in the slit. **b)** Part of the inverted mountain just above the tip. **c)** Further up in the sample.

To increase the effect of gravity the sample was also mounted vertically instead of horizontally. Now the long edge of the slit ran along the gravity direction. In this configuration a zero field already resulted in the formation of a glass throughout most of the sample. Only at the bottom crystals were formed. When the sample aged the crystal grew very slowly up into the glass.

We compressed a sample in this orientation with 65 Volts. In Fig. 4.6 the crystalline domains are shown after compression. The colloids outside of the slit had all moved to the top of the sample. The colloids in the slit formed a sharply peaked inverted mountain that sticks out of the sediment. The colloids at the bottom of the slit had crystallized completely while they formed a glass at the top and in between the mixed states were formed. The particles near the edges of the slit were crystalline further up into the sample while the particles in the center were amorphous. The majority of the crystals consisted of hexagonal layers parallel to the glass wall indicating wall-induced crystallization. The

top of the sample was completely glassy with approximately the same amount of order as a stable fluid.

Gravity has an influence on the compression speed and consequently it has an effect on the glass transition. The geometry is of a major importance in samples with gravity when the particles are sedimenting. When the sample is oriented with its long edge parallel to gravity the pressure exerted on the particles at the bottom is very large compared to the pressure exerted on the particles at the bottom when its short side is parallel with gravity. It is possible that crystals that nucleated at a smooth wall slide down and are destroyed in the process. As far as we know this explanation has not yet put forward to explain why hard-sphere crystallisation is not dominated by crystals nucleated and grown inwards from smooth walls as theory and simulations predict. This corresponds with the results of Zhu et al. [28] who perform experiments in microgravity and show that the glass transition is very sensitive to gravity.

4.3.3 Slowly growing crystals

To investigate the time dependence of the compression process further, which for the kind of electric bottle we used is known to be a complicated function of time as the gradient region is relatively small, we performed a compression at 200 V and followed the system over time. The sample was homogenized by rotation before the electric field was turned on. Because it is difficult to follow compression in an electric bottle as a function of time under the condition in which we average out gravity by rotating the sample, we look at differences caused by compression of gravity as compared to the electric field gradients.

After the field was turned on the sample was transferred to the confocal microscope and the imaging started. The fast compression, caused by the depletion of the regions where the electrical field rises steeply, already occurred and the volume fraction had increased from 0.3 to 0.6 in the 3 minutes before the first frame was taken [83]. In the first frame there were already small crystalline domains attached to the top wall, these domains filled 11% of the sample (Fig. 4.7). When the sample aged existing nuclei grew but also new nuclei formed. After one hour 22% of the sample was filled with crystalline parts. The particles on the bottom wall did not form a hexagonal layer and no crystalline domains were observed near the bottom wall (similarly as shown in Fig. 4.4). The sample was, although it was at very high density and pressure, slowly changing in time which included crystal nucleation and growth. In figure 4.7d we show the crystalline fraction as function of time. The crystallization slowed down when the density increased but did not stop. Pusey and van Megen [27] also observed a slow growth of the crystal into the glass that continued for a very long time.

4.4 Conclusion

We have shown that the glass transition of colloidal hard spheres depends on the compression rate. The compression rate in turn depends on external fields such as gravity and electrical field gradients. The compression rate due to gravity depends strongly on the sample geometry. An elongated sample with the long axis horizontal crystallized

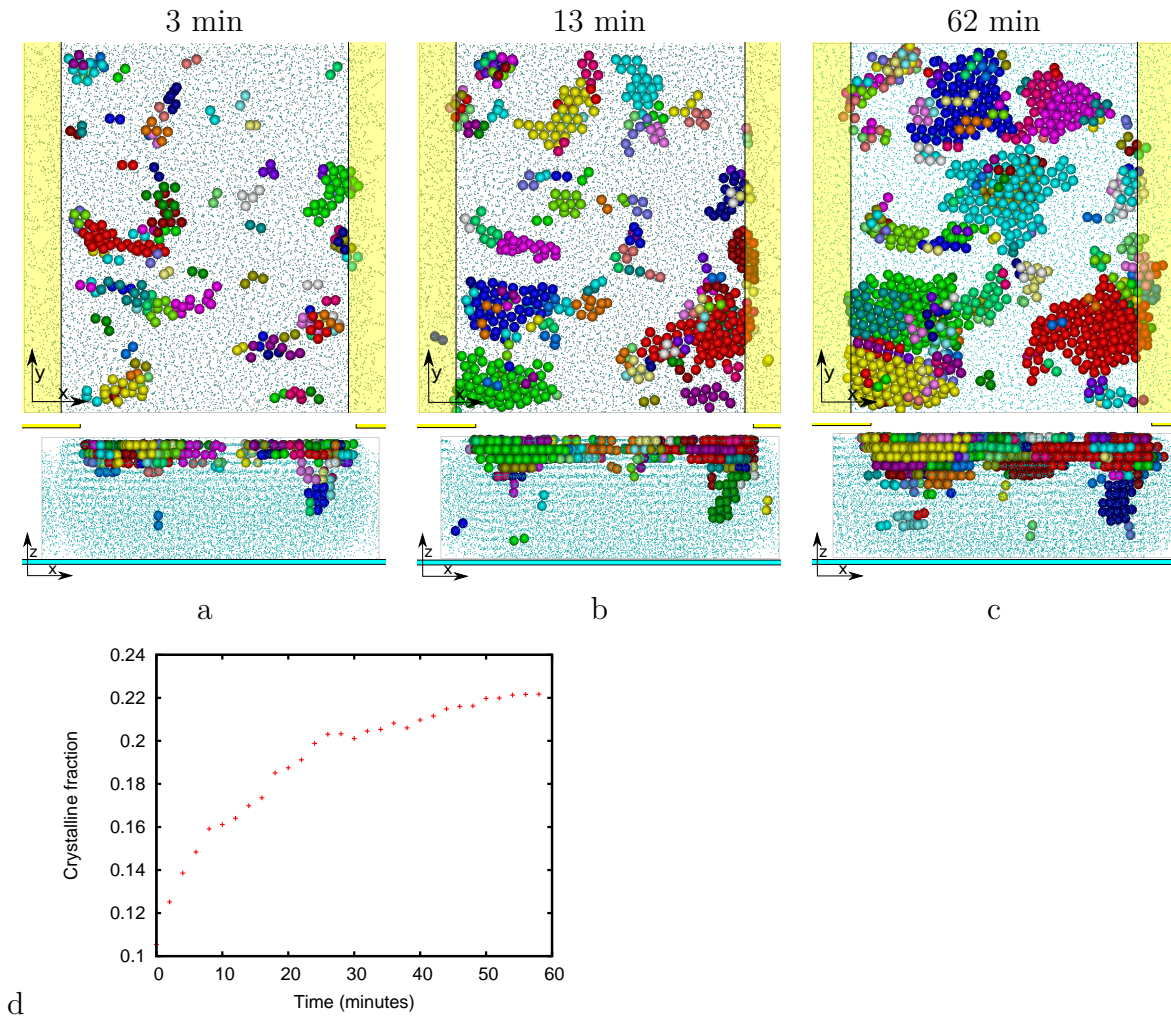


Figure 4.7: The percentage of crystalline particles determined using Q_6 as a function of time for a compression run at 200V in a sample that is under the influence of gravity. The volume fraction of the not crystalline regions in the center of the slit starts at $\eta = 0.61-0.63$ and ends at $\eta = 0.63-0.65$. We do not show the hexagonal layer of particles that had formed at the top glass wall. The compression was started at $t=0$. **a)** The crystalline particles after 3 minutes. **b)** The crystalline particles after 13 minutes. **c)** The crystalline particles after 63 minutes **d)** The fraction of crystalline particles as function of time.

completely, while a sample with the long axis vertically formed a glass. The height of the sample determined not only the final pressure at the bottom but also the rate of compression. When a fluid was compressed at intermediate compression rates it formed a structure with crystalline domains surrounded by glass. When the compression rate was increased the crystalline domains became smaller. Even at volume fractions above 0.63 crystalline domains kept growing slowly.

Homogeneous nucleation

We employ different simulation techniques to measure the rate of crystal nucleation for hard spheres for packing fractions below the kinetic glass regime and compare the rates obtained from these techniques with each other and with those obtained from experiments. The effect of different order parameters to define a crystalline cluster on the shape and size of the critical nucleus is investigated. We find that all techniques yield similar results for the critical nucleus shape. When unbiased spontaneous simulations are feasible they yield the most accurate nucleation rates, however, they are at present impossible for low supersaturation. Umbrella sampling simulations yield nucleation barriers but to obtain the rate across the barriers additional simulations need to be performed. The nucleation rates obtained from both simulation techniques agree within the statistical errors validating the techniques used in the biased simulations. The experiments yield similar results for high supersaturation, however, they yield higher rates than those found with simulations for lower volume fractions. We speculate that this might be caused by different crystal domains present within the growing nuclei that are counted as different nuclei in the experiments, yielding an overestimation of the nucleation rate.

5.1 Introduction

Nucleation processes are present in both natural and artificial systems. However, the occurrence of a nucleation event is often rare and difficult to examine both experimentally and theoretically.

Colloidal systems are almost ideal model systems for studying nucleation phenomena. Nucleation and the proceeding crystallization in such systems often takes place on experimentally accessible time scales, and due to the size of the particles, they are accessible to a wide variety of scattering and imaging techniques, such as (confocal) microscopy [84, 85], holography [86], light and x-ray scattering [87]. Additionally, progress in particle synthesis, solvent manipulation, and the application of external fields allows for significant control over the interparticle interactions, allowing for the study of a large variety of nucleation processes.

One such colloidal system is the experimental realization of “hard” spheres comprised of sterically stabilized polymethylmethacrylate (PMMA) particles suspended in a liquid mixture of decaline and carbon disulfide [88]. Experimentally, the phase behaviour of such a system has been examined by Pusey and van Megen [27] and maps well onto the phase behaviour predicted for hard spheres. Specifically when the effective volume fraction is scaled to reproduce the freezing volume fraction $\eta = 0.495$ of hard sphere simulations the effective melting volume fraction has been found to be $\eta = 0.545 \pm 0.003$ [27] which is in good agreement with what simulations predict for hard spheres [1]. The nucleation rates have been measured using light scattering by Harland and van Megen [88] and Sinn et al. [89], in real space experiments by [90] and in simulations by Auer and Frenkel [91]. However, the simulations and the experiments do not seem to be in agreement. The reason of this study is to try to gain understanding of the discrepancy between simulations and experiments.

On the theoretical side, the hard-sphere system is one of the simplest systems which can be used to study colloidal and nanoparticle systems, and generally, to investigate the nucleation process itself. As such, it is an ideal system for examining various computational methods for studying nucleation, and comparing the results against the experimental data. Such simulation methods include molecular dynamics (MD) simulations, umbrella sampling simulations (USS) [80], forward flux sampling (FFS) [92], and transition path sampling (TPS) [93].

Classical nucleation theory (CNT) is the simplest theory to describe nucleation. Small crystal nuclei are continually being formed in a fluid due to thermal fluctuations. Most of these small nuclei quickly melt away, however, when the fluid is supersaturated these nuclei have a chance to grow out. In CNT it is assumed that the free energy of making these small nuclei is given by a surface free energy cost and a bulk free energy gain. The Gibbs free energy displays a maximum at the critical size and when a nucleus is larger than this critical size the chance of growing out exceeds the chance of melting back into the fluid. With CNT the nucleation barriers can be predicted and compared with simulations. When the kinetic prefactor is known nucleation rates can be obtained from these barriers as well.

Umbrella sampling [8, 94] is a (relatively) well established method, to examine the nucleation process and to determine the nucleation barrier. The calculated barrier can

then be used in combination with kinetic Monte Carlo (KMC), Brownian dynamics (BD) or MD simulations to determine the nucleation rate [91]. In USS the simulations are performed in a biased ensemble which is chosen such that the unlikely event of the formation of a critical nucleus becomes more probable. The results obtained in this ensemble are mapped back onto the unbiased ensemble to obtain the actual probability of the formation of a critical nucleus. Usually these simulations are performed in small windows in which only a narrow distribution of nucleus sizes is sampled. These windows then have to be stitched together to obtain the total barrier. The success of the method is expected to highly depend on the choice of order parameter and biasing potential. Additionally, as the method is based on configurational averages, it assumes that the nucleus is in quasi-equilibrium with the surrounding supersaturated fluid.

Molecular dynamics or BD simulations are ideal to study the time evolution of systems, and, when possible, they are the natural technique to study processes such as nucleation. Unfortunately, however, available computational time often limits the types of systems which can be effectively studied by these dynamical techniques. Brownian dynamics simulations, which would be the natural choice to use for colloidal systems, are very slow, due to the small time steps required to handle the steep potential used to approximate the hard-sphere potential. Event driven MD simulations are much more efficient to simulate hard spheres and enable us to study spontaneous nucleation of hard spheres over a range of volume fractions. Fortunately, it turns out that the long time dynamics which are important for nucleation are not sensitive to the details of the short time dynamics.

To compare with experiments we have to take into account the effects of hydrodynamics. We expect that the effects of dynamics on single particle diffusion are automatically taken into account when the rates are expressed in units of the long time diffusion. This is confirmed by the fact that we find no significant difference between the nucleation rates obtained from MC and MD simulations. However, hydrodynamics might effect the collective dynamics differently than the single particle dynamics. We do not know how important collective dynamics are on nucleation and do not know of an efficient technique to include these complex effects into our simulations. Therefore we do not include any hydrodynamics into our calculations.

In this chapter we examine the effect of the choice of order parameter, used to bias the system, on the nucleation process, and compare USS results with results from MD simulations. In the region in which we compare both techniques we find good agreement between both simulation techniques. We have also studied the nucleation and subsequent growth process with MD simulations. We find that the critical nuclei of both techniques have a very similar form and shape. The growing nuclei are rich in defects and contain many small domains. Finally, we compare our predicted nucleation rates to those measured in experiments[88, 89]. We speculate that the defect rich nuclei could cause an overcounting in the number of nuclei in scattering experiments which could explain the high nucleation rates at low volume fractions.

5.2 Methods

This section contains an overview of the methods used. We first discuss CNT and obtain theoretical predictions for nucleation barriers. After that we explain the order parameter that is used in the simulations to distinguish crystals and how we detect the different domains within a crystal. Next the simulation details are given for the MD simulations and the USS. We finish with the method to calculate the kinetic prefactor and the nucleation rate once the free energy barrier is known.

5.2.1 Classical nucleation theory

CNT states that the Gibbs free energy difference between a homogeneous bulk fluid and a system containing a spherical nucleus of radius R is given by

$$\beta\Delta G = \gamma_{\text{fs}}4\pi R^2 - \Delta\mu\rho_s\pi R^3\frac{4}{3} \quad (5.1)$$

where $\Delta\mu = \mu_{\text{f}} - \mu_{\text{s}}$ is the chemical potential difference between the fluid and the solid, ρ_s is the density of the solid and γ_{fs} is the surface tension of the fluid-solid interface. The radius of the critical cluster is given by

$$R_{\text{c}} = \frac{2\gamma_{\text{fs}}}{\Delta\mu\rho_s}. \quad (5.2)$$

The barrier height is given by

$$\beta\Delta G_{\text{crit}} = \frac{16\pi\gamma_{\text{fs}}^3}{3\rho_s^2\Delta\mu^2}. \quad (5.3)$$

The nucleation barrier itself cannot be measured directly in experiments and only the nucleation rate is accessible. We will discuss a method to obtain the nucleation rate from the barrier height later in this chapter.

5.2.2 Order Parameters

In this chapter, an order parameter is used to differentiate between fluid- and solid-like particles and a cluster algorithm is used to identify the solid clusters. For this study we have chosen to use the local bond-order parameter introduced by ten Wolde [80, 95] in the study of crystal nucleation in a fluid of Lennard-Jones particles. This order parameter has been used in many studies of crystal nucleation, including a previous study of hard sphere nucleation by Auer and Frenkel [91].

In the calculation of the local bond order parameter a list of “neighbours” is determined for each particle. The neighbours of particle i include all particles within a radial distance r_c of particle i , and the total number of neighbours is denoted $N_b(i)$. A bond orientational order parameter $q_{l,m}(i)$ for each particle is then defined as

$$q_{l,m}(i) = \frac{\frac{1}{N_b(i)} \sum_{j=1}^{N_b(i)} Y_{l,m}(\theta_{i,j}, \phi_{i,j})}{\left(\sum_{m=-l}^l |q_{l,m}|^2\right)^{1/2}} \quad (5.4)$$

where $m \in [-l, l]$. Solid-like particles are identified as particles for which the number of connections per particle $n_{\text{con}}(i)$ is greater than a critical number denoted n_{con}^c and where

$$n_{\text{con}}(i) = \sum_{j=1}^{N_b(i)} H(d_l(i, j) - d_c), \quad (5.5)$$

H is the Heaviside step function, d_c is a threshold value, and

$$d_l(i, j) = \sum_{m=-l}^l q_{l,m}(i) q_{l,m}^*(j). \quad (5.6)$$

A cluster contains all solid-like particles which have a solid-like neighbour in the same cluster. Thus each particle can only be a member of one cluster.

The parameters contained in this algorithm include a neighbour cutoff, r_c , a dot-product cutoff d_c , a critical number of solid-like neighbours n_{con}^c , and a symmetry index for the bond orientational order parameter l . The solid nucleus of a hard-sphere crystal is expected to consist of randomly stacked hexagonal planes, thus the symmetry index is chosen to be six in all cases in this study. We will study the effect of the choice of n_{con}^c in more detail later. We have used $n_{\text{con}}^c = 7$, $d_c = 0.7$ and $r_c = 1.4\sigma$ unless noted otherwise.

We are not only interested in the crystalline order but also in the stacking of the hexagonal layers. The free energy difference between FCC and HCP is very small [10] and it is expected that the stacking of the crystal will be random. To determine the stacking of the critical nuclei we have used the Q_5 order parameter. In the case of both FCC and HCP there are twelve nearest neighbors for any given particle: six in the same hexagonal layer and three above and three below. The six neighboring particles in the hexagonal layer are identically situated for both FCC and HCP and cannot be used to distinguish between the two structures. However, the triangle formed by the three particles on top is oriented in the same direction, as the triangle beneath, in the case of HCP, while they are oriented oppositely in the case of FCC. The Q_5 order parameter is sensitive to this effect. We use the Q_5 correlations but with different cut off values as used for the Q_6 order parameter. We use $d_c = 0.5$ and $n_{\text{con}}^c = 4$ and $r_c = 1.4\sigma$. This allows us to distinguish between particles in an FCC and particles in an HCP environment. More details can be found in the introduction.

5.2.3 Molecular Dynamics

In molecular dynamics simulations the equations of motion are integrated to follow the time evolution of a system. Since the hard-sphere potential is discontinuous the interactions only take place when particles collide. These collision events are identified and handled in order of occurrence in an event driven simulation. Thus the particles move in straight lines (ballistic) until they encounter another particle with which they perform an elastic collision [96].

We would like to compare our results with experiments on colloidal particles that exhibit Brownian motion. To be able to compare the MD simulations with the colloidal systems we can only look at the long time dynamics since the short time dynamics will be different. Fortunately Pusey et al. [75] have shown that nucleation is governed by the

long time dynamics, which is expected since particles have to rearrange on length scales comparable to their diameter to form a crystal. To obtain the long time diffusion we have measured the mean squared displacement as a function of time and fitted the slope to obtain the long time diffusion coefficient.

Measuring nucleation rates from MD simulations is straightforward for relatively low supersaturations. We simply measure the time until a nucleation event takes place. To pinpoint a nucleation event for low supersaturations the cluster size was measured. When the largest cluster exceeded the size of the critical nucleus significantly we determined the time at which the largest cluster had the critical size. This is easy to determine for low supersaturation when the nucleation times are relatively long compared to the nucleation event itself and when the critical nucleus sizes are known from USS. However, for high supersaturations pinpointing the time of a nucleation event is more difficult. Often many nuclei form at once and we have to estimate the critical nucleus size from CNT or MD simulations. Also the precise details of the initial configuration start to play a role at high supersaturations since the equilibration time of the fluid is of the same order of magnitude as the nucleation rate.

We performed MD simulations with up to 100,000 particles in a cubic box with periodic boundary conditions in the NVE ensemble. Time was measured in MD units $\sigma\sqrt{m/k_B T}$. The order parameter was measured every 10 time units and when the largest cluster exceeded the critical size by 100 percent i.e. twice the size of the critical nucleus, we estimated the time τ_{nucl} at which the critical nucleus was formed using stored previous configurations. We performed up to 20 runs for every density and averaged the nucleation times. The nucleation rate is then given by $R = 1/(\tau_{\text{nucl}}V)$.

5.2.4 Umbrella Sampling

Umbrella sampling is a technique developed by Torrie and Valleau [8] to study rare events. This method has been applied frequently to study nucleation events [94], and specifically has been applied in the past to study crystal nucleation of hard spheres [91]. In general, umbrella sampling is used to examine parts of configurational space which are inaccessible by traditional schemes, e.g. Metropolis Monte Carlo. Typically, a biasing potential is added to the true interaction potential of the system to sample a specific region of configuration space. The biasing potential, however, is added in a manner such that it is easy to “un”-bias the measurables. While it is simple to sample the fluid, crystalline clusters of larger sizes will be rare, and as such, can not be sampled on reasonable time scales. The typical biasing potential for studying nucleation is given by [80, 95]

$$U_{\text{bias}}(S(\mathbf{r}^N)) = \frac{k}{2}(S(\mathbf{r}^N) - S_C)^2 \quad (5.7)$$

where k is a coupling parameter, S is the size of the largest cluster in the system, and S_C is the targeted cluster size. By choosing k carefully, the simulation will fluctuate around that part of configurational space that corresponds to S in the vicinity of S_C . The expectation value of an observable A is then given by

$$\langle A \rangle = \frac{\langle A/W(S) \rangle_{\text{bias}}}{\langle 1/W(S) \rangle_{\text{bias}}} \quad (5.8)$$

where

$$W(S) = \exp \left[-\beta U_{bias}(S(\mathbf{r}^N)) \right]. \quad (5.9)$$

Using this scheme to measure the probability distribution $P(n)$ to find a cluster of size n , the Gibbs free energy can be determined by

$$\beta G(S) = \text{constant} - \ln(P(n)). \quad (5.10)$$

More details on this method are given by Frenkel and Smit [6].

The first simulation we perform is an unbiased simulation in which we measure the probability that a random particle is the center particle of a cluster of size n . We define $P(n) = N_n/N$ where N_n is the number of clusters of size n and N is the total number of particles in the system. To obtain the nucleation barrier we need the probability $P(n)$ for $n < n_c$. Since the chance that a critical nucleus forms spontaneously is small for low supersaturation we use USS to sample clusters at the top of the barrier.

In our implementation of USS, we break the nucleation process up into a number of windows and determine the ratio of probabilities $C(n)$ in each window, with $C(n)$ the probability that the largest cluster in the system contains n particles. We later stitch these windows together as described by Auer [97] to obtain the probability ratios across the barrier. To obtain the normalization constants in Eq. 5.10 we match the beginning of our first umbrella sampling window to the Gibbs free energy curve of the unbiased simulation. We repeat this procedure with the other windows until we have determined all normalization constants.

Note that we do not measure the same probability in the biased and in the unbiased simulations. However, it will be unlikely that the system contains more than one large cluster in the unbiased simulation. We therefore assume that the probability ratio of having a maximum cluster of size $n+a$ and n , i.e. $C(n)/C(n+a)$, becomes approximately equal to the probability ratio $P(n)/P(n+a)$. So although we did not measure the same probability ratio it will be approximately the same for large enough clusters. Thus when the unbiased simulation run is long enough we can attach it to the biased simulations to obtain $P(n)$ and the Gibbs free energy of a crystalline cluster using equation 5.10.

5.2.5 Kinetic prefactor

Once the Gibbs free energy barrier ΔG_c is known from simulations or theory the nucleation rate can be calculated. The crystal nucleation rate is related to the free energy barrier by [91]

$$I = \kappa e^{-\beta \Delta G_c} \quad (5.11)$$

where κ is the kinetic prefactor which can be approximated by:

$$\kappa \approx \rho f_{n_c} \sqrt{\frac{|\beta \Delta G''(N_c)|}{2\pi}}, \quad (5.12)$$

ρ is the number density of the metastable fluid, G'' is the second derivative, and f_{n_c} is the rate at which particles are attached to the critical cluster. Auer and Frenkel [91] showed

that the attachment rate f_{nc} can be related to the mean square deviation of the cluster size at the top of the barrier, specifically,

$$f_{nc} = \frac{1}{2} \frac{\langle \Delta n_c^2(t) \rangle}{t}. \quad (5.13)$$

The mean square deviation of the cluster size can then be calculated by either employing a kinetic MC (KMC) simulation or a MD simulation of a cluster at the top of the barrier. To relate the time of this KMC to the time in the MD simulations and the experiments, the long time diffusion coefficient D_l was calculated in the fluid at the same density and with the same step size.

5.3 Results

We calculate the nucleation rates and compare the results obtained from the two simulation techniques with each other and with experiments. We determine the nucleation barrier using CNT as well as with USS and we perform simulations to measure the attachment rate with which we calculate the nucleation rate once the barrier is known. The attachment rates are calculated using kinetic MC. At the end of this section we compare the results of CNT, MD simulations, USS and experiments.

5.3.1 Gibbs free energy barriers

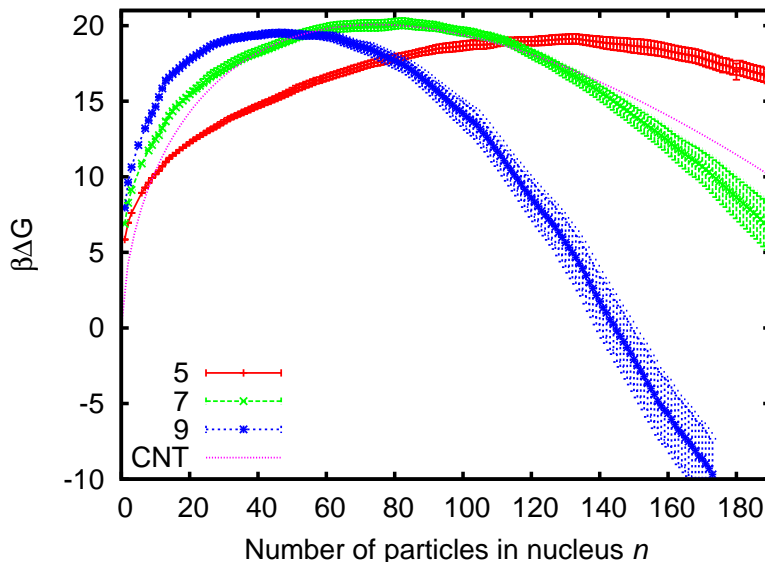


Figure 5.1: The Gibbs free energy $\beta\Delta G$ as a function of cluster size n at $\eta = 0.5355$ obtained from USS using different crystalline order parameters. The error bars were obtained from five independent simulations.

We have calculated the Gibbs free energy barriers by means of USS using different order parameters to bias our simulation at pressure $\beta p \sigma^3 = 17.03$, which corresponds with

a volume fraction $\eta = 0.5355$ for the metastable fluid. The barrier height with the strict order parameter $n_{con}^c = 9$ is $\beta\Delta G = 19.5 \pm 0.5$ with $n_{con}^c = 7$ the height is $\beta\Delta G = 20.0 \pm 0.5$ and with the loose order parameter $n_{con}^c = 5$, $\beta\Delta G = 19.0 \pm 0.5$. We have calculated the standard error from the variance of 5 independent simulations. The error bars grow for larger clusters since the errors accumulate upon growing the cluster. The difference in height between the three barriers is within the statistical error bars. However, the size of the critical nucleus depends strongly on the crystalline order parameter. This is to be expected, since a strict order parameter takes into account less particles in the interface while a loose order parameter will define more particles to be crystalline yielding a shift in cluster size.

Since our results fall on top of the previous results of Auer and Frenkel [91] we only performed USS for high supersaturation where we can compare directly with MD simulations. At these high supersaturations care has to be taken to avoid the formation of multiple nuclei within the simulation box. When multiple nuclei form in USS the system the first unbiased simulation can no longer be attached to the first biased simulation and the barrier can no longer be determined.

Classical nucleation theory has only one unknown parameter which is the surface tension of the solid and the fluid interface γ_{fs} . At coexistence the surface tension has been measured by Davidchack et al. [98] and it depends on the crystal orientation at the interface. They obtained $\beta\gamma_{fs}\sigma^2 = 0.574$, 0.557 and 0.546 for the (100), (110) and (111) planes, respectively. For a spherical nucleus, the effective surface tension is expected to be an average over all exposed crystal planes. When we fit the top of our nucleation barrier with CNT we obtain a surface tension of $\beta\gamma_{fs}\sigma^2 = 0.765$ which is very close to the value $\beta\gamma_{fs}\sigma^2 = 0.751$ found by Auer et al. [97] for this volume fraction $\eta = 0.5355$. When we compare the results of the different crystalline order parameters with CNT we notice that only the barrier with an intermediate order parameter $n_{con}^c = 7$ can be fitted with CNT. Using this crystalline order parameter the shape of the nucleus corresponds best with a spherical nucleus as assumed by CNT.

5.3.2 Nuclei

We tested whether the structure and shape of the critical clusters depend on the precise threshold values used for the crystalline order parameters. To this end we analyzed the critical clusters obtained by using three crystalline order parameters in the USS. In Fig. 5.2 two (top and bottom row) typical critical clusters of three different USS (from left to right $n_{con}^c = 5, 7, 9$ have been used in the umbrella sampling) are compared with each other using the three different order parameters. The nucleus of the cluster, shown in blue, was identified by all three cluster criteria. The main difference between the criteria is the location of the fluid-solid interface as shown by the green and red particles. The strictest order parameter only finds the more ordered center whereas the loosest version detects many less ordered particles in the interface as well. Furthermore we used the Q_5 order parameter to distinguish between particles in an FCC and HCP environment. The critical clusters seem to have a preference for FCC stacking with only 16% of the particles in an HCP environment.

If Fig. 5.3 we show some of the nuclei obtained from MD simulations. These configu-

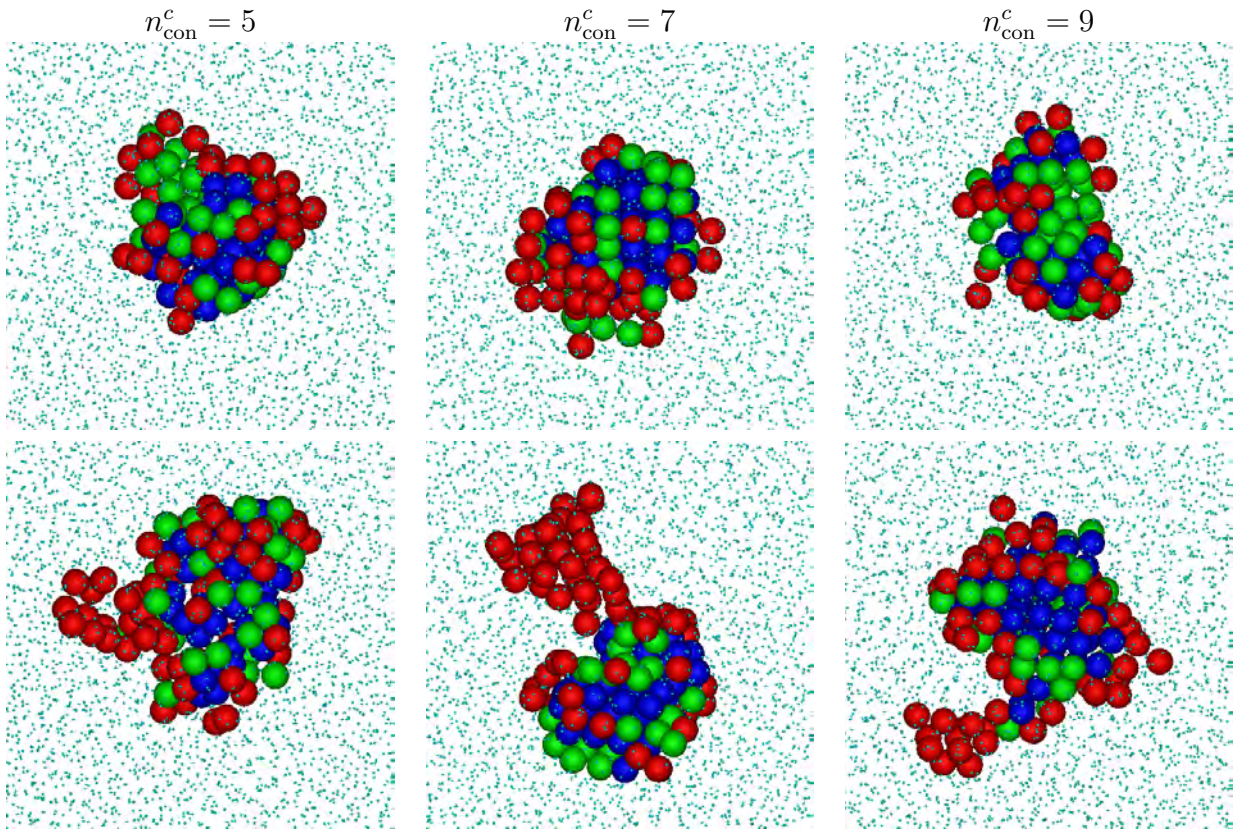


Figure 5.2: Two typical snapshots (top and bottom) of the critical nuclei as obtained with USS at a volume fraction $\eta = 0.5355$ using different values of n_{con}^c , $n_{\text{con}}^c = 5$ left, 7 middle and 9 right in the biasing potential. The clusters are analyzed with three different crystalline order parameters. The blue particles are found by all three cluster criteria, the green particles have 7 or 8 crystalline bonds and the red particles have only 5 or 6 crystalline bonds.

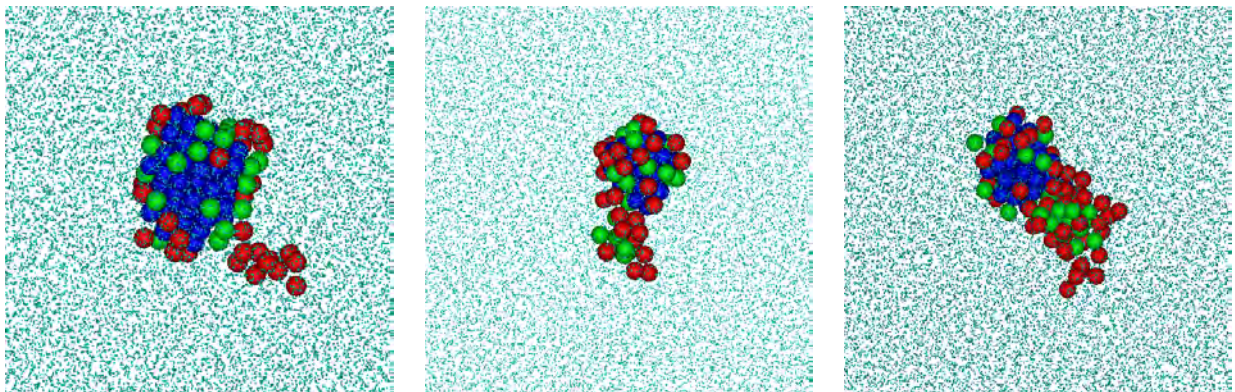


Figure 5.3: Snapshots of spontaneously formed nuclei during an MD simulation at a volume fraction of 0.537. The snapshots were taken just before the nuclei grew. The color of the particles as in Fig. 5.2.

rations are taken just before the nuclei grew out so they are not necessarily precisely at the top of the nucleation barrier. They look very similar in roughness and aspect ratio

as those obtained from USS. We did not observe critical nuclei with twinning defects as O'Malley and Snook [99]. However, their simulations were performed at volume fraction $\eta 0.539$, where we predict the critical nucleus to have a size of approximately 60 particles. The critical nuclei shown by O'Malley have an average size of 426 particles. When we examine larger nuclei in Fig. 5.4, that have grown out further, we observe similar twinning defects.

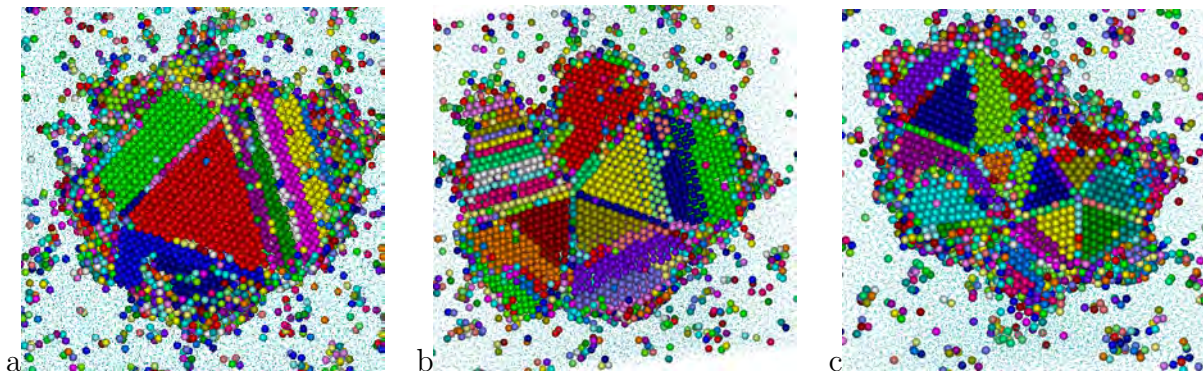


Figure 5.4: Typical snapshots of spontaneously formed nuclei during an MD simulation with 100,000 particles at a volume fraction of 0.538. The snapshots were taken while the nuclei were growing fast. The different colors indicate the different domains within the nuclei.

To analyse the domain structure of the nucleus we identify the different clusters within the nucleus that have a high Q_6 correlation of $d_c = 0.95$. In figure 5.4, the domain structure of three growing nuclei is shown. All three snapshots are the result of a single nucleation event. In Fig. 5.4(a) the nucleus consists of a large FCC domain (red) surrounded by four mostly randomly stacked domains. In Fig. 5.4(b) the center of the nucleus consists of five domains with different orientations and all merging in a single line defect. In Fig. 5.4(c) the nucleus contains two areas where 5 differently oriented domains meet. These kind of defects of five domains all meeting in one line are observed in more than half of the observed nuclei. The initial nucleus is often located close to such a defect.

The surface boundaries of the growing nuclei are very rough. Close to the defects, we observed deep crevices and at hexagonal planes there were bulges that stuck out and grew into the fluid. These results correspond well with experimental observations of growing nuclei [28, 100], where the nuclei have wild shapes with protrusions and rough edges. The rectangular shape, observed predominantly in experiments [100], is not reproduced, we expect that our nuclei are too small to observe this.

5.3.3 Kinetic prefactor

To obtain the nucleation rate when the barrier is known we need to determine the kinetic prefactor in Eq. 5.11. This kinetic prefactor can be measured using kinetic MC or MD simulations. We have chosen to use kinetic MC which was also used by others [91]. We compared our results with MD simulations and obtained the same results within the statistical error.

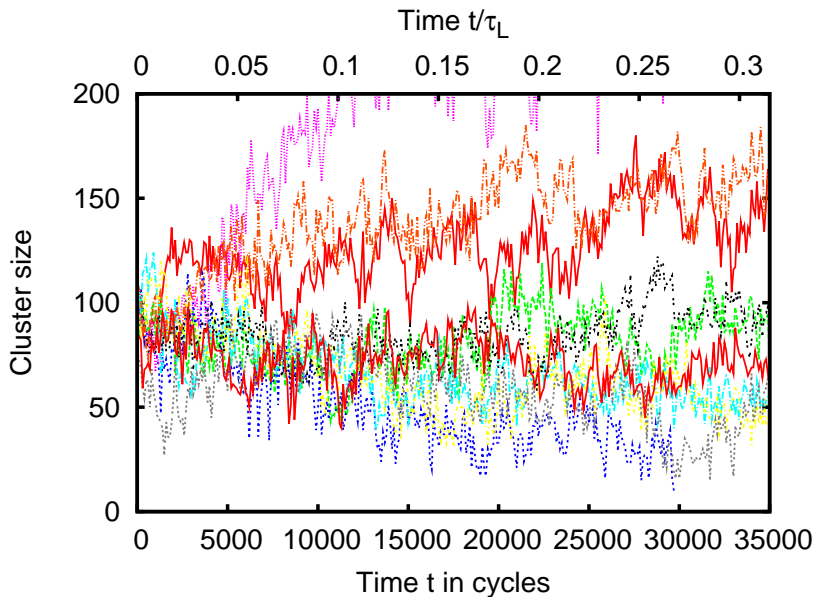


Figure 5.5: *The cluster size as a function of time (MC cycles and long time diffusion units) for a random selection of clusters that start at the top of the free energy barrier.*

The kinetic prefactor was determined using kinetic MC simulations with 3000 particles in the NVT ensemble in a cubic box with periodic boundary conditions. The initial configurations were taken from USS in one of the windows at the top of the barrier. The step size was chosen to be 0.012σ and Gaussian displacements were used. The determined the short and long time diffusion from the mean squared displacement in the metastable fluid. The short time diffusion coefficient was $D_s = \frac{1}{2}(0.012\sigma)^2$ per cycle and the long time diffusion coefficient was $D_l = D_s/48$. In Fig. 5.5 we observed that the nucleus fluctuated much faster than expected and could completely disappear or double its size within $0.3/\tau_l$ where τ_l is the time that it takes a particle on average to diffuse over a distance equal to its own diameter i.e. $\tau_l = \sigma^2/(6D_l)$.

The attachment rate was obtained from the variance or mean squared deviation of the cluster size as described by Auer et al. [97]. The variance has a different short and long time behaviour. At short time, fluctuations are caused by particles performing Brownian motion around their initial positions. The long time behaviour is caused by rearrangements of particles which is needed for the barrier crossings. At short times the slope of the variance is large, and only the fast rattling is sampled, the longer the time the further the systems have diffused away from the critical cluster size at the top of the nucleation barrier. We observed a large variance in the rates calculated for different nuclei. Some nuclei have attachment rates more than an order of magnitude higher than other nuclei of similar size. The nuclei with low attachment rates seem to have a smoother surface (and thus a smaller surface area) than the nuclei with a high attachment rate.

5.3.4 Rates

The nucleation rates have been determined using MD simulations as described in the methods section. The results are shown in Table 5.1. The nucleation times shown here

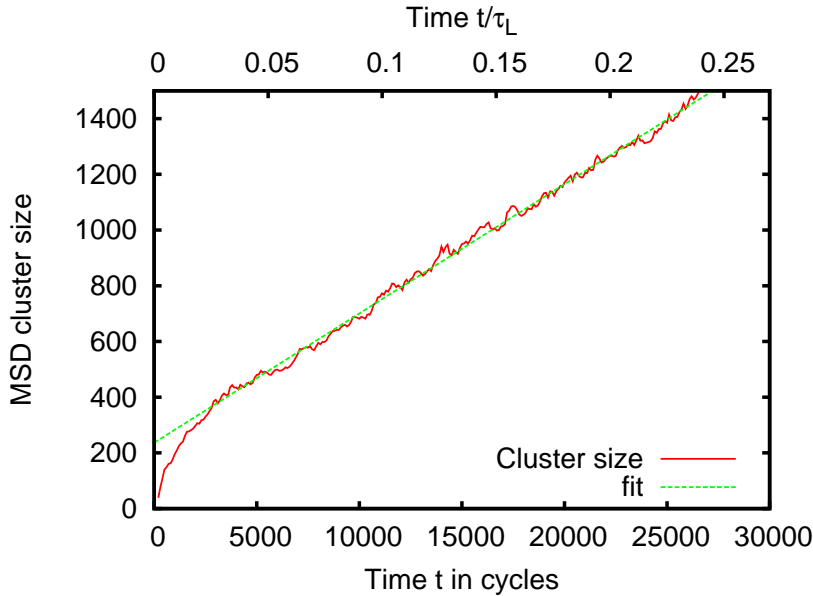


Figure 5.6: The mean squared cluster size as a function of time. The cluster size has been measured every cycle and averaged over 100 cycles to reduce the short time fluctuations. The slope of this graph is twice the attachment rate.

Volume fraction η	Average nucleation time $t\sqrt{k_B T}/(m\sigma^2)$	rate $R\sigma^5/(6D_l)$
0.5316	$1 \cdot 10^6$	$5 \cdot 10^{-9}$
0.5348	$1.7 \cdot 10^4$	$3.6 \cdot 10^{-7}$
0.5381	$1.4 \cdot 10^3$	$5.3 \cdot 10^{-6}$
0.5414	$2.0 \cdot 10^2$	$4.3 \cdot 10^{-5}$
0.5478	42	$3.0 \cdot 10^{-4}$
0.5572	10	$2.4 \cdot 10^{-3}$

Table 5.1: The average time obtained from MD simulations, before the system formed a critical cluster that grew out and filled the box. The last column contains the rate in units of $\sigma^5/(6D_l)$.

are for a system of $2.0 \cdot 10^4$ particles and in MD time units. To compare with other data we convert the MD time units to units of $\sigma^2/(6D_l)$ with D_l the long time diffusion coefficient measured in the same MD simulations. We were not able to measure the long time diffusion coefficients for high densities because our measurements were influenced by crystallization. We used the fit obtained by Zaccarelli et al. [101] who used polydisperse particles to prevent crystallization and fits our data for D_l very well for $\eta < 0.54$.

To compare the different results we have plotted the nucleation rates obtained from experiments, previous simulations, CNT, our USS and our own MD simulations in Fig. 5.7. The experiments have been performed using polydisperse particles instead of monodisperse spheres. This is expected to influence the nucleation rate significantly, however, the experimental volume fractions have been scaled to yield the coexistence densities of monodisperse hard spheres [75]. To be able to compare the simulations with the experiments we have to scale all volume fractions to the coexistence volume fraction of

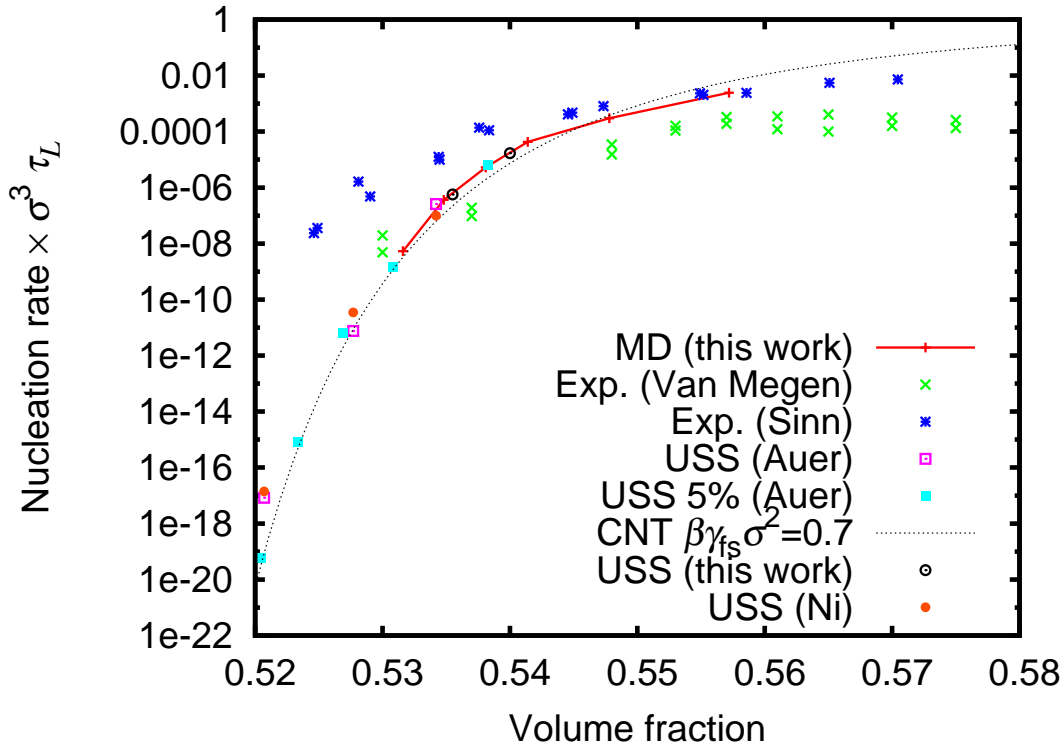


Figure 5.7: The nucleation rates obtained with different techniques as labeled. MD denotes the results obtained from spontaneous nucleation using event driven molecular dynamics simulations. USS denotes the results obtained from umbrella sampling simulations. For comparison we also plot experimental results obtained using scattering from [88, 89] and the predictions from CNT using the surface tension $\beta\gamma_{fs}\sigma^2 = 0.7$ as a fit parameter.

monodisperse hard spheres. When the five percent polydisperse results of Auer [97] are scaled with the bulk coexistence density for polydisperse hard spheres from Fasolo et al. [33], as was done in the experiments, the results for polydisperse sphere fall on top of those for monodisperse spheres.

In experiments with colloidal particles the influence of the solvent on the dynamics can not be ignored. The system slows down due to hydrodynamic interactions when the density is increased. The time in experiments is usually measured in units of D_s the free diffusion at low density. Since the long time diffusion D_l is expected to be the relevant time scale for crystallization [75] and is known for the experimental systems we can also convert the experimental times to units of D_l . Since the hydrodynamics are already taken into account in the long time diffusion we should be able to scale our results directly onto the experiments.

The experiments of Harland and van Megen[88] yield nucleation rates one order of magnitude below the experiments of Sinn et al. [89]. This is unexpected as the experimental systems are very similar. One explanation lies in the fact that van Harland used particles with 5 percent polydispersity while Sinn used particles with a polydispersity of only 2.5 percent. The effect of polydispersity on the nucleation rate of the experimental system can be corrected by taking the long time diffusion coefficient measured for the same

system as well, and hence we expect to find the same nucleation rate in units of σ^2/D_L . It is worth mentioning here that the units of [88] were not always mentioned and used consistently. Fig. 5.7 also shows that the nucleation rates obtained from MD simulations agree well with those obtained from USS calculated here and presented in [97]. Finally, we fit the nucleation rate as a function of packing fraction with CNT using the kinetic prefactor and surface tension as fit parameters. We have used the same expression as Sinn and Harland [88, 89]. We find good agreement using $\beta\gamma_{fs}\sigma^2 = 0.7$ and $\frac{\kappa\sigma^5}{6D_L} = 3.0\eta^{5/3}$.

5.4 Conclusions

We demonstrate that different simulation techniques allow us to measure the crystal nucleation rate of hard spheres. In the regime where both techniques are feasible we compare their results and find good agreement. The simulation results are fitted roughly by CNT when the kinetic prefactor and surface tension are used as fitting parameters. The experiments match the trend of the simulations but predict a higher rate for lower densities. We speculate that this is caused by the twinning defects that are formed in the growing nuclei which in scattering can not be distinguished from different nuclei. Hence, too many nucleation events are counted per volume and time unit, yielding a higher nucleation rate. This effect will be more severe at low volume fractions when the size difference between the different nuclei is expected to be larger. This could in principle be tested by calculating the scattering profile in the simulations and performing the same analysis on the peak width and height as performed in the experiments. Another possible origin of the discrepancy between simulations and experiments is that collective hydrodynamics, which are extremely density dependent, are important in the experiments.

The precise details of the order parameter used in USS does not influence the critical nucleus shape. The critical nuclei with the MD simulations are very similar to the nuclei obtained using USS. However, the cluster can be analyzed by using different order parameters. A looser cluster criterion identifies more particles as solid-like, yielding a larger crystalline cluster with a rough surface, while a strict cluster criterion yields a more compact nucleus with a smooth surface.

5.5 Acknowledgements

We would like to thank R. Ni for performing USS simulations at low supersaturation and L. Filion and F. Smallenburg for many useful discussions.

Nucleation on configurable seed structures

We studied seeded crystal growth in a system of nearly hard sphere colloids with a template of particles trapped with an optical tweezer. In addition we performed molecular dynamics simulations on a hard-sphere system with an identical template of fixed particles. We show that we can initiate the nucleation process with the template and that the template shape determines the final crystal shape and orientation. Furthermore we show that defects can play an important role in the growth of the crystal. A crystal grown on a hexagonal template has a small chance of producing a crystal containing twinning defects while a square template produces many twinning defects. These twinning defects have a tendency to produce many small domains with more twinning defects instead of one large domain. Since a spontaneously formed critical nucleus is thought to be randomly stacked we expect that these twinning defects will also play an important role in the growth of spontaneously nucleated crystals.

6.1 Introduction

Nucleation is an important stage in the growth of crystals. During this stage, the structure and orientation of a crystal are determined. However, short time and length scales make nucleation poorly understood. Micrometer-sized colloidal particles form an ideal model system to study nucleation due to more experimentally accessible time and length scales [102] and the possibility to manipulate them individually [103]. In addition, control over colloidal crystal nucleation is important for advanced materials such as photonic crystals [104]. Colloidal epitaxy on corrugated surfaces is well established [102, 105, 106], but this is not yet the case for directed nucleation in the bulk [107, 108]. Here we report experiments and simulations on nucleation in the bulk of a hard-sphere fluid, initiated by seed structures configured using optical tweezers. We find that different seed structures result in different crystal morphologies. From the growth of the crystals beyond the critical nucleus size new insights into the role of defects in crystal growth, that are incompatible with the assumption of equilibrium growth, were gained.

The primary aim of our study on the effects of small 2D nuclei brought into the bulk is to study the nucleation itself. We investigate whether the nucleation barrier can be lowered by introducing a seed and if the shape of the barrier can be explained by classical nucleation theory. Additionally, we study the subsequent growth of the crystal nucleus and investigate how the resulting crystal morphology depends on the structure of the seed. Lowering nucleation barriers in bulk and thereby increasing the nucleation rate is important for e.g. protein crystallization and electronic ink [109], while gaining control over the self assembly of colloidal systems is interesting for advanced materials such as photonic crystals [104].

In general, two types of nucleation can be distinguished: *homogeneous nucleation* in which small crystallites grow in the bulk of an undercooled or supersaturated fluid, and *heterogeneous nucleation* in which crystallites nucleate on a different substance, e.g. the surface of another crystal or on a container wall. Homogeneous nucleation can be qualitatively described by CNT: nuclei are formed continually by thermal fluctuations, but most of the time the high surface energy cost of the crystallites is not counterbalanced by the bulk free energy gain and the crystallite melts [90, 97, 110]. However, if a nucleus is formed that exceeds the critical nucleus size, the bulk free energy term overcomes the surface term and the nucleus grows out. Since the growing nuclei form randomly throughout the sample it is impossible to control homogeneous nucleation. However, crystals grown by heterogeneous nucleation can be precisely controlled by controlling the structure of the nucleating object [105].

To study heterogeneous nucleation, Cacciuto and Frenkel [111] performed Monte Carlo simulations on finite two-dimensional seed structures in the bulk of a hard-sphere fluid. They observed a pre-critical nucleus, corresponding to a local minimum in the free energy. This pre-critical nucleus could already grow out at volume fractions with very low rates of spontaneous nucleation. They found a good correspondence between the barrier heights predicted by a modified version of CNT and the nucleation rate of their simulations. They studied planar crystalline templates with the structure of the square (100), distorted hexagonal (110) and hexagonal (111) plane of a face centered cubic (FCC) structure and concluded that the hexagonal plane is the most effective in lowering the nucleation barrier.

They also suggest that the number of seed particles can be drastically reduced by choosing a larger particle spacing that is also commensurate with the crystal without effecting the effectiveness of the seed. In experiments, this would allow for larger seeds using the same number of seed particles. We investigate in experiments and simulations whether we can indeed use seeds with a large spacing to reduce the number of particles in the seed structure. Additionally, we compute the nucleation barriers for such seeds using computer simulations and we compare them with their modified version of CNT.

The free energy difference between FCC and hexagonal close-packed (HCP) crystals of hard spheres at coexistence is very small: $0.0008 k_B T$ per particle [10]. Because of this small difference homogeneously nucleated hard-sphere crystals have a random hexagonal close-packed (RHCP) structure [27, 28, 112]. The internal structure of the critical nuclei has been studied in experiments [90] and computer simulations [91, 110] both finding a RHCP structure for hard spheres. However, O'Malley *et al.* showed using molecular dynamics (MD) simulations that the structure of crystallites is more complex and consists predominantly of multiply twinned crystal nuclei that are formed by blocks of FCC crystals bound by stacking faults [99]. We investigate whether the stacking of the crystal can be influenced by choosing a square seed, which is only compatible with FCC, or a hexagonal seed, which is compatible with both FCC and (R)HCP.

6.2 Methods

The particles that formed the bulk of the experimental dispersion were PMMA particles which were completely dyed with 1,1'-dioctadecyl-3,3,3',3'-tetramethylindocarbocyanide perchlorate (DiIC) and sterically stabilized with poly(12-hydroxystearic acid) (PHS). The PHS was not locked to the particles. These host particles were $0.93 \mu\text{m}$ in diameter. The seed particles were made from polystyrene cores with a diameter of $0.99 \mu\text{m}$ onto which a thin 50 nm silica shell was grown as described in [113]. Subsequently, the silica shell was coated with 3-(trimethoxysilyl) propyl methacrylate and the PMMA-PHSA steric stabiliser [103]. The final diameter of the seed particles was $1.1 \mu\text{m}$. The solvent matched the index of refraction of the PMMA host particles at 1064 nm (the infrared wavelength of the trapping laser) and consisted of a mixture of cyclohexyl bromide (CHB) and cis-decalin. We verified that the density profile of the fluid particles remained flat in the presence of an empty optical trap. The interactions between the particles were tuned to be nearly hard-sphere-like by saturating the solvent with the salt tetrabutylammonium bromide (TBAB). The combined confocal microscopy and optical tweezers setup used in this chapter is described in Ref. [103]. The dielectrophoretic compression was obtained by a 'slit-like' geometry as described in [83]. The cell was approximately 15 mm by 8 mm by $70 \mu\text{m}$ and the slit was approximately 0.3 mm wide.

Event driven MD simulations were performed on $100,000$ hard spheres with diameter σ and mass m . The particles in the seed were fixed to their positions and the collisions with these particles were treated as if the fixed particles had infinite mass. A cubic box with periodic boundaries was used. To study whether the particles were part of the nucleus, we calculated the Q_6 bond correlation order parameters [14, 31, 114]. A distance criterion of $r_c = 1.4$ diameters was used to define the neighbors of a particle. We used $d_c = 0.6$ for

the cutoff of the bond order and $n_{\text{conn}}^c = 7$ as the minimum number of correlated bonds of a crystalline particle. Two crystalline particles with a bond correlation of 0.95 or higher were considered as part of the same crystalline domain.

We have followed the scheme of Cacciuto *et al.* to adapt CNT to a seed structure [111]. The only modification is that we have placed our seed in the middle of the crystallite since this yields a lower free energy and corresponds to the observations in our simulations and experiments. Thus the Gibbs free energy to form a crystalline cluster reads:

$$\Delta G = \gamma_{\text{fs}}S - \Delta\mu\rho_s V + E_{\text{si}} \quad (6.1)$$

where S is the surface area of the nucleus, V is the volume of the nucleus, γ_{fs} is the interfacial tension between the fluid and the solid, $\Delta\mu$ is the chemical potential difference between the fluid and the solid, ρ is the density of the solid and E_{si} is the interaction energy between the fluid solid interface and the fixed seed particles. In our case the surface area of the seed is given by:

$$S_t = \begin{cases} 2\pi(r^2 + r_s^2) & r < r_s \\ 4\pi r^2 & r > r_s \end{cases}, \quad (6.2)$$

and the volume is given by:

$$V_t = \begin{cases} \frac{\pi}{3}r(3r_s^2 + r^2) & r < r_s \\ \frac{4}{3}\pi r^3 & r > r_s \end{cases} \quad (6.3)$$

where r_s is the radius of the seed and r is the height or radius of the nucleus measured from the center of the seed. Here we assume that the cluster on the seed structure has the shape of a spherical cap of radius r_s and height r , which becomes spherical when $r > r_s$. We ignore the seed interface interactions and set E_{si} to zero. To compare with the experiments and simulations we chose r_s such that the circular seed area matched the area of the seed structure used in experiments and simulations.

6.3 Results

In this work a seed of sterically stabilised polystyrene-polymethylmethacrylate core-shell particles was trapped in the bulk of a sample filled with index-matched polymethylmethacrylate (PMMA) [115] particles using time shared optical traps [103]. The fluorescently dyed PMMA particles were imaged using a confocal microscope. The volume fraction was controlled in-situ using dielectrophoretic compression [83]. Our seed particles including all the coatings were 1.18 times larger than our PMMA bulk particles. The effect of this mismatch is discussed later. Additionally, MD simulations in the NVE ensemble were performed to study the crystal growth and Monte Carlo simulations in the NPT ensemble using an umbrella biasing potential [91] to measure the nucleation barriers. The experiments were started at a volume fraction $\eta = 0.30$ and compressed very slowly, with a total time between $\eta = 0.30$ and 0.50 of on average 180 minutes. The simulations were performed at a fixed particle volume fraction. The volume fraction was chosen such that the free energy barrier to nucleate on the seed was several $k_B T$ to ensure that the pre-critical nucleus had time to equilibrate before it grew out.

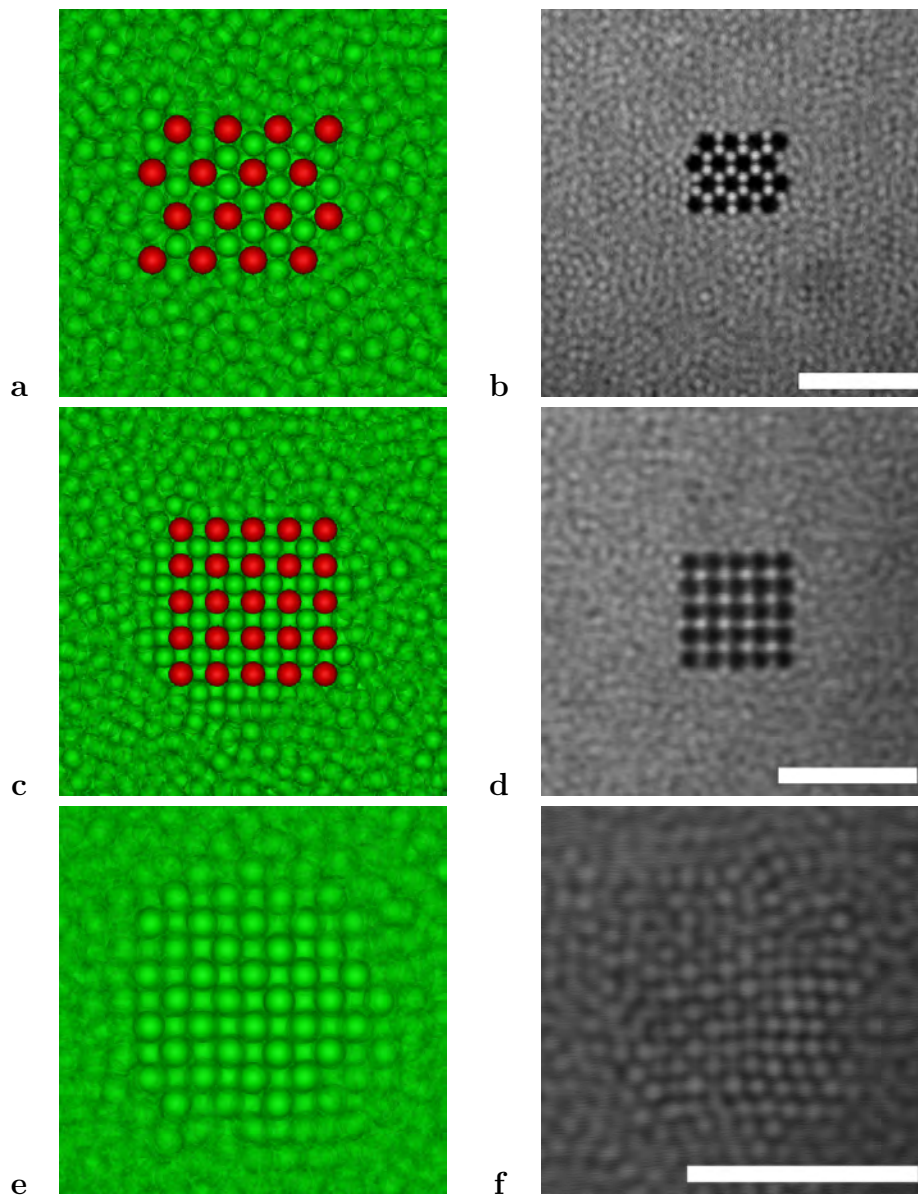


Figure 6.1: Structuring of the fluid particles around the seeds. *The particles around the seed are at a volume fraction below coexistence in (a,b,c and d). At the left (a, c and e) are time-averaged snapshots from an MD simulation and at the right (b, d and f) are time-averaged confocal images, the undyed seed particles are visible as black spots. Images (a and b) are hexagonal seeds of 16 particles with a spacing of approximately 1.56 diameters (of the free particles), (c,d,e and f) are square seeds of 25 particles with a spacing of approximately 1.91 diameters. In (e and f) are the pre-critical nuclei of approximately 120 particles one layer above the square seed structure at volume fraction $\eta = 0.51$. The scale bars are $10 \mu\text{m}$.*

The particles in the seed were not touching, and the spacing was chosen such that exactly one particle could fit in between the seed particles as can be seen in Figs. 6.1 and 6.2. The larger spacing was required in the experiments to avoid overlap of neighboring optical traps. The particle spacings were chosen to match the spacing in a solid at co-

existence as closely as possible. The spacing was $\sqrt{2} * 1.1 \approx 1.56$ diameters (of the free particles) for the square seed structures and $\sqrt{3} * 1.1 \approx 1.91$ diameters for the hexagonal seed structures. The square seeds consisted of 25 particles and the hexagonal seeds consisted of 16 particles. The seed structures in the simulations were equivalent to the ones configured in the experiments. As in the experiments, the seed particles were 1.18 times larger than the host particles.

The experiments were started at a volume fraction $\eta = 0.30$. In Fig. 6.1(a-f) we show the seeds at a volume fraction slightly below 0.494, the coexistence density of the fluid. In order to distinguish between the solid and fluid-like particles, the confocal images were averaged over (5-10) frames to emphasize the immobile particles.

Figs. 6.1(c-f) show that experiments and simulations both yielded a small FCC stacked crystal on the square seed at densities slightly above the coexistence density. In Figs. 6.1(e,f) a slice through the crystallite, one layer above the seed is shown. The simulation was performed at a volume fraction of 0.51. The volume fractions obtained from the experiments had a large uncertainty and the simulation values were well within the variance of the experimental value. When the density was increased further, the size of the critical nucleus decreased and the probability of growing beyond the critical size increased. At a volume fraction of approximately 0.515 (simulation value) the nucleus grew out beyond the critical size. Bulk nucleation at this density is still extremely unlikely [91]. The pre-critical nucleus was found to disappear when the seed particles were released, while a nucleus that was larger than the critical nucleus remained stable even without a seed. A pre-critical nucleus was never found on the hexagonal seeds neither in simulations nor in experiments (see Figs. 6.1(a,b)). The hexagonal nucleus did grow out but at a higher density, which is estimated by simulations to be at a volume fraction of 0.535. Thus it is indeed possible to use a larger particle spacing to lower the nucleation barrier, however, the square seed does this more efficiently than the hexagonal seed.

Typical results for crystals that grew beyond the critical nucleus size are shown in Fig. 6.2. The square seed structure generated an FCC initial nucleus on the seed visible in Fig. 6.2 (a,b). Outside the range of the seed, the crystals were randomly stacked and contained many small domains. There was no sign yet of bulk crystallization. The crystals were always more or less spherical but had very rough surfaces with deep crevices at the domain boundaries (Figs. 6.3 and 6.4). In the case of hexagonal seeds, visible in Figs. 6.2 (c,d), most nuclei consisted of a single RHCP domain. In the experiments the first small bulk nuclei are also visible. We observed a tendency for a cylindrical crystal shape. From these observations we conclude that the initial stacking of the 3D nucleus that grew on the 2D seed after reaching the critical nucleus size plays an important role in the growth and incorporation of defects in the crystal.

In Fig. 6.3 we take a closer look at typical defect structures of the growing crystals. In the simulations we used the 3D Q_6 bond correlation order parameter, as described in the methods section, in order to distinguish different domains inside the crystal. It was not possible to obtain reliable 3D coordinates from the experimental images, therefore all major defects were marked by visual inspection (a two dimensional local bond order analysis gave very similar results). Almost all RHCP crystals grown on hexagonal seeds were completely free of 2D and 3D defects and contained only a few point defects (examples are given in Figs. 6.3c,d). On the other hand, the crystals grown on the square

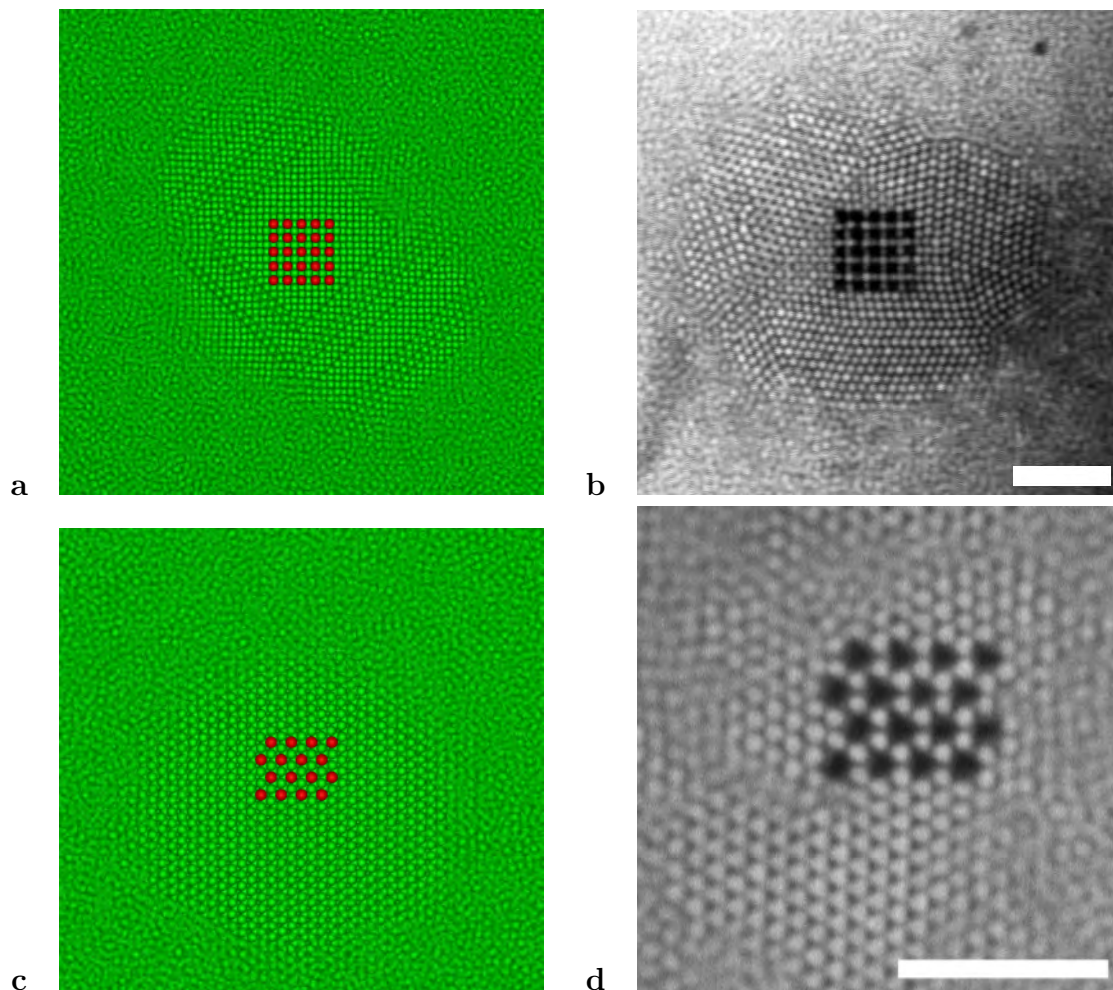


Figure 6.2: Crystals growing on 2D square and hexagonal seeds. *The crystal on the square seed has grown beyond its critical size at a volume fraction of 0.515 at which the critical size is approximately 400 particles. The crystal on the hexagonal seed has grown beyond its critical size at a volume fraction of 0.535. At the left (a and c) are snapshots from an MD simulation when the crystal was approximately 3×10^4 particles and at the right (b and d) time-averaged confocal images. At the top (a and b) a square seed structure with a spacing of 1.56 diameters (of the free particles) and at the bottom (c and d) a hexagonal seed structure with a spacing of approximately 1.91 particle diameters. The scales bars are 10 μm .*

seeds contained many defects. A central FCC-stacked domain originated from the seed and followed the (100) plane induced FCC structure. This central FCC domain has eight hexagonal planes on the outside. When the FCC domain had grown outside the reach of the seed, differently stacked domains formed on some of these hexagonal faces, with twinning defects in between, see e.g. Figs. 6.3 (a,b) and 6.4. This could not happen on the hexagonal seed since the RHCP nucleus only has hexagonal planes on the bottom and top faces. To illustrate the broad range of crystal morphologies that was observed for a square seed structure a few typical ones are depicted in Fig. 6.4.

To investigate why the pre-critical nuclei were seen on the square seeds and not on

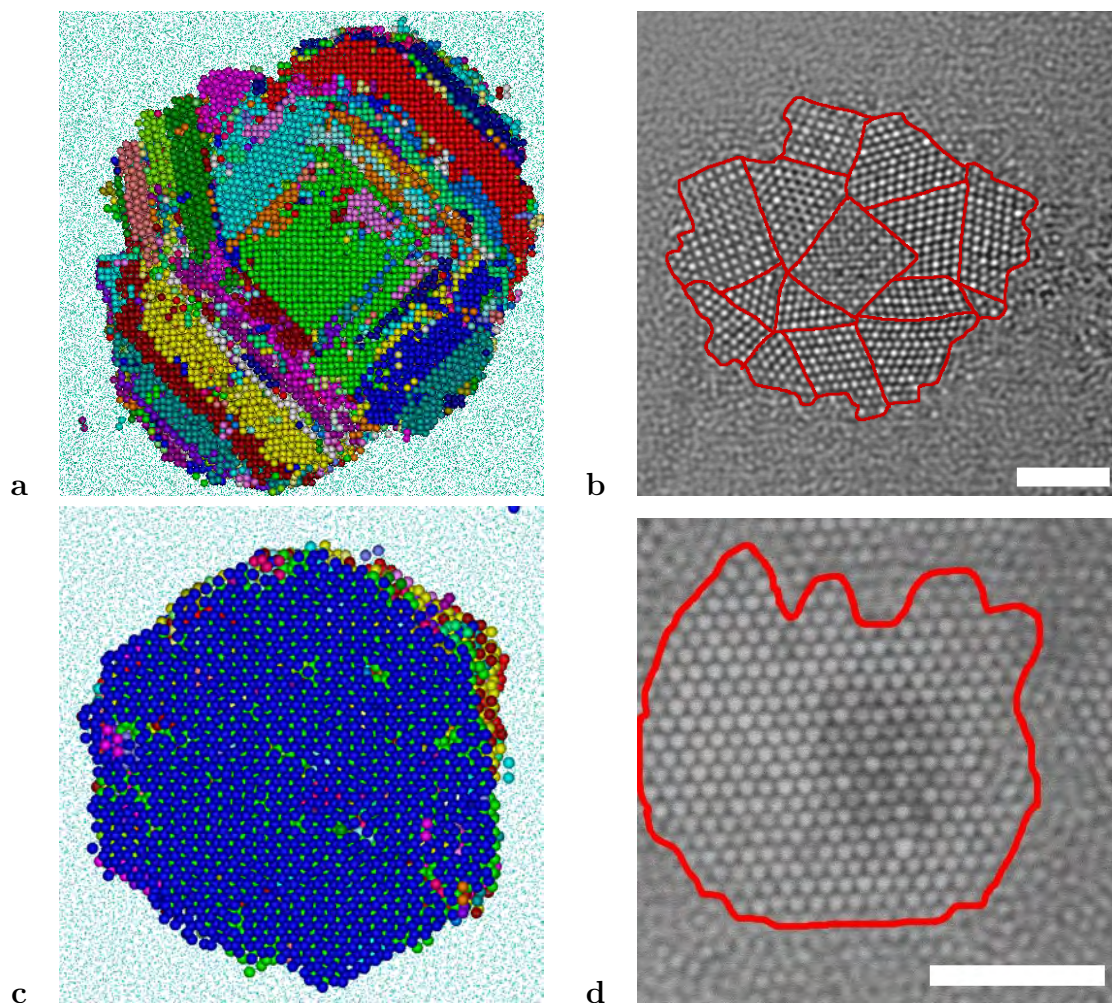


Figure 6.3: Defect structures of the growing crystals 2 layers above the seeds. *The square (a,b) and hexagonal (c,d) seed simulations on the left, experimental data on the right. In the simulations (a,c) a cluster criterion based on Q_6 was used to determine the crystallinity of the particles there are $4 * 10^4$ crystalline particles in (a) and there are $3 * 10^4$ crystalline particles in (c). The crystalline particles are drawn at their normal size and the fluid particles are drawn as dots. A cluster criterion was used to color the different domains. In (b,d) we show, experimental, time-averaged scans to distinguish the fluid from the crystal-like particles. Lines were drawn where irregularities in the crystal were observed. The scale bars are $10 \mu\text{m}$.*

the hexagonal seeds, the nucleation barriers were calculated using umbrella sampling in Monte Carlo NPT simulations. In Fig. 6.5a, the free energy barriers for a four-by-four hexagonal seed with a spacing of 1.91 are plotted. The barriers obtained with umbrella sampling simulations correspond well with our observations in both experiments and MD simulations. There is no metastable pre-critical nucleus since the metastable free energy minimum is always at nucleus size zero. However, the modified CNT as described in the section 6.2, does not match with the other results and predicts barriers that are too low and do have a metastable minimum at finite nucleus size. In Fig. 6.5b, the barriers for a four-by-four square nucleus and spacing of 1.56 particle diameters are plotted. At low

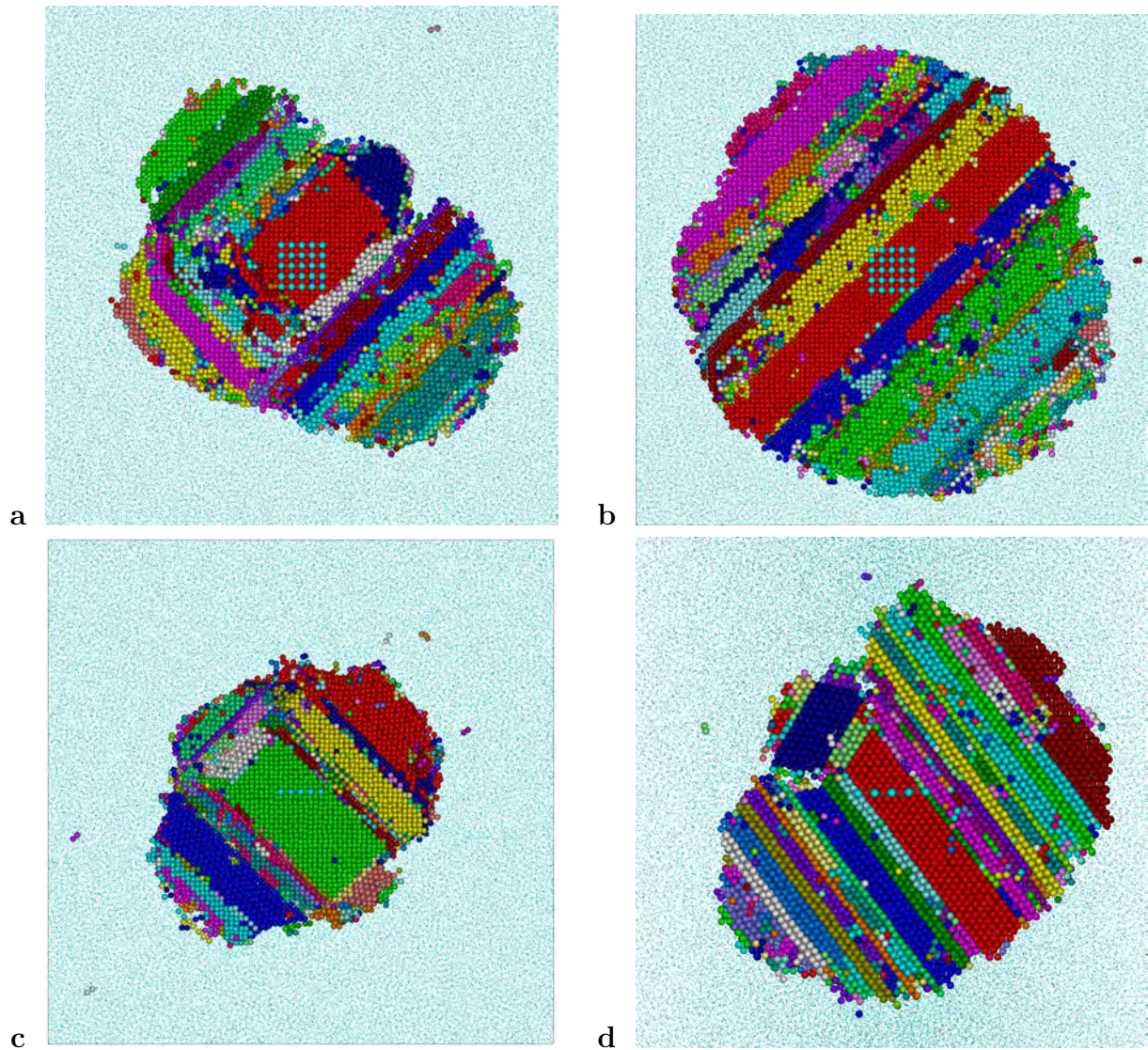


Figure 6.4: Snapshots from MD simulations illustrating the different defect structures that were observed on a square seed. The MD simulations were performed with $1 * 10^5$ particles on a square seed of 25 particles and a spacing of 1.56 diameters. The fluid particles are drawn as dots. The particles are colored according to the Q_6 criterion described in the methods section. **a)** has a tetrahedral central FCC domain which occurred in 40% percent of our MD simulations (there are $9 * 10^4$ particles in the crystal). **b)** has a central FCC domain that is flat, which was observed in 30% of the simulations (there are $17 * 10^4$ particles in the crystal). **c)** has a central FCC domains that is bound by six defects. The view is perpendicular to the plane of the seed (there are $5 * 10^4$ particles in the crystal). **d)** has a central FCC domain that is very similar as b but with an additional twinning defect (there are $7 * 10^4$ particles in the crystal).

density a local free energy minimum was found at finite nucleus size. When the density was increased, the free energy barrier between this finite nucleus and the crystal phase lowers until it has completely disappeared at a volume fraction between 0.515 and 0.520.

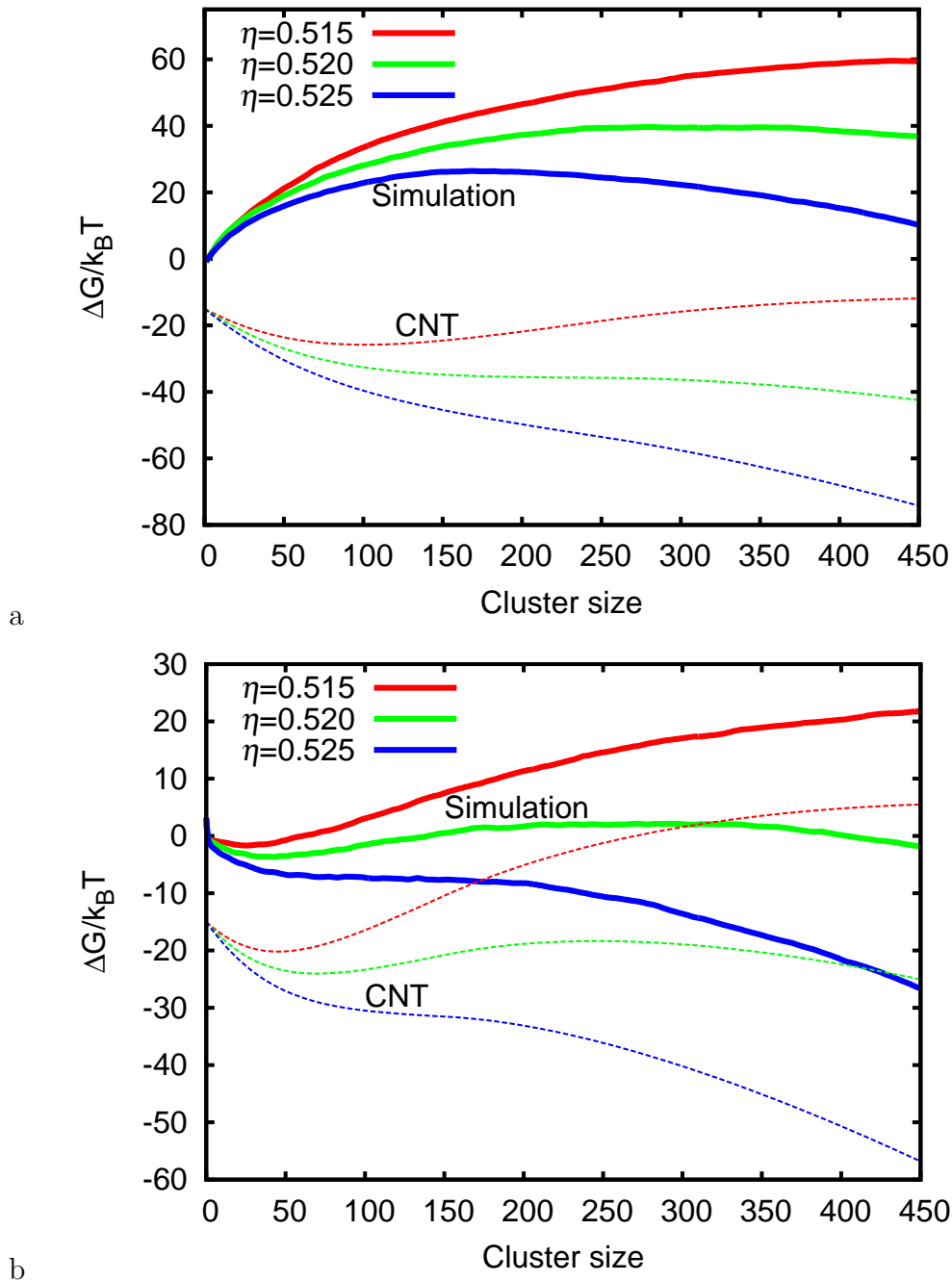


Figure 6.5: The free energy barriers between fluid and crystal nucleating on preset 2D seeds obtained with *NPT* umbrella sampling and modified CNT. The CNT barriers are offset $-15k_B T$ for clarity. **a)** The solid lines are of a four-by-four hexagonal seed with a spacing of 1.91 diameters, the dashed lines are obtained from CNT with surface tension $\beta\gamma_{fs}\sigma^2 = 0.66$. The different colors stand for different volume fractions (as labeled). **b)** The solid lines are for a four-by-four square seed and not five-by-five as our experiments. The spacing is 1.56 diameters, the dashed lines are obtained from modified CNT with a surface tension $\beta\gamma_{fs}\sigma^2 = 0.66$.

The critical size and the size of the metastable nucleus obtained from the calculated barriers agrees well with the values obtained from the experiments, the MD simulations and the modified CNT as described in the section 6.2. However, the precise barrier shape does differ slightly from the CNT barriers. This is most likely caused by the particle spacing and the seed-interface interaction which are both not taken into account in the modified CNT.

To investigate if the larger diameter of the seed particles was the cause of the discrepancy between CNT and the other results on the hexagonal seeds, we also performed simulations with seed particles of the same size as the free fluid particles. For the square seed the free energy barriers were found to be very similar to the ones with 1.18 times larger seed particles at a slightly higher density (0.005 increase in volume fraction). In the case of hexagonal seeds the barriers were substantially lowered but still no metastable pre-critical nuclei were observed. Cacciuto *et al.* [111] have shown that for a seed structure with a spacing of 1.1 diameters there exists such a metastable free energy minimum. To investigate whether the large particle spacing was the cause of the absence of a pre-critical nucleus in our experiments we also performed simulations with a square seed with a spacing of 2.2 particle diameters. These simulations also yielded barriers without a pre-critical nucleus. From these observations it can be concluded that the formation of a metastable pre-critical nucleus and the effectiveness of lowering the nucleation barriers of 2D seeds depends strongly on the lattice spacing.

6.4 Conclusion

In conclusion, we have shown that the nucleation barrier can be lowered by introducing a seed structure into the bulk of an supersaturated fluid. However, contrary to what was suggested by Cacciuto *et al.* [111] it was found that non-touching seed structures are less effective when the particle spacing exceeds a certain threshold. The large spacing of the hexagonal seeds combined with the large size of our seed particles results in barriers that are only slightly lower than the nucleation barriers in the bulk. However, the square seed worked remarkably well and resulted in nucleation at low supersaturation. The modified CNT from Cacciuto *et al.* [111] works fairly well for our square seeds but fails to describe the barriers of our hexagonal seeds. We have shown that the structure of the initial nuclei that grow further determines not only the shape and orientation but also the domain size and crystal/defect morphology of the resulting crystal. While the square seeds lower the nucleation barrier significantly, they result in crystals with more defects than the hexagonal seeds and do not lead to large FCC crystals. Our results on the defect-rich crystals grown on square 2D seeds also strongly indicate that non-equilibrium pathways may become important early on in the crystal growth in many experimental studies on hard-sphere crystal growth. In future work we would like to extend the methodology started here with 2D seeds to study nucleation on permanent self-assembled 3D seeds.

6.5 Acknowledgements

I would like to acknowledge: M.E. Leunissen and E.C.M. Vermolen for performing the experiments described in this section and D.L.J. Vossen for particle synthesis and the initial experiments.

Shear induced order

We investigated the non equilibrium phase behaviour of colloidal hard spheres in oscillatory shear. For the first time we were able to follow in real space and real time the formation of shear induced crystallization. We focused on the regime where hard-sphere crystallization can be induced by shear while the unperturbed system is still in the fluid regime. We found five different phases under conditions of varying frequency and amplitude: four known phases and one new phase. The fluid, a sliding layer phase, an twin FCC phase and a string phase were all observed in light scattering experiments and also seen by us. We also find a tilted layer phase. We confirm the structures and sliding mechanisms proposed by Ackerson for the four known phases. The formation of all phases occurred via nucleation and growth and the melting, when the shear was stopped, started on the edges and the defects of the crystal phases. The string and the tilted layer phases were very unstable without shear and melted very quickly, whereas the twin FCC and the sliding layer phases melted slowly contrary to what was observed before by Wu et al. on shear induced crystal formation in the (unperturbed) coexistence regime.

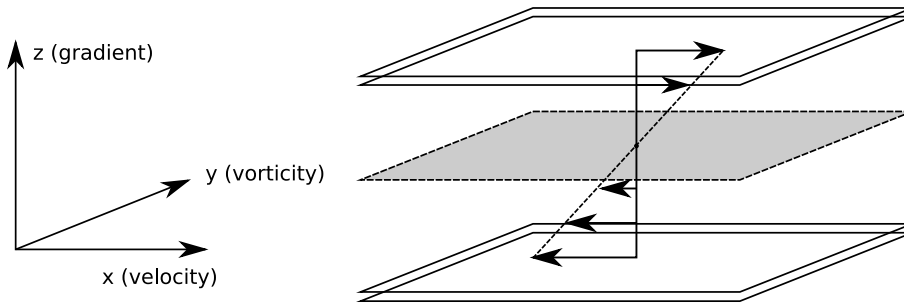


Figure 7.1: *Laminar (Couette) flow between parallel plates. The top plate is moving to the right and the bottom plate is moving to the left. The gray plane depicts the zero velocity plane, which can be moved in the z -direction by changing the relative velocities while keeping the difference constant. The z -direction is in the direction of the velocity gradient, the x direction is parallel to the shear velocity and the y -direction is in the vorticity direction.*

7.1 Introduction

The response of materials to a shear stress provides information about their basic physical properties. A fluid exposed to shear stress will start to flow whereas a solid can resist a finite amount of stress before it yields. In principle every material responds like a solid on short time scales and as a fluid for long time scales. For crystals the time scale required to observe a fluid like response can be extremely long whereas for liquids the timescale required to observe a solid like response can be extremely short. Colloids are an ideal model system for the study of materials under shear. Besides its fundamental physical interest the behaviour of colloids under shear flow is also important for many applications ranging from paint and food to smart shock absorbers and the transport of particles in blood vessels.

Uniform shear stress can be applied to a sample by moving two opposite plates as shown in Fig. 7.1 and in reference [116]. For ordinary Newtonian liquids the velocity profile will be linear and the slope will be given by the viscosity. For more complex fluids the profile may be non-linear and/or discontinuous shear-banding may occur [117]. In this chapter only two types of shear: steady shear and oscillatory shear will be discussed. In steady shear the plates move at a constant velocity whereas in oscillatory shear the plates move back and forth. Throughout this chapter we use the convention that the x axis is along the velocity direction, the y axis is along the vorticity direction and the z axis is along the gradient direction.

Earlier studies on colloidal suspensions under shear used light, x-ray or neutron scattering. These scattering techniques are good at measuring averaged quantities such as the global structure but yield little information about the details of the single particles behaviour. We use confocal microscopy which allows us to observe individual particles in time. In this chapter we will focus on colloidal dispersions close to the order disorder transition.

7.1.1 Steady shear

Blaak et al. [118] have shown using computer simulations of Yukawa particles, without hard core, that at low shear rates steady shear will slow down the nucleation rate. They used umbrella sampling simulations to calculate the nucleation barriers of a metastable fluid with a low nucleation barrier in the absence of shear. They show that the nucleation barriers become higher when shear is applied. It is expected that this system can be compared with a colloidal system that is so highly charged that the hard cores never come into contact. String formation and shear stabilized order have been observed at high shear rates in early simulations of steady shear [119]. However, the validity of these simulations has been questioned [120]. The problems referred to occur in simulations when the thermal velocity of the particles is of the same order of magnitude as the velocity difference with nearest neighbors due to the shear. If a thermostat is implemented such that the colloidal particles lose their excess kinetic energy immediately they can not move fast enough to be able to move out of the way of passing particles. As a result the system jams in an amorphous structure and shear thickening is observed. If the particles are allowed to temporarily gain more velocity strings might form [121]. To conclude, steady shear at low volume fractions with a low shear rate slows down crystal nucleation whereas at high shear rates a string phase might form depending on the details of the dynamics.

At the opposite end of the metastable fluid regime, near the glass regime, steady shear is known to speed up the formation of crystals. In glasses crystallization is not slow because of high nucleation barriers, but because the dynamics of the glass is extremely slow [75]. Shear increases the mobility of nearly jammed systems and makes it possible for glassy systems to nucleate within experimentally accessible time scales.

Wu et al [122] have performed steady shear experiments on nearly hard spheres in the coexistence regime. They have shown that nucleation does not happen through the expected nucleation and growth but that nucleation happens gradually and at all locations in the sample at the same time without the formation of a nucleus. They also showed that shear induced melting at high shear rates is a gradual transition that happens through the appearance of fast fluctuating disordered domains.

Simulations in which the hydrodynamics of colloidal dispersions under steady shear are taken into account have been performed. Most of these simulations have been Stokesian dynamics simulations based on the method Bossis et al. [123]. It has been shown that the lubrication forces play an important role at high shear rates and even break down for perfectly hard spheres [124]. The differences between Brownian dynamics simulations without hydrodynamics and Stokesian dynamics have been discussed [125]. The hydrodynamics dynamics depend strongly on the details of the system such as the stabilization of the particles. As far as we know no Stokesian dynamics simulations have been performed on oscillatory shear.

7.1.2 Oscillatory shear

Oscillatory shear has been applied by Scott et al. [126] on a granular system of steel spheres to increase the order of the system. Since then oscillatory shear has been used in

many experiments to increase the crystalline order of nearly jammed systems [127]. Not only jammed and glassy systems but also gels can crystallize by oscillatory shear [128], and even in stable fluids ordered structures can be formed under the influence of oscillatory shear [129]. Steady shear is quite different from oscillatory shear. Steady shear tends to increase nucleation barriers and slows down nucleation whereas oscillatory shear does the opposite when the amplitude is close to unity. Oscillatory shear with a large amplitude should yield the result as steady shear.

One of the first systematic studies of oscillatory shear on the phase behavior of colloids has been performed by Ackerson and Pusey [129, 130]. They performed light scattering experiments below the equilibrium coexistence density and observed shear induced structure formation. Ackerson observed with increasing strain amplitude the following four phases: a fluid or amorphous phase, a twin FCC phase, a sliding layer phase and a string phase.

The twin FCC structure is observed at low strain amplitude $\gamma_{\max} < 1$ and consists of hexagonal layers in which the close packed lines of particles are oriented in the vorticity direction. The structure is called twin FCC because during the oscillating shear the layers shift from ABC stacking at one extremum of the oscillation to ACB stacking at the other extremum of the oscillation. This structure can only occur when adjacent layers did not shift more than one particle diameter relative to each other.

When the twin FCC phase can no longer accommodate the strain it changes into a sliding layer structure. The sliding layer structure consists of hexagonal layers with the close packed lines of particles in the velocity direction. The planes shift in a zig-zag pattern between the holes in the neighboring layers. Ackerson has observed that for higher Peclet numbers and lower volume fractions the amplitude of the zig-zag decreased and the layers moved in straighter lines. The twin FCC and the sliding crystal phases have also been observed in real space experiments performed by Haw et al. [131]. They were not able to study the structure in three dimensions and focussed on nucleation from the high density glass regime.

The string phase is the most elusive and shows up in the scattering experiments as two weak intensity maxima and four elongated maxima. A string phase has also been observed in Brownian dynamics simulations with oscillating shear and particles interacting through a screened Coulomb potential [132]. The string phase in these simulations consists of strings of particles aligned along the velocity direction. These strings are ordered in a hexagonal structure in the vorticity-gradient plane with a close packed line of particles in the vorticity direction. The strings, although oriented along the velocity direction, do not maintain a uniform separation within the string. Butler et al. [120] performed non equilibrium Brownian dynamics simulations on particles interacting with a screened Coulomb potential. The scattering patterns calculated from the string phase observed by Butler et al. and the scattering pattern observed in experiments by Ackerson are very similar making it likely that this was indeed the structure observed in the experiments.

The effect of polydispersity on the twin FCC and sliding layer phases has been investigated using simulations by Komatsugawa and Nose [133]. They performed non equilibrium molecular dynamics simulations [134] on particles interacting through a Weeks Chandler Anderson potential [135]. They observed very little effect of a polydispersity that was smaller than 6%. At a polydispersity of 8% or higher they no longer observed a twin FCC

phase.

The first experiments by Ackerson were performed using nearly hard sphere PMMA particles. Yan et al. [136] performed oscillatory shear experiments on charged silica particles with double layer thicknesses on the order of the particle size in which they observed twin FCC and sliding layer structures far below coexistence. Their experiments were hindered by sedimentation which makes a direct comparison of volume fractions difficult. Later Paulin et al. [137] performed light scattering experiments on soft microgel PMMA spheres which they modelled with a $1/r^{20}$ potential. They observed the same four phases, including the string phase but at higher strain amplitudes. The string phase of these soft particles was even more pronounced than for hard particles with clear stripes in the scattering pattern. In Brownian dynamics simulations of Lennard Jones particles in oscillatory shear the same twin FCC and sliding layer structures have been observed [138]. This indicates that these structures are quite general and can be expected to appear in more systems of spherical particles.

To summarize, four different phases have been observed in simulations and experiments: the fluid or amorphous phase; the twin FCC phase that hops between ABC and ACB stacking; the sliding layer phase in which hexagonal layers slide over each other and the string phase in which strings are formed in the velocity direction with hexagonal order in the gradient-vorticity plane. To date no simulations have been performed on hard or nearly hard spheres in which all four phases were observed. The hexagonal layers of the twinning FCC and sliding layer phases have been reported in real space but the string phase has never been observed in real space.

In this chapter we compare the three dimensional structures observed in real space using confocal microscopy with structures observed in light scattering experiments by Ackerson [130]. We construct a non-equilibrium phase diagram and compare it with the phase diagram of Ackerson [130]. We show that oscillatory shear with the right parameters can induce order in an bulk equilibrium fluid of hard spheres.

7.2 Methods

The microscope used was a Leica TCS-SP2 confocal scanning laser microscope mounted on an upright Leica microscope frame. The 543 nm line of a green HeNe laser was used to excite the RITC. The objective used was a 100x, 1.4 NA objective. We varied the voxel size and resolution of the stacks we made depending on the scan speeds and resolution required to obtain accurate data. For the 3D data stacks of the unstable phases we used small frames of 128 or 256 scan lines and bidirectional scanning to increase the frame rate. For the more stable structures we used 512x512 pixels per frame and one directional scanning. We used a minimum of 5 pixels per particle diameter in all three direction and more pixels per particle diameter if possible.

The shear cell we used is a parallel plate shear cell in which both top and bottom plate can be moved independently [116]. The shear cell was mounted on the inverted confocal microscope. The bottom plate was 24 by 50 mm smooth glass plate that was 0.13-0.16 mm thick and the top glass plate was a 10 by 33 mm smooth glass plate that was 0.5-0.6 mm thick. Both top and bottom plate rested on three ball bearings of which the height

could be adjusted. The distance between the plates could be adjusted between 20 and 200 μm , we used approximately 80 μm for the experiments described in this chapter. The plate position was determined using the confocal microscope in reflection mode. The plates were aligned by repeated adjustments of ball bearings until there was no noticeable change in height when the plate was moved from one extremum to the other. The plates were driven using piezo stepper motors which were controlled using a computer. The amplitude of the oscillations of the top and bottom plate could be tuned such that the zero velocity plane could be positioned at any height in the sample. More details can be found in [116].

We express in this chapter length in units of the particle diameter σ and time in units of the Brownian diffusion time $\tau_B = \frac{\sigma^2}{4D} = 10.1$ seconds. We left out a factor of $4/6$ since this seems to be the accepted standard in the shear literature. The position of the top plate as a function of time was $x_{\text{top}} = A \sin(2\pi ft)$ and the bottom plate $x_{\text{bottom}} = -A \sin(2\pi ft)$. We define the strain amplitude as $\gamma_{\text{max}} = 2A/h$ [130] with A the amplitude of the oscillation at the top and bottom plate and h the distance between the plates. Note that Ackerson defined this as the peak to peak distance of the oscillation $\gamma_{\text{Ackerson}} = 4A/h$. The shear rate is defined as $\dot{\gamma}_{\text{max}} = 2\pi f \gamma_{\text{max}}$.

The experiments were performed with 2.0 μm polymethylmethacrylate (PMMA) particles dyed with rhodamine isothiocyanate (RITC). The polydispersity was less than 2.5%. They were dispersed in a density matching mixture of cyclohexyl bromide (CHB) and cis-decaline that contained 74.2 weight percent CHB. The CHB was saturated with the salt tetrabutylammonium bromide (TBAB) to obtain nearly hard spheres resulting in a screening length $\kappa^{-1} \approx 0.15 \mu\text{m}$. Particle coordinates were obtained using a particle tracking program implementing the algorithm described by Crocker and Grier [79] adapted to 3D.

The volume fractions were obtained by scaling to the densities of the coexisting fluid and solid phase of hard spheres. We made four samples of increasing density in the coexistence regime and measured the percentage of each sample that had crystallized after 22 hours. We obtained a ratio of 1.23 between the weight ratio $m_{\text{PMMA}}/m_{\text{tot}}$ and the actual volume fraction with a fluid coexistence at a weight ratio of $m_{\text{PMMA}}/m_{\text{tot}} = 0.40 \pm 0.01$ and the solid coexistence at weight ratio 0.44 ± 0.01 .

To study the development of order during shear we performed a two dimensional analysis in the zero velocity plane. To this end we calculated the two dimensional global bond order parameter Ψ_6 [139]. We define a bond between particles i and j at positions \mathbf{r}_i and \mathbf{r}_j when $|\mathbf{r}_j - \mathbf{r}_i| = |\mathbf{r}_{ij}| < 1.5\sigma$. The global bond order parameter is defined as

$$\Psi_6 = \left| \frac{1}{N_B} \sum_{n=1}^{N_B} \exp(6i\theta_n) \right| \quad (7.1)$$

where N_B is the total number of bonds in the image and θ_n is the angle \mathbf{r}_{ij} makes with the y axis. When the lattice is perfectly hexagonal $\Psi_6 = 1$ and when the sample is fluid $\Psi_6 = 0$.

To investigate the order in three dimensions the three dimensional bond order parameters Q_m are calculated [14]. In the calculation of the bond order parameter a list of ‘‘neighbours’’ is determined for each particle. The neighbours of particle i include all

particles within a radial distance r_c of particle i , and the total number of neighbours is denoted $N_b(i)$. A bond orientational order parameter $q_{l,m}(i)$ for each particle is then defined as

$$q_{l,m}(i) = \frac{\frac{1}{N_b(i)} \sum_{j=1}^{N_b(i)} Y_{l,m}(\theta_{i,j}, \phi_{i,j})}{\left(\sum_{m=-l}^l |q_{l,m}|^2\right)^{1/2}} \quad (7.2)$$

where $\theta_{i,j}$ and $\phi_{i,j}$ are the inclination and azimuth of the bond between i and j and $Y_{l,m}(\theta, \phi)$ are the spherical harmonics with $m \in [-l, l]$. Solid-like particles are identified[31] as particles for which the number of connections per particle $n_{con}(i)$ is greater than a critical number denoted n_{con}^c and where

$$n_{con}(i) = \sum_{j=1}^{N_b(i)} H(d_l(i, j) - d_c), \quad (7.3)$$

H is the Heaviside step function, d_c is a threshold value, and

$$d_l(i, j) = \sum_{m=-l}^l q_{l,m}(i) \cdot q_{l,m}^*(j). \quad (7.4)$$

We used $m = 6$, $r_c = 1.4$, $d_c = 0.7$ and $n_c = 6$ to determine whether or not a particle is crystalline. To determine if a particle is HCP or FCC stacked we used $m = 5$, $d_c = 0.5$ and $n_c = 4$. More details about the order parameter can be found in the introduction of this thesis.

We obtained the structure factor from the particle coordinates

$$S(\mathbf{k}) = \frac{1}{N} \sum_{i=1}^N \sum_{j=1}^N \exp(i\mathbf{k} \cdot (\mathbf{r}_j - \mathbf{r}_i)) \quad (7.5)$$

where \mathbf{r}_i is the position of particle i . We chose the \mathbf{k} vectors such that $k_j = n2\pi/L_j$ with L_j the length of the sample in the j direction and j is x, y or z and n in integer. To avoid artifacts caused by the box shape we applied a cosine window.

7.3 Results

We have observed five different phases in our experiments on oscillatory shear. The tilted layer phases has not been observed before. We will discuss these phases in order of increasing strain amplitude. The fluid or amorphous phase is observed at low strain amplitude and its structure does not differ from a normal stable hard sphere fluid. The experiments were performed at volume fractions in the range 0.47-0.49, just below freezing.

7.3.1 Sliding layer and twin FCC phase

The sliding layer and twin FCC phase that were observed had the structure that was predicted from the scattering patterns by Ackerson [130]. In Fig. 7.2 we compare confocal images of the layers with the predicted structures. In both cases the close packed sliding

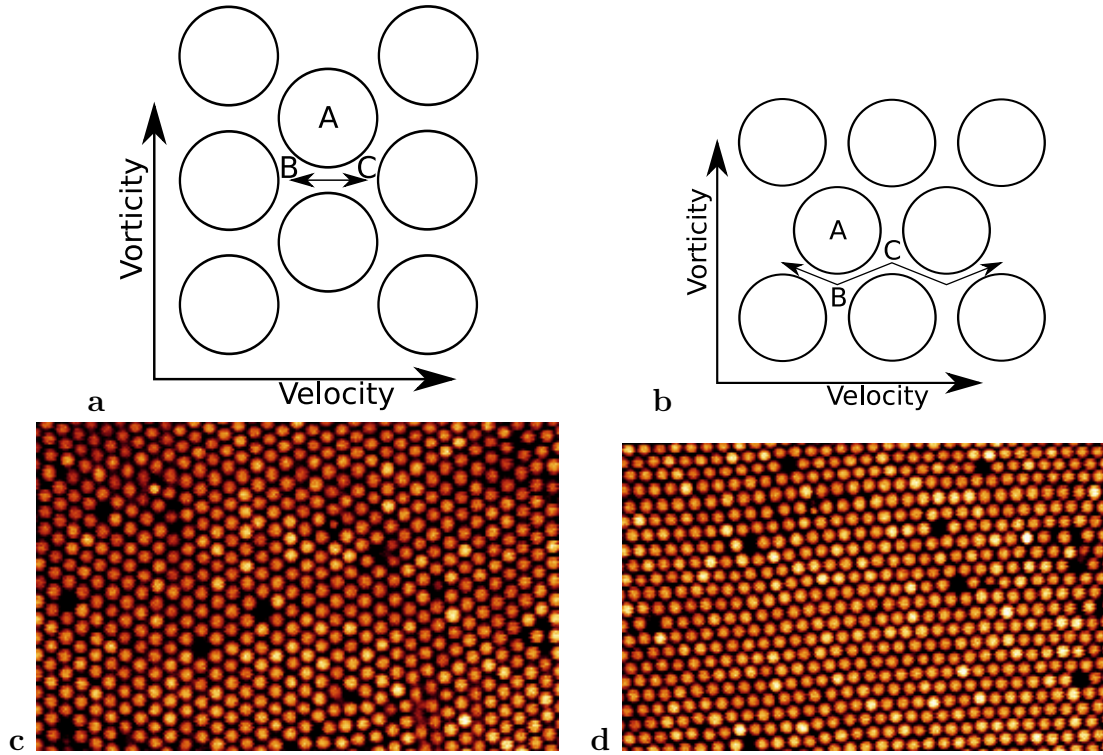


Figure 7.2: **a)** A close packed layer of a twinning FCC crystal. The close packed lines are oriented in the vorticity direction and the layers above and below move as indicated by the arrow. In one extrema of the oscillation the layers are ABC stacked and in the other extrema they are ACB stacked. **b)** A close packed layer of a sliding layer structure. The close packed lines are oriented in the velocity direction. The arrow indicates the movement of the layers above and below. **c)** A confocal image of the xy plane of the twin FCC structure at a strain amplitude of 0.3 and a frequency of $3 \tau_B^{-1}$. **d)** A confocal image of the xy plane of the sliding layer structure at a strain amplitude of 2.5 and a frequency of $8 \tau_B^{-1}$.

planes were parallel with the direction of shear. However, in case of the twin FCC crystal the layers were oriented with the close packed lines in the vorticity direction whereas in the sliding layer structure the close packed lines were oriented in the velocity direction.

To analyse the three dimensional structures the particle coordinates were obtained as described in the methods section. In Fig. 7.3 we show reconstructed configurations of three dimensional confocal stacks taken immediately after cessation of the shear. The volume fraction, at which these configurations were taken, was $\eta = 0.47 \pm 0.01$ the frequency was $4.0/\tau_B$ and the strain amplitude was 0.27. These configurations are from the center of the gap. The crystal that formed was metastable since the density was below the coexistence density of the fluid but we were able to finish a confocal stack before it melted. When the shear was stopped at phase 0 or π the layers were all exactly halfway between the two holes in the neighboring layers and the system formed a Body Centered Tetragonal (BCT) crystal. These BCT structures were even more unstable since the particles were stacked on the bridge sites (saddle points) between two holes in the neighboring layers.

We analysed the structures using the Q_5 and Q_6 bond correlation orientational order parameters to distinguish between the different ways close packed planes can be stacked

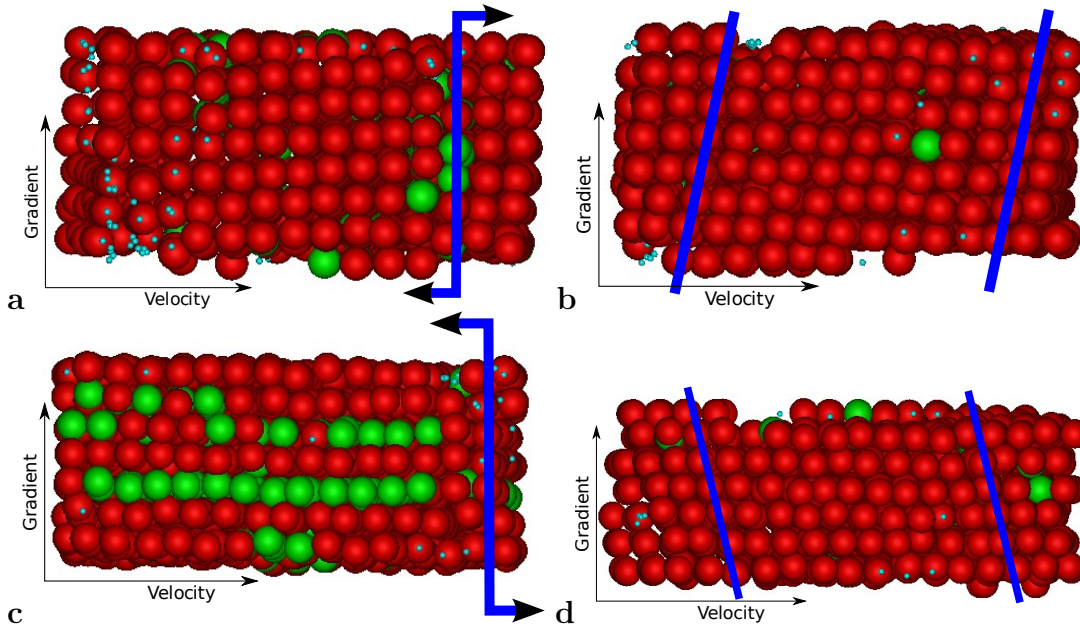
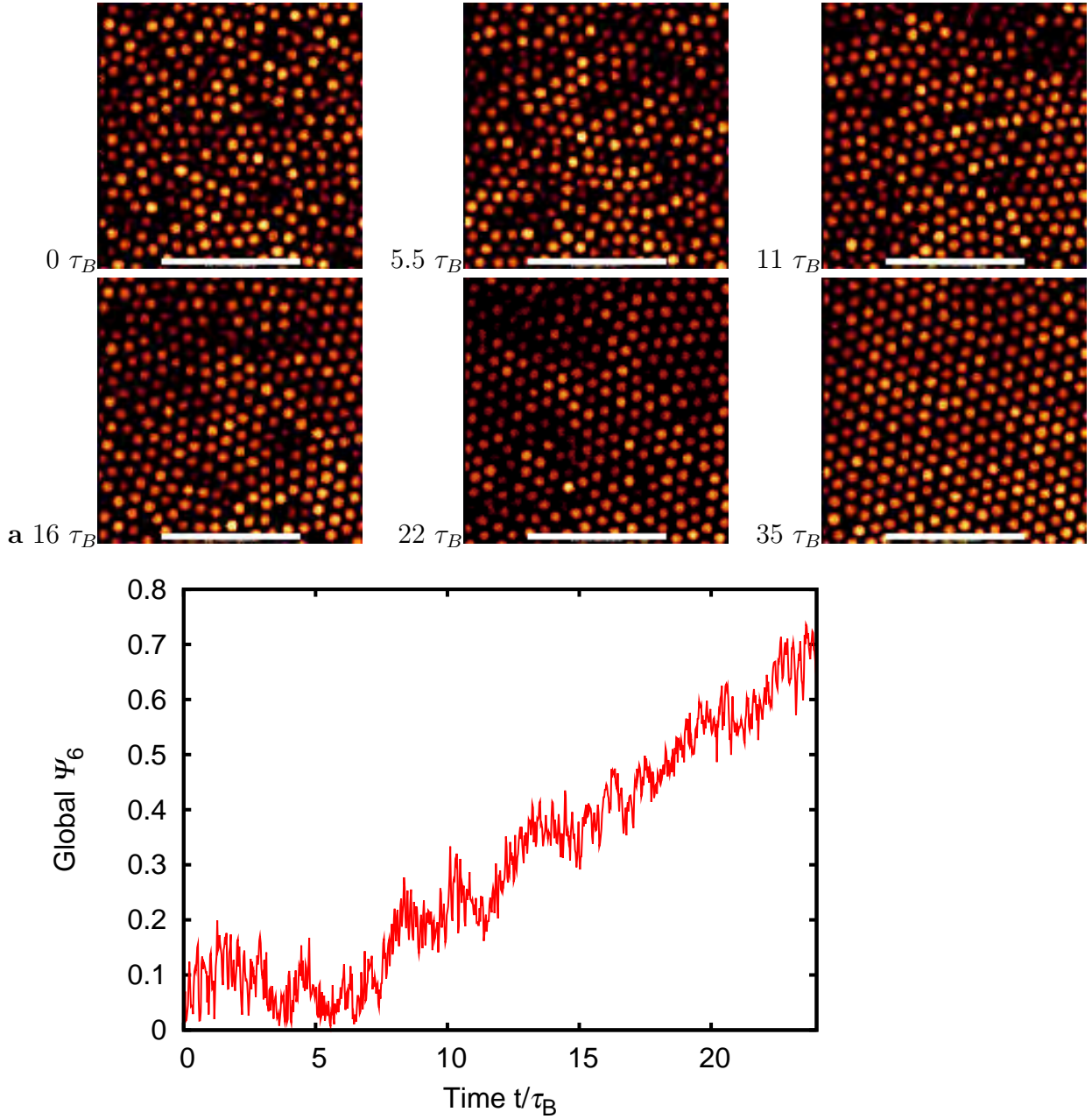


Figure 7.3: Reconstructions of the twin FCC crystal at different phases of the oscillation. The coordinates were obtained from a confocal scan taken immediately after cessation of the shear. The crystalline particles (according to Q_6) are drawn large and the fluid particles are drawn small. The HCP stacked particles have been colored green. The lines indicate the average stacking direction. **a)** A twin FCC crystal at phase 0. **b)** at phase $\pi/2$. **c)** at phase π **d)** at phase $3\pi/4$

and colored the FCC and HCP particles red and green, the fluid particles are depicted as blue spheres of one tenth of the particle diameter. The structure at the extrema in Fig. 7.3b and d was as observed before [129, 130] FCC stacked whereas the structure in between the extrema Fig. 7.3a and c was bridge site stacked i.e. BCT-like. Our order parameters do not distinguish between this bridge site stacked BCT crystal and FCC stacking. In Fig. 7.3c the bridge site stacked structure had already fallen back to a random stacked structure. This Martensitic transition occurred before the crystal melted (this is the same transition as the one that takes place when the electric field is removed from a electric field stabilized colloidal BCT crystal [3]).

Ackerson [129, 130] and Yan [136] used light scattering to study the twin FCC phase and observed 3 peaks on an equilateral triangle oriented with its mirror axis along the velocity direction. The triangle changed orientation during the movement from one extremum to the other. These three peaks are only visible for nearly perfect FCC stacking. The reciprocal lattice of FCC is BCC and the Ewald sphere intersects (or passes very near) three of the corners of the reciprocal lattice producing three maxima. When the stacking is inverted at the other extremum the triangle of scattering the FCC unit cell and the maxima are mirrored. Contrary to Ackerson we often observe a fluid in coexistence with a twin FCC crystal. It is likely that Ackerson never performed experiments at volume fractions low enough to observe coexistence. At a volume fraction of 0.49 or higher the entire sample was filled with twin FCC crystal.



b

Figure 7.4: a) Confocal images of the zero velocity plane of the sample during shear. The volume fraction $\eta = 0.47 \pm 0.01$ the shear amplitude $\gamma_{\max} = 0.36$, and the frequency is $4 \tau_B^{-1}$. The numbers indicate at which time the image was taken. The shear was started at $t = 0$. The scale bars are $20 \mu\text{m}$. b) The global Ψ_6 order parameter as function of time. The steps are caused by groups of particles drifting in and out of focus.

To investigate the nucleation mechanism of the twin FCC phase in more detail we took images of the zero velocity plane during the nucleation. In Fig. 7.4a we show a selection of these images. The shear is started at $t = 0 \tau_B$ and has an amplitude of 0.36 and a frequency of $4 \tau_B^{-1}$. At $t = 0 \tau_B$ the system is fluid at equilibrium with a volume fraction $\eta = 0.47$. In Fig. 7.4b the global order is plotted as function of time. During the first $7 \tau_B$ the order fluctuates around zero until a critical nucleus is formed (outside of our field of view) and the system starts to order. The large fluctuations are caused by layers drifting in and out of focus. We adjusted the position of the focal plane after $25 \tau_B$ to keep a single layer in view. The crystalline order reached a plateau value of $\Psi_6 = 0.65$ after $35 \tau_B$.

Wu et al. [122] observed a continuous increase in crystalline order that took place throughout the sample at the same time. They performed experiments in steady shear at higher volume fractions. We observed patches of high local order mixed with regions of low order. We also observed an induction time that was not observed by Wu et al.. Both the induction time and the formation of nuclei indicate that the transition from fluid to twin FCC phase proceeds via normal nucleation and growth.

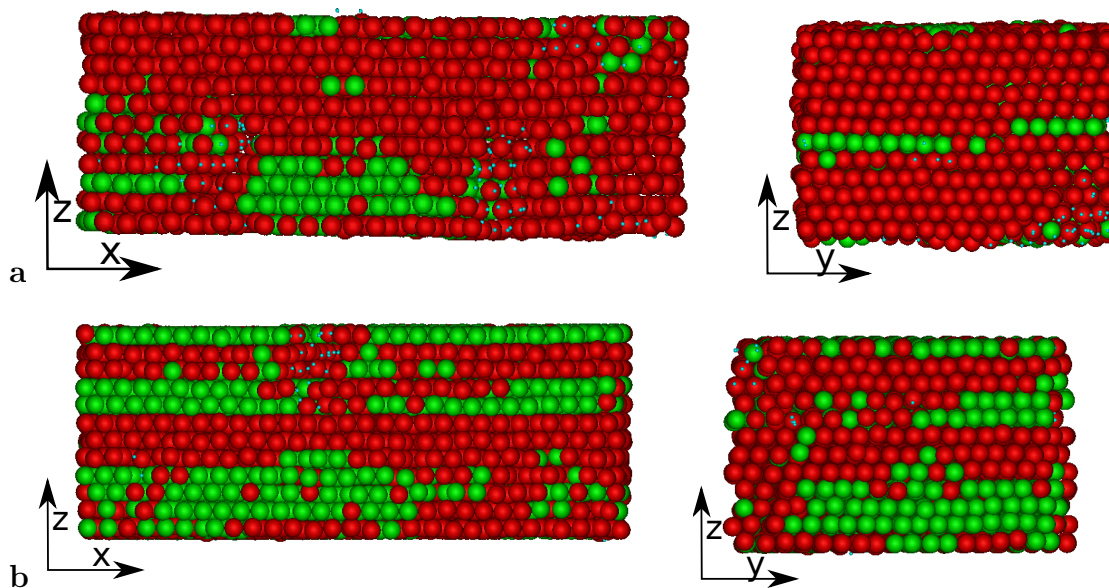


Figure 7.5: *Reconstruction of the sliding layer crystal. The coordinates were obtained from a confocal scan taken immediately after cessation of the shear. The fluid particles (determined using Q_6) are colored blue, the FCC stacked particles (determined using Q_5) are colored red and the HCP stacked particles are colored green. The frequency is $55 \tau_B^{-1}$, the volume fraction is $\eta = 0.49$. **a)** Left the velocity, gradient and right the vorticity, gradient plane of a sample after a strain amplitude of $\gamma_{\max} = 0.6$ and a frequency $54 \tau_B^{-1}$. **b)** Left the velocity, gradient and right the vorticity, gradient plane of a sample after a strain amplitude of $\gamma_{\max} = 0.9$ and a frequency $73 \tau_B^{-1}$.*

At higher strain amplitude the structure changed to a sliding layer phase. We show a configuration at volume fraction $\eta = 0.49$ after cessation of the shear in Fig. 7.5. The

close packed lines of the hexagonal layers were oriented along the velocity direction and slide over each other. The layers become flatter for higher amplitude and frequency. The stacking of the layers continually changed during the shear and was random after cessation of the shear. We did not observe a strong zig-zag motion as was observed by Ackerson and for steady shear at higher densities by Derks et al. [140]. For intermediate strain amplitudes the sliding layer structure was often mixed with the twin FCC structure and regions of both phases were observed separated by grain boundaries.

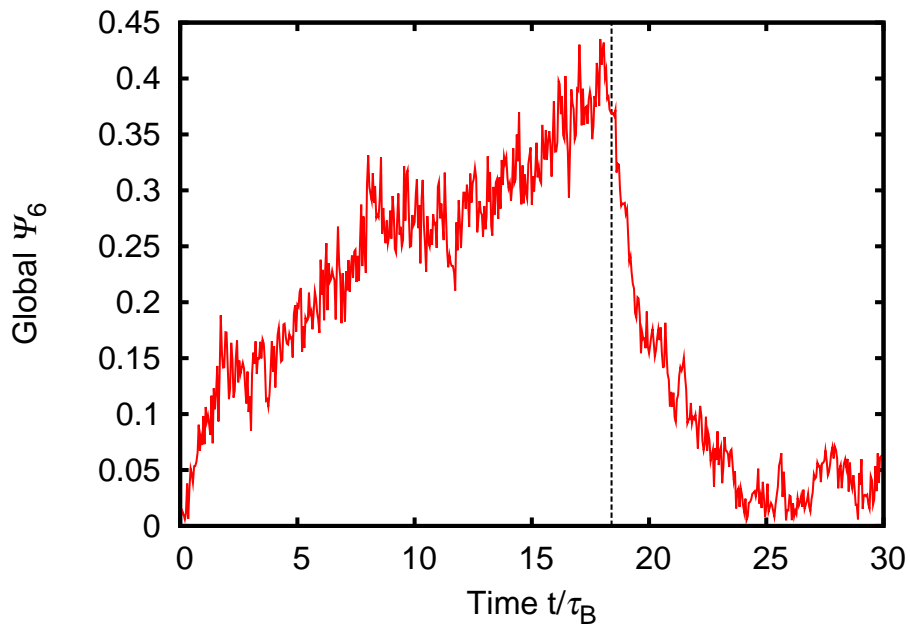
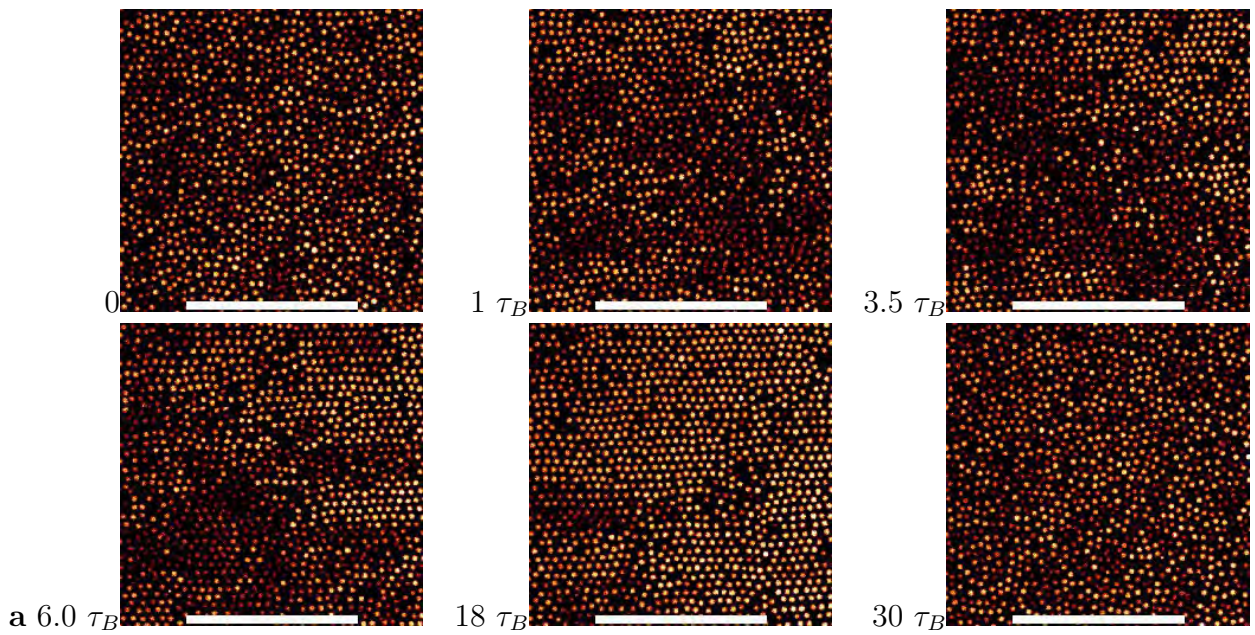
After formation of the sliding layer phase many grain boundaries and line defects were present as well as point defects in the form of missing particles. During the shear the line defects and grain boundaries moved rapidly and annealed out at much higher rates than in an unsheared crystal. Always a few point defects in the form of vacancies remained in the crystal. These vacancies moved one lattice position every couple of oscillations whereas we nearly never saw vacancies move in unsheared crystals. This enhanced defect mobility contributes to the increased quality of the crystals under shear. This was also mentioned by Derks et al. [140] for a sample under steady shear.

In light scattering experiments the sliding layer phase can be recognised by six maxima on a hexagon of which four are brighter than the other two. The hexagon is oriented with the two weaker maxima on the vorticity axis. We were unable to reproduce such a scattering pattern. We could not obtain three dimensional coordinates of the particles during shear. The layers quickly rearrange into the holes of the neighboring layers forming a random stacked structure when the shear was stopped. The resulting scattering pattern had six equally bright spots.

The walls of the sample had strong influence on the structure and the dynamics of the formation of both the twin FCC and the sliding layer phase. We noticed that the particles were stuck to the glass of our sample cell. They could, however, still roll or move over the wall. Despite the stuck particle both phases often nucleated at the wall. These particles formed a seed for nucleation when they formed an ordered structure and hindered nucleation if they did not. Once a crystal had been formed and the particles on the wall had ordered in accordance with this crystal the order on the wall was maintained for long times even after the crystal had melted. These ordered layers on the wall determined the orientation of the crystals that nucleated on the wall in later experiments.

7.3.2 String phase and tilted layer phase

At low volume fraction and a strain amplitude of $\gamma_{\max} = 1.7$ we observed a string phase. The string phase melted so quickly after the cessation of the shear that we were not able to obtain three dimensional coordinates. To investigate the dynamics of the nucleation we took confocal scans of the nucleation in the zero velocity plane. In Fig. 7.6 we show a series of images of a sample with volume fraction $\eta = 0.47 \pm 0.01$. Without shear this sample was completely fluid with only one layer with hexagonal order at both glass walls. When this sample was sheared with shear amplitude $\gamma_{\max} = 1.7$ and a frequency of $f = 6/\tau_B$ the crystal started to grow from the walls of the sample. The images shown were taken 20 particle diameters from the glass wall. After 20 oscillations at $t = 5\tau_B$ small hexagonal patches were visible. These hexagonal patches grew while they improve their alignment with the flow direction.



b

Figure 7.6: **a)** Confocal images taken of the zero velocity plane of the sample during shear. The volume fraction $\eta = 0.47 \pm 0.01$ the shear amplitude $\gamma_{\max} = 1.7$ and the frequency is $3 \tau_B^{-1}$. The numbers indicate the time in Brownian units. The shear was started at $t = 0 \tau_B$ and stopped at $t = 18 \tau_B$. The scale bars are $50 \mu\text{m}$ long. **b)** The global Ψ_6 order parameter as a function of time for the images shown in **a**. The vertical dashed line indicates when the shear was stopped.

In Fig. 7.6b the global Ψ_6 order parameter is plotted as function of time. When the shear was started the hexagonal order immediately started to develop. The order increased slowly over time as the crystal grew from the walls into the sample. The large fluctuations were caused by layers of particles drifting in and out of focus. Although by

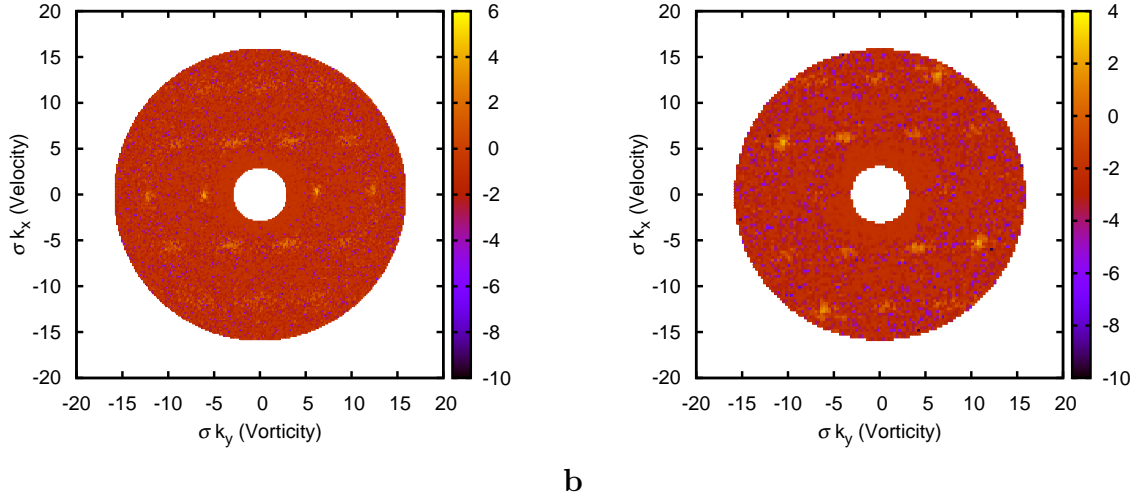


Figure 7.7: **a)** The scattering pattern $\log(S(\mathbf{k}))$ of the string phase calculated from 2d coordinates. The sample was sheared for 110 oscillations at volume fraction $\eta = 0.47 \pm 0.01$, $\gamma_{\max} = 1.7$ and $f = 3\tau_B^{-1}$. **b)** The scattering pattern $\log(S(\mathbf{k}))$ of the tilted layer phase calculated from the 3d coordinates. The sample was sheared for 400 oscillation at volume fraction $\eta = 0.50 \pm 0.01$, $\gamma_{\max} = 0.65$ and $f = 62\tau_B^{-1}$.

eye the layer appeared very regular the low value of Ψ_6 indicated that the layer was not nicely hexagonally ordered. When we took the Fourier transform of the two dimensional data we observed four stripes and two weak peaks in Fig. 7.7a. This is very similar to the scattering patterns observed by Ackerson and Paulin [130, 137]. This means that this is the string phase observed here has the same structure as the string phase observed in the scattering experiments. The string phases observed by Delhommelle in simulations [138] had very similar structure to what we observed.

At frequencies of $f = 14\tau_B^{-1}$ and higher we observed a phase that had some characteristics of the sliding layer phase and some of the string phase. This phase consisted of close packed lines or strings of particles in the velocity direction as can be seen in Fig. 7.8a. To analyse the three dimensional structure we obtained the coordinates after cessation of the shear. In Fig. 7.8b it can be seen that the strings of particles formed hexagonal layers at an angle with the velocity vorticity plane and that they are ABC stacked, therefore we dubbed it the tilted layer phase. This phase occurred solely when the system did not nucleate from the walls. We sometimes observed this tilted layer phase turn into a sliding layer phase in time. The scattering pattern of the tilted layer phase is plotted in Fig. 7.7b. When we compare this scattering pattern with the patterns of Paulin et al. [137] we notice that they observed a very similar scattering pattern. They, however, mistakenly identified this scattering pattern with a sliding layer phase. Neither the tilted layer phase nor the string phase had good long range order. Some higher order maxima were visible in the scattering patterns but they were not as bright as the higher order spots of the twin FCC and the sliding layer structures.

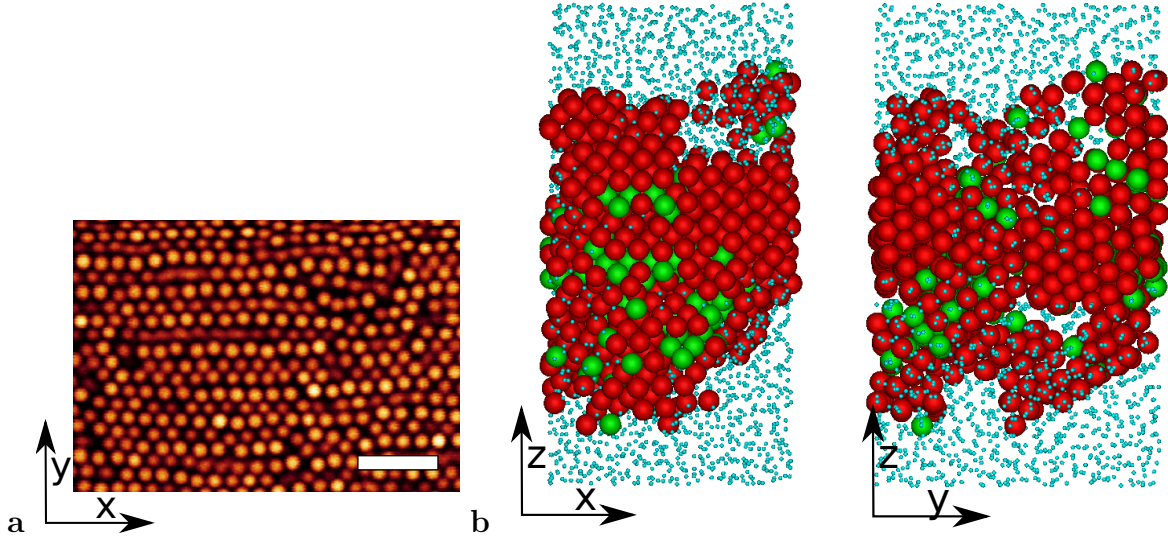


Figure 7.8: a) A confocal image of the tilted layer phase at volume fraction $\eta = 0.50 \pm 0.01$, frequency $f = 62\tau_B^{-1}$ and shear amplitude $\gamma_{\max} = 0.65$. The image was taken in the middle of the gap between the plates. The scalebar is $10 \mu\text{m}$. b) A three dimensional reconstruction of the tilted layer phase. The fluid particles are drawn at one tenth of their actual size.

7.3.3 Non equilibrium phase diagram

We are aware of the fact that the structures, which were observed during shear, are out of equilibrium. Therefore, it is not clear whether a description based on thermodynamic equilibrium (like the existence of a phase diagram) is appropriate. Lacking theory on this we simply apply our knowledge from equilibrium systems to construct an experimental phase diagram.

In Fig. 7.9 the non equilibrium phase diagram for a volume fraction $\eta = 0.49 \pm 0.01$ with the string phases observed at $\eta = 0.46 \pm 0.01$ is shown. This phase diagram was constructed by performing 200 oscillations after which the shear was stopped and the final configuration determined. For low strain amplitude (below 0.1) the system remained amorphous or fluid. At higher strain amplitude the twin FCC phase formed. When the strain was increased further the twin FCC phase changed into a sliding layer phase. Often a mixture of both phases was observed. At higher strain amplitude the structure became fluid again. When the frequency was increased the amplitude range where the crystal existed narrowed.

In Ref. [130], Ackerson determined a phase diagram for fixed frequency which is very similar to the phase diagram shown here. At a volume fraction of $\eta = 0.47$ Ackerson observed the formation of a twin FCC crystal at strain amplitude $\gamma_{\max} = 0.5$ (in our definition of γ_{\max}) which is very similar to our observations. Ackerson observed a mixture of twin FCC structure and the sliding layer structure between $\gamma_{\max} = 0.9$ and $\gamma_{\max} = 1.5$ which again corresponds very well with our phase diagram. We observed the string phase at lower strain amplitude than Ackerson. It is possible that this string phase turns into a sliding layer structure at higher volume fractions.

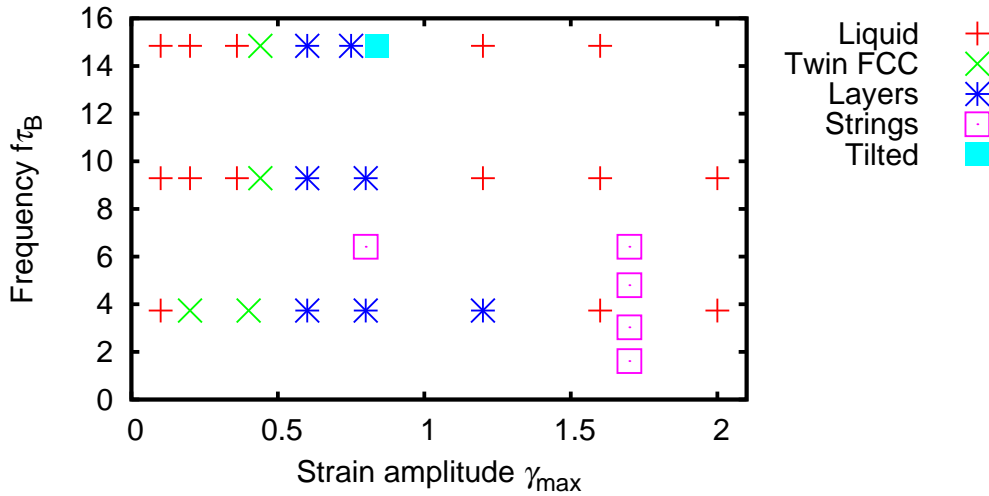


Figure 7.9: The non equilibrium phase diagram for a volume fraction $\eta = 0.49 \pm 0.01$. The string phases were observed at a lower volume fraction $\eta = 0.47 \pm 0.01$. All phases were observed after 200 oscillations.

7.4 Conclusions

We have confirmed that a twin FCC, a sliding layer and a string phase can be formed by applying oscillatory shear to an equilibrium bulk liquid. We observed the formation of these structures in real space and find excellent agreement with the structures analyzed by Ackerson [130] through scattering experiments. Contrary to Ackerson we observed coexistence between fluid and twin FCC phases as well as between fluid and sliding layer phases indicating that these are first order transitions between the ordered phases and the liquid. The transition from twin FCC to sliding layers seems to go through small islands of one phase appearing inside the other phase. However, it is difficult to exclude history and wall effects so further research is needed to elucidate the nature of this transition.

Additionally, we observed a tilted layer phase which was most likely observed in scattering experiments on soft particles but not recognised. This phase does not have a hexagonal layer in the velocity vorticity plane instead there are close packed rows of particles alternating in height visible in the velocity vorticity plane.

We showed that the formation of all the observed phases occurs through nucleation and growth. This is clearly distinct from the high volume fraction regime described by Wu et al. [122]. The melting of the phases all starts at the surfaces and the defects and proceeds from there. Both the string phase and the tilted layer phase contained very little long range order compared to the twin FCC and the sliding layer phase. No third or higher order Bragg spots were visible in the scattering and the global two dimensional bond order parameter was never higher than 0.4 for the string phase. Both the string phase and the tilted layer phase were very unstable without shear and melted within 1-3 τ_B when the shear was stopped.

7.5 Acknowledgements

We would like to acknowledge T. Besseling for performing most of the experiments described in this chapter.

Depletion forces between spherical particles with a rough surface

Interactions between colloids can be modified by the addition of polymers to the suspension. Polymers cause effective attractions between the colloidal particles: the depletion interaction. If the attraction range and strength are sufficient this attraction results in a gas liquid coexistence making the phase diagram very similar to that of molecular systems. The polymer concentration plays the role of inverse temperature, a high polymer concentration corresponds to a strong attraction and low temperature, whereas a low polymer concentration corresponds to weak attraction and high temperature. Zhau et al. and Badaire et al. have used surface roughness of platelets and cylinders to reduce the effective overlap of the polymer excluded volume. Here we investigate whether tuning the surface roughness to reduce depletion forces is also viable for spherical particles. We generate a rough surface by attaching small colloidal particles to a big spherical colloid. This is inspired by several experimental procedures with which such surfaces can be realised. We calculate the pair interaction between smooth and rough colloids (in the dilute polymer regime). We find that when the polymer is smaller than the small colloidal particles the attraction can be reduced significantly. The exact numbers depend on the details of the system but for particles that were recently synthesized by Van Kats and Kraft we expect that a reduction of one order of magnitude should be easily obtained. We calculate the pair potential for newly synthesised systems of polystyrene dumbbells consisting of one smooth and one rough sphere and show that in principle it is possible to strongly reduce the attraction between the rough spheres which makes these dumbbells a model surfactant.

8.1 Introduction

Asakura and Oosawa [141] and later, independently, Vrij [142] showed that colloids feel an attractive force when nonadsorbing polymers are added to a colloidal dispersion. Every colloid is surrounded by a zone, where the centers of mass of the polymers are excluded, the so-called depletion zone, Fig 8.1. This attractive force arises from the overlap of these depletion zones, when they overlap the volume available to the polymers increases and gives rise to a gain in entropy and with that an effective attraction between the colloids. The range of this attraction is given by the size of the polymers and the strength of the attraction is determined by the density of the polymers. Another, identical, method of understanding this attraction is through an osmotic pressure imbalance. The polymers exert pressure on the colloids where they can reach their surface. The pressure imbalance is caused by the absence of polymers pushing on the colloids from the overlapping depleted zones between two colloids.

In what is now called the Asakura Oosawa (AO) model the polymers are assumed not to interact with other polymers and to interact as hard spheres with the colloids. This is a valid assumption when the polymers are in a good solvent and the volume fraction of polymers is low i.e. $\eta_{\text{polymers}} \ll 1.0$ so that the polymers remain in the dilute regime. When the volume fraction is in the semi-dilute regime correlations between the polymers will start to play a role. In this regime the AO model will overestimate the range and the depth of the attraction [143].

Colloid-polymer mixtures are widely used as a model system to study the phase behaviour of attractive systems. The ability to tune the attraction between particles by changing the polymer concentration has led to a range of new research. Colloid-polymer mixtures have produced: better understanding of the phase behaviour of liquids [144], the first real space studies of capillary waves [145] and a greater understanding of meta stable phases [146]. The phase diagram has been extensively studied with experiments [147], simulations [148, 149] and theory [144]. Many different depletants have been used, the effects of charge, size, solubility, stiffness and the adsorption properties of the depleting particles have been investigated [150], for a review see [151, 152].

The surface of the container walls has been engineered to enhance or reduce the overlap volume [153] but only recently it has been realized that the surface of the colloidal particles can also be modified. By modifying the surface of the colloids the overlap volume, and with that the interactions, can be engineered. By making the surface rough the attractions can be reduced whereas a flat surfaces enhance the attractions. When only part of the colloid surface is modified, attractive or repulsive patches can be made. Zhai et al. [154] and Badaire et al. [155] have shown that the depletion interaction between platelets and cylinders can be tuned by modifying the surface roughness. The cylinders used by Badaire had a flat top and a flat bottom but sides of which the roughness could be tuned. They show that particles with rough sides aggregated top to bottom and formed columnar aggregates while particles with smooth sides also aggregated side to side. They conclude that when the root mean square amplitude of the roughness Δ_{RMS} is much larger than the diameter of the polymer σ_p the depletion attraction is effectively reduced.

It is expected, from geometric considerations, that the surface or line contacts between cylinders are much more sensitive to surface roughness than the contacts between spheres

since the contact area between spheres is so much smaller. We investigate whether it is feasible to tune the depletion interaction between spherical colloids by modifying the surface roughness. We determine the parameter range for which the depletion attraction between rough spheres is reduced in such extent that it can for instance prevent significant phase separation of rough particles for parameters for which smooth particles phase separate. The parameters that we investigate are polymer concentration, polymer size, surface coverage of small particles on the large particle, size of the small particle and size ratio of rough and smooth particles. In the last section, we investigate the effect of charge stabilization on the effectiveness of the roughness.

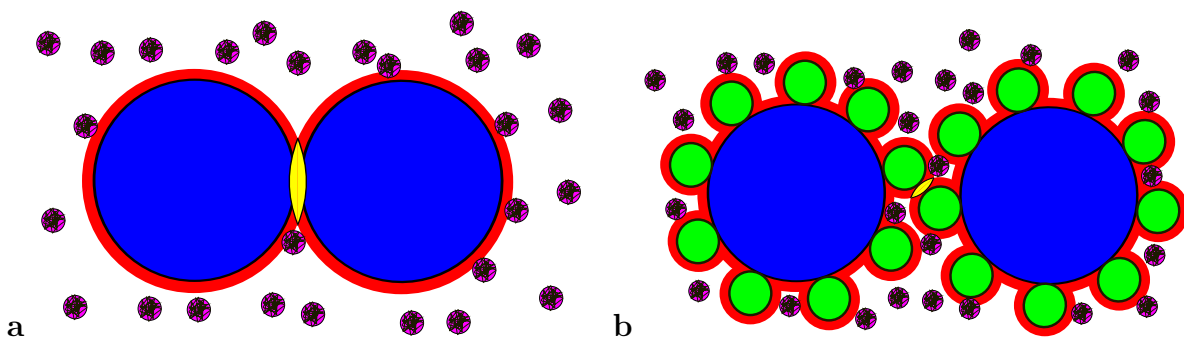


Figure 8.1: The depletion zones (red) for the polymers (purple) of two colloids (blue). The overlap of the depleted zones is yellow. **a)** For two smooth spheres. **b)** For two spheres coated with small spheres (green).

To calculate the interaction potential between rough particles we first need to generate particles with a rough surface. To create rough particles we perform MC simulations with a Yukawa interaction. We place a single positively charged large sphere in the center of our box and many negatively charged small spheres around it. We run this simulation and increase the charge of the large sphere until all the small spheres have aggregated on the large sphere. We then take the end configuration of this simulation as a model for a rough particle. There have been several experimental studies in which particles have been made with such a method [156].

In many cases colloidal dispersions are stabilized against aggregation by Van der Waals forces. Silica colloids are often stabilized by charge whereas PMMA and polystyrene are often stabilized with a steric layer. The thickness of the stabilization layer determines the distance of closest approach between the particles. The polymers are often not hindered by charge stabilization since they are not charged, however, they are hindered by the dense steric layer. We find that in the case of charge stabilized spheres the polymer size is limited by the thickness of this stabilization layer on the colloids on the one hand and the size of the rough particles on the other hand. In case of sterically stabilized spheres it is not entirely clear what limits the size of the polymers.

The concentration should then be chosen such that the smooth particles feel an attraction of a few $k_B T$ while the attraction between rough and smooth particles is still less than one $k_B T$. In this way the smooth particles will cluster while the rough particles will not.

8.2 Model and effective interactions

We model the colloidal particles as hard spheres with diameter σ_c at positions \mathbf{R}_i coated with small hard spheres on the colloidal surface. We consider N_c coated particles with orientations $\hat{\omega}_i$ and N_p polymers with diameter σ_p at positions \mathbf{r}_j in a macroscopic volume V at temperature T . The polymer diameter $\sigma_p = 2R_g$ is taken to be twice the radius of gyration R_g . The colloidal particles are described by a pairwise colloid-colloid interaction Hamiltonian $H_{cc} = \sum_{i < j}^{N_c} \phi_{cc}(\mathbf{R}_{ij}, \hat{\omega}_i, \hat{\omega}_j)$, a pairwise colloid-polymer Hamiltonian $H_{cp} = \sum_{i=1}^{N_c} \sum_{j=1}^{N_p} \phi_{cp}(\mathbf{R}_i - \mathbf{r}_j, \hat{\omega}_i)$, and a polymer-polymer Hamiltonian $H_{pp} \equiv 0$ as the polymers are assumed to be ideal. Here we introduced the colloid-colloid pair potential ϕ_{cc} and the colloid-polymer pair potential ϕ_{cp} given by

$$\beta\phi_{cc}(\mathbf{R}_{ij}, \hat{\omega}_i, \hat{\omega}_j) = \begin{cases} \infty & \text{for } \xi(\mathbf{R}_{ij}, \hat{\omega}_i, \hat{\omega}_j) < 0 \\ 0 & \text{otherwise} \end{cases}$$

$$\beta\phi_{cp}(\mathbf{R}_i - \mathbf{r}_j, \hat{\omega}_i) = \begin{cases} \infty & \text{for } \xi(\mathbf{R}_i - \mathbf{r}_j, \hat{\omega}_i) < 0 \\ 0 & \text{otherwise} \end{cases}$$

where $\beta = (k_B T)^{-1}$ with k_B the Boltzmann constant, and where $\mathbf{R}_{ij} = \mathbf{R}_i - \mathbf{R}_j$, $\xi(\mathbf{R}_{ij}, \hat{\omega}_i, \hat{\omega}_j)$ denotes the surface-to-surface distance between two coated particles, and $\xi(\mathbf{R}_i - \mathbf{r}_j, \hat{\omega}_i)$ is the surface-to-surface distance between a coated particle and a polymer coil. The total interaction Hamiltonian of the system of interest reads $H = H_{cc} + H_{cp}$. The kinetic energy of the polymers and the colloids is not considered here explicitly, as it is trivially accounted for in the classical partition sums to be evaluated below.

We map the binary mixture of coated particles and ideal polymers with interaction Hamiltonian H onto an effective one-component system with Hamiltonian H^{eff} by integrating out the degrees of freedom of the polymer coils. Our derivation follows closely those of Refs. [157–162].

We consider the system in the (N_c, V, z_p, T) ensemble, in which the fugacity $z_p = \Lambda_p^{-3} \exp(\beta\mu_p)$ of the polymer coils is fixed, with Λ_ν the thermal wavelength of species $\nu = c, p$, and with μ_p the chemical potential of the polymers. The thermodynamic potential $F(N_c, V, z_p, T)$ of this ensemble can be written as

$$\begin{aligned} \exp[-\beta F] &= \sum_{N_p=0}^{\infty} \frac{z_p^{N_p}}{N_c! \Lambda_c^{3N_c} N_p!} \text{Tr}_c \text{Tr}_p \exp[-\beta H] \\ &= \frac{1}{N_c! \Lambda_c^{3N_c}} \text{Tr}_c \exp[-\beta H^{\text{eff}}], \end{aligned} \quad (8.1)$$

where the trace Tr_c is short for the volume integral $\int_V d\mathbf{R}^{N_c} \int_\Omega d\hat{\omega}^{N_c}$ over the coordinates and orientations of the coated particles, and similarly $\text{Tr}_p = \int_V d\mathbf{r}^{N_p}$. The effective Hamiltonian of the coated particles is written as

$$H^{\text{eff}} = H_{cc} - z_p V_f, \quad (8.2)$$

where $z_p V_f = z_p V_f(\{\mathbf{R}\}, \{\hat{\omega}\})$ is the negative of the grand potential of the fluid of ideal polymer coils in the static configuration of N_c coated colloids with coordinates $\{\mathbf{R}\}$ and

orientations $\{\hat{\omega}\}$. Here $V_f(\{\mathbf{R}\}, \{\hat{\omega}\})$ is the free volume of the polymers in the configuration of the colloids. Because of the ideal character of the polymer-polymer interactions it can be written explicitly as

$$V_f = \int_V d\mathbf{r} \exp\left[-\sum_{i=1}^{N_c} \beta\phi_{cp}(\mathbf{R}_i - \mathbf{r}, \hat{\omega}_i)\right]. \quad (8.3)$$

Non-vanishing contributions to V_f stem from those positions \mathbf{r} that are outside any of the N_c depletion shells. The shape of the free volume is highly irregular and non-connected. We decompose V_f , formally, into zero-colloid, one-colloid, two-colloid contributions, etc., by expanding it in terms of the colloid-polymer Mayer-function $f(\mathbf{R}_i - \mathbf{r}, \hat{\omega})$, which for the present model equals -1 for $\xi(\mathbf{R}_i - \mathbf{r}, \hat{\omega}) < 0$, and 0 otherwise. One finds

$$\begin{aligned} V_f &= \int_V d\mathbf{r} \prod_{i=1}^{N_c} (1 + f(\mathbf{R}_i - \mathbf{r}, \hat{\omega})) \\ &= V + \sum_{i=1}^{N_c} V_f^{(1)}(\mathbf{R}_i, \hat{\omega}_i) + \sum_{i<j}^{N_c} V_f^{(2)}(\mathbf{R}_i, \mathbf{R}_j, \hat{\omega}_i, \hat{\omega}_j) + \dots \end{aligned} \quad (8.4)$$

For $k \geq 1$, the k -colloid contribution reads

$$V_f^{(k)} = \int_V d\mathbf{r} \prod_{m=1}^k f(\mathbf{R}_{i_m} - \mathbf{r}, \hat{\omega}_{i_m}), \quad (8.5)$$

where only those positions \mathbf{r} give non-vanishing contributions where the depletion layers of (at least) k colloids overlap simultaneously.

We give explicit expressions for $V_f^{(k)}$ for $k = 1$ and 2 for equal-sized colloidal hard spheres with a smooth surface. It follows directly from Eq. (8.4) that the one-body contribution $V_f^{(1)} = -v_1$ with $v_1 = \pi\sigma_{cp}^3/6$ and $\sigma_{cp} = (\sigma_c + \sigma_p)/2$, which can be interpreted as the volume that is excluded for a polymer coil by a single colloid. $V_f^{(2)}(\mathbf{R}_i, \mathbf{R}_j)$ is the lens-shaped overlap volume of two spheres of radius σ_{cp} at separation $R_{ij} = |\mathbf{R}_i - \mathbf{R}_j|$. We note that $-z_p V_f^{(2)}(R_{ij}) \equiv \beta\phi_{AO}(R_{ij})$ is the well-known depletion potential of the AO model [142, 163], which was derived by Asakura and Oosawa [141, 164]. The effective pair potential $\phi_{\text{eff}}(R_{ij}) = \phi_{cc}(R_{ij}) + \phi_{AO}(R_{ij})$ reads

$$\beta\phi_{\text{eff}}(R_{ij}) = \begin{cases} \infty & \text{for } R_{ij} < \sigma_c \\ -\frac{\pi\sigma_p^3 z_p (1+q)^3}{6 q^3} \left[1 - \frac{3R_{ij}}{2(1+q)\sigma_c} + \frac{R_{ij}^3}{2(1+q)^3 \sigma_c^3} \right] & \text{for } \sigma_c < R_{ij} < 2\sigma_{cp} \\ 0 & \text{for } R_{ij} > 2\sigma_{cp} \end{cases}$$

This Asakura-Oosawa pair potential describes an attractive well close to the surface of the colloid, whose depth increases linearly with increasing z_p . The range of the potential is given by σ_p .

Similarly, we define an effective depletion potential for our coated spheres, which depends explicitly on the orientation of the coated spheres.

$$\beta\phi_{\text{eff}}(\mathbf{R}_{ij}, \hat{\omega}_i, \hat{\omega}_j) = \beta\phi_{cc}(\mathbf{R}_{ij}, \hat{\omega}_i, \hat{\omega}_j) - z_p \int_V d\mathbf{r} f(\mathbf{R}_i - \mathbf{r}, \hat{\omega}_i) f(\mathbf{R}_j - \mathbf{r}, \hat{\omega}_j) \quad (8.6)$$

The three- and more-body contributions $V_f^{(k)}$ with $k \leq 3$ will be zero when the radius of gyration of the polymer coils is sufficiently small compared to the size of the colloids. The mapping of the full Hamiltonian of the colloid-polymer mixture can then be mapped exactly onto an effective Hamiltonian with only effective pairwise additive interactions, since three colloidal spheres cannot simultaneously overlap with a polymer coil. If the relaxation of the orientation degrees of freedom is much faster than that of the translational degrees of freedom, and the coated particles are sufficiently isotropic, we can perform a further coarse-graining by integrating out the orientational degrees of freedom of the effective interactions. The orientation-averaged effective pair potential reads

$$\beta\phi_{\text{eff}}(R_{ij}) = -\log\left(\frac{1}{16\pi^2} \int_{\Omega} d\hat{\omega}_i \int_{\Omega} d\hat{\omega}_j \exp\left[-\beta\phi_{\text{cc}}(\mathbf{R}_{ij}, \hat{\omega}_i, \hat{\omega}_j) - z_p \int_V d\mathbf{r} f(\mathbf{R}_i - \mathbf{r}, \hat{\omega}_i) f(\mathbf{R}_j - \mathbf{r}, \hat{\omega}_j)\right]\right). \quad (8.7)$$

Since the integrals over the orientations of the particles cannot be solved directly, we perform the orientation average by evaluating the integrand for many different random orientations. We have checked the convergence of our integrations.

In order to generate colloidal particles coated with small particles onto the surface, we perform Monte Carlo simulations of a binary mixture of oppositely charged particles in the NVT ensemble. The particles are assumed to interact with Yukawa interactions and we choose a negative charge on the small particles with diameter σ_{small} and a positive charge on the large particles. The charge of the large spheres was increased until all the small particles were attached onto the surface of the large particles. The structure of the small particles on the surface of the large particles can be tuned by the inverse screening length $\kappa\sigma_c$ in the Yukawa interaction of the particles. For low $\kappa\sigma_c$ the small particles are evenly distributed and very structured while for high $\kappa\sigma_c$ there is much more disorder in the coating of the small spheres. Using $\kappa\sigma_c = 10$, the resulting configurations gave the best match with the coated particles obtained by Van Kats and Kraft as shown in Fig. 8.2.

Once the two particles have been created they are placed next to each other in a cubic simulation box and $1 \cdot 10^5$ random orientations of the two particles are sampled. For the first 1000 non overlapping configuration the pair potential is calculated. If non overlapping configurations were found the particles are moved closer together and again orientations are generated and the potential calculated.

To calculate the free volume we divide the space into cells. To calculate the overlap volume in each cell we first check whether the cell is completely embedded in the overlap volume or falls completely outside the overlap volume. If neither is the case the cell is divided into eight subcells for which we perform the same procedure. This is repeated until the volume of the cell is smaller than $1 \cdot 10^{-5}$, the algorithm then randomly generates ten points to estimate the overlap volume in this cell. The final overlap volume is than the sum of the overlap volume of all cells. We tested the accuracy of this method for two spheres and the difference between the analytic expression and the calculation is less than $1 \cdot 10^{-5}\sigma^3$.

We are interested in the attraction between rough spheres in the presence of smooth spheres. The aim is to have smooth spheres with a significant attraction while the effective

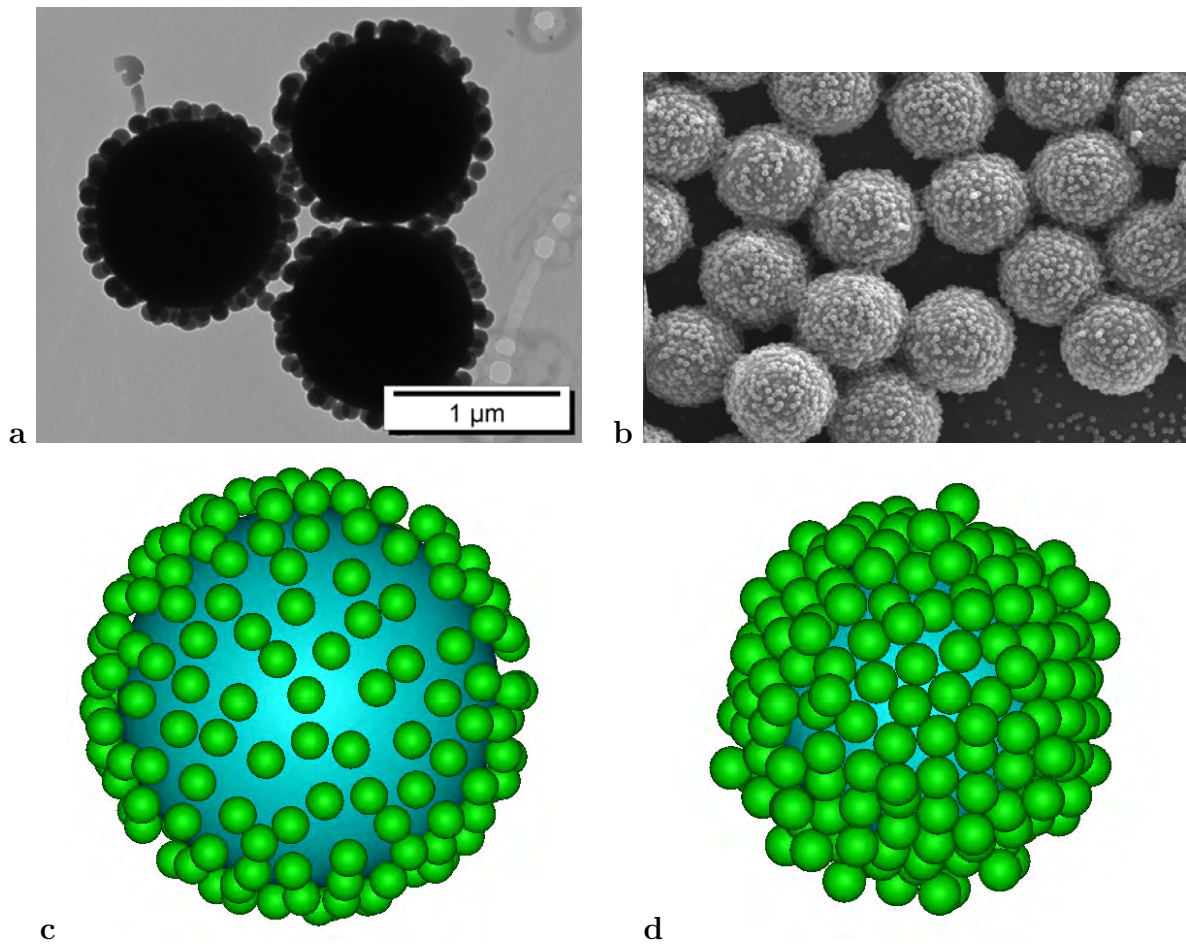
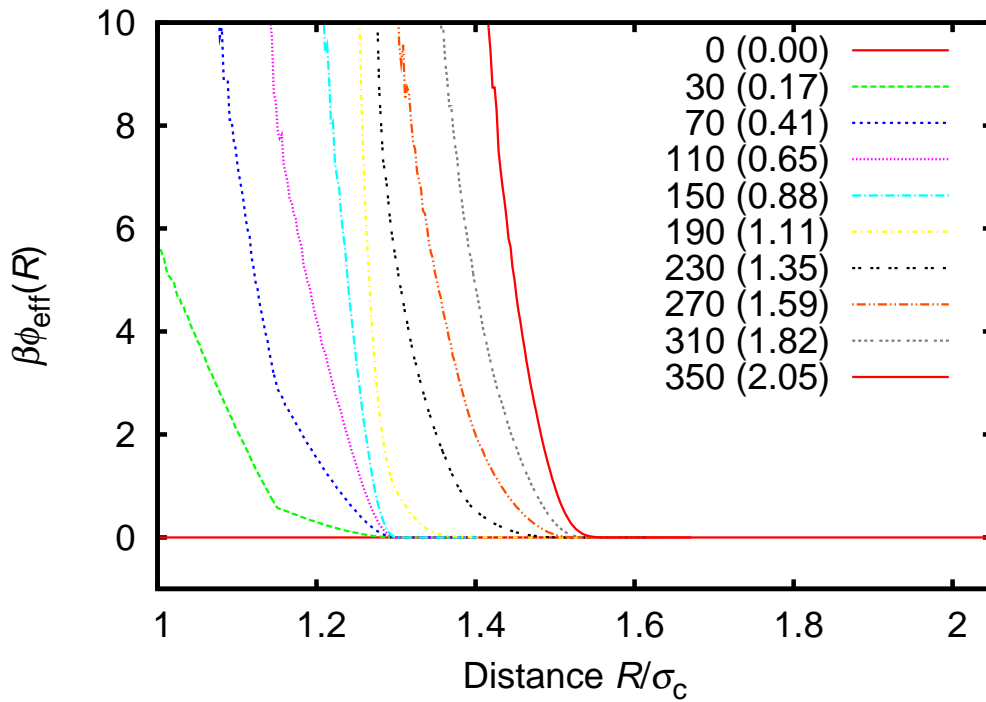


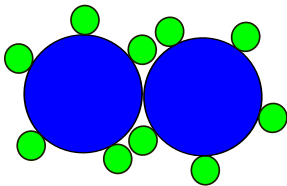
Figure 8.2: a) $1.238 \mu\text{m}$ silica spheres coated with $0.75 \mu\text{m}$ silica spheres made by Van Kats. The large particles were given an opposite charge with a coating of PAH. The small particles were fixed by a final coating step in which a layer of 10 nm TPM is grown on the entire particle. b) Rough polystyrene particles made by Kraft. c and d) Rough spheres generated in MC simulations by aggregation of small spheres on an oppositely charged large particle.

attraction between the rough and smooth spheres is still weak. The parameters that can be tuned in the experiments are: the size ratio between the large particles and the small particles used to tune the roughness, the size ratio between polymer and small particles and the number of small particles on the large particle. We investigate for which parameters the effect of the roughness is largest.

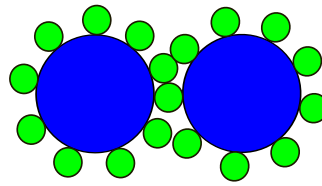
8.3 Results



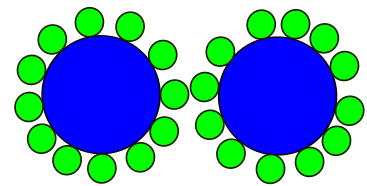
a



b



c



d

Figure 8.3: **a)** The effective pair potential $\beta\phi_{\text{eff}}(R)$ between two spheres with diameter σ_c as a function of center-of-mass distance R and an increasing coverage of small particles with diameter $\sigma_{\text{small}} = 0.15\sigma_c$ in the absence of polymers. The first number in the legend denotes the number of small spheres, the second number the fraction of one complete layer. **b)** Sparsely covered spheres can still touch at a center of mass distance $R = \sigma_c$. **c)** Spheres with half a layer of small particles can approach till $R \approx \sigma_c + \sigma_{\text{small}}$. **d)** Spheres with more than half a layer can approach till $R \approx \sigma_c + 2\sigma_{\text{small}}$.

The effective potential (8.7) between two rough spheres is repulsive when there are

no polymers present because the roughness reduces the number of non-overlapping configurations. To calculate this repulsive potential we calculate the ratio of configurations with and without overlap as a function of distance. In figure 8.3 we show the effective potential between two spheres with diameter σ_c with increasing coverage of small spheres with diameter $0.15\sigma_c$. A low coverage of only 30 particles already produces an effective repulsive potential of more than $5 k_B T$. With approximately 180 particles the particles are fully covered and the particles only have a very limited number of configuration available where the rough surfaces can penetrate. The kink at $1.15 \sigma_c$, visible at a coverage of 10-70 small particles, is caused by configurations where the particles can still come into contact but only with a very limited number of orientations.

To generate the configurations with more than one complete layer of particles the charge of large particle had to be increased till unphysical high values. These configuration can therefore, not be formed by the adsorption of oppositely charged particles. However, large particles covered with multiple layers of small particles can be synthesized by different methods. Therefore, we are also interested in these particles with multiple layers of small particles as a model for particles made by different methods.

8.3.1 Effect of surface coverage

When polymers are added to the system they will gain entropy when the colloids are forced together and an attractive depletion potential will counteract the repulsive potential caused by the loss of rotational degrees of freedom of the colloids. In Fig. 8.4 we plot the effective pair potential for two colloids of radius σ_c covered with small particles of $\sigma_{\text{small}} = 0.15\sigma_c$ and polymers with diameter $0.04 \sigma_c$. The polymers have a fugacity of $z_p \sigma_c^3 = 5000$ which corresponds to a polymer reservoir packing fraction of $\eta_p^r = z_p \sigma_p^3 \pi / 6 = 0.17$ if we take $\pi \sigma_p^3 / 6$ as the volume of a polymer coil. The smooth spheres are attracted with approximately $6 k_B T$. The same structure as without polymers becomes even more visible. For particles with a sparse covering of 20-40 small particles as shown in Fig. 8.3b the potential shows two minima, one at center-of-mass distance $R = \sigma_c$ and one at $R = \sigma_c + \sigma_{\text{small}}$. When the coverage is increased a minimum starts to develop at $R \approx 1.28\sigma_c$ as the first layer of particles starts to become denser. When the first layer of small particles is complete, a second layer starts to form and the minimum moves to $1.5 \sigma_c$. The suppression of the attraction is most effective at 60-80 and 220-260 particles when the outer layer is sparsely populated and not when the outer layer is complete at 180 particles.

The range of the attraction is increased by the rough surface. For a smooth sphere the attraction range is exactly the polymer diameter. The rough spheres have, for sufficiently high polymer fugacity, an attractive range of the polymer diameter plus approximately the diameter of the small particles that are used for the surface roughness. This effect is most pronounced when the outer layer of small particles is incomplete.

8.3.2 Effect of polymer size

The radius of gyration of the polymers has to be smaller than the small particles on the surface otherwise the roughness will be smoothed out by the polymers. To investigate

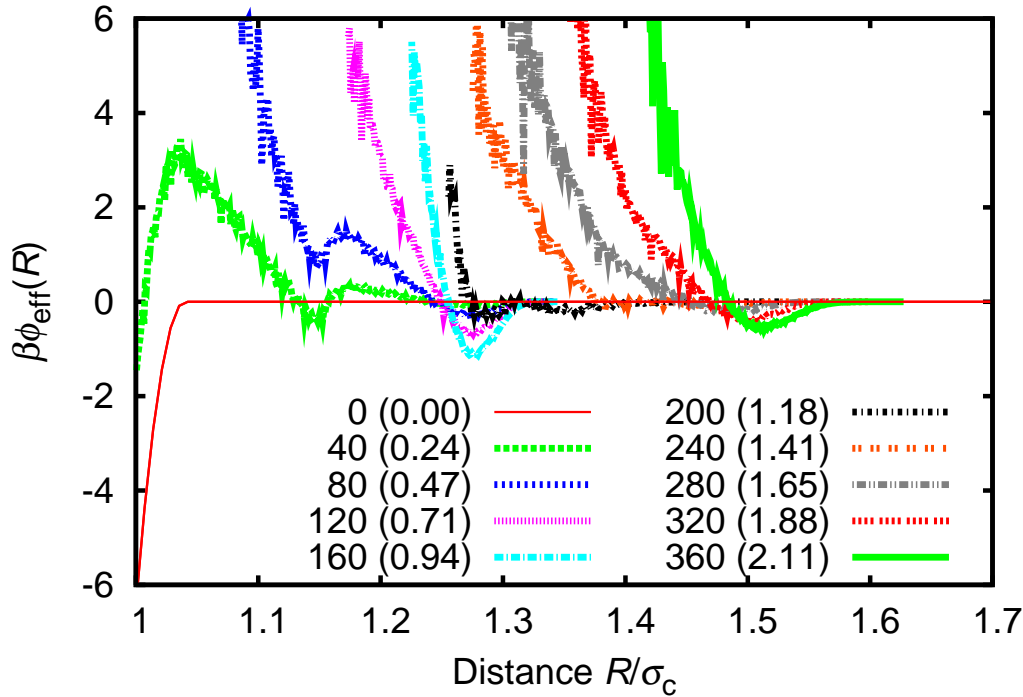


Figure 8.4: The effective pair potential $\beta\phi_{\text{eff}}(R)$ between two spheres with an increasing coverage of small particles. The first number in the legend denotes the number of small spheres the second number the fraction of one complete layer. The bare spheres have a diameter σ_c . The polymer has a diameter of $0.04 \sigma_c$ and a polymer reservoir packing fraction of $\eta_p^r = 0.16$. The small spheres have a diameter of $0.15 \sigma_c$. The attraction between the smooth spheres is $6 k_B T$.

the effect of polymer size quantitatively we change the polymer size while we fix the attraction strength between the smooth spheres at $6 k_B T$. To keep the attraction strength between smooth particles fixed we increased the fugacity of the smaller polymers, however, the actual volume fraction goes down for smaller polymers. For the largest polymers the volume fraction is 0.58 and for the smallest it is 0.04. For high polymer volume fraction such as 0.58 correlations between the polymers can no longer be ignored and our assumption of noninteracting polymers will break down. In Fig. 8.5 we plot the attraction between two spheres covered with 250 small particles of diameter $0.15 \sigma_c$. When the polymer has approximately the same size as the particles used for the roughness, the attraction between rough particles is nearly as strong as between smooth particles, but the range is $\sigma_p + \sigma_{\text{small}}$. When the polymer is made smaller the difference between smooth and rough particles increases. Also the volume fraction of polymer required to obtain a reasonable attraction is much lower for the smaller polymers. We conclude from this graph that smaller depletion agents are more sensitive to particle roughness as they probe a larger part of the roughness and at a larger center of mass distance.

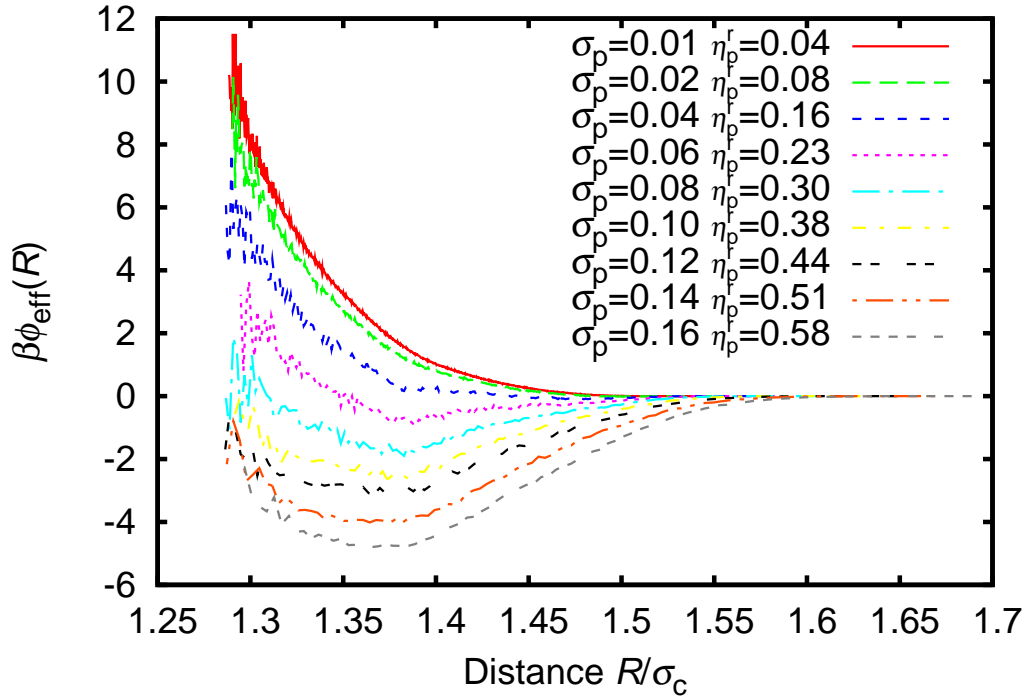


Figure 8.5: The effective pair potential $\beta\phi_{\text{eff}}(R)$ between two rough spheres covered with 250 small spheres of $0.15\sigma_c$. The polymer diameter and reservoir packing fraction $\eta_p^r = z_p\sigma_p^3\pi/6$ are varied as labeled. The polymer reservoir packing fraction is chosen such that the attraction between the smooth colloids is $6k_B T$.

8.3.3 Rough dumbbells

We have also calculated the effective interaction potentials for an experimental system of asymmetric polystyrene dumbbells with a rough side and a smooth side. These particles have recently been made by Nagao et al. [165] but also by Kraft in cooperation with Yoon and Weitz (Harvard University). Kraft made two systems of these asymmetric dumbbell particles: one where the larger sphere was smooth and one where the smaller sphere was smooth. The particles are particularly interesting when the smooth sides attract each other with several $k_B T$, while the attraction between the rough sides remains weak. If this is the case the particles can be seen as model surfactants.

The first system is a system with size ratio 0.72 with large smooth sides and smaller rough sides as can be seen in Fig. 8.6. The large smooth spheres have a diameter of $3.32\mu\text{m}$, the rough spheres have a diameter of approximately $2.4\mu\text{m}$ including the surface, the small spheres that form the rough layer have a diameter of 182nm and the polymers have radii of gyration of 10, 19 and 34nm , corresponding to diameters $\sigma_p = 20, 38, 68\text{nm}$, respectively. In Fig. 8.6 we have plotted the pair potentials between the smooth and rough sides. For all polymer sizes the effect of the roughness is significant. For the largest polymer (diameter of 68nm) the attraction between smooth sides is eight times stronger than between the rough and smooth sides. This should be sufficient to be visible in experiments. The polymer reservoir packing fraction required for this attraction is

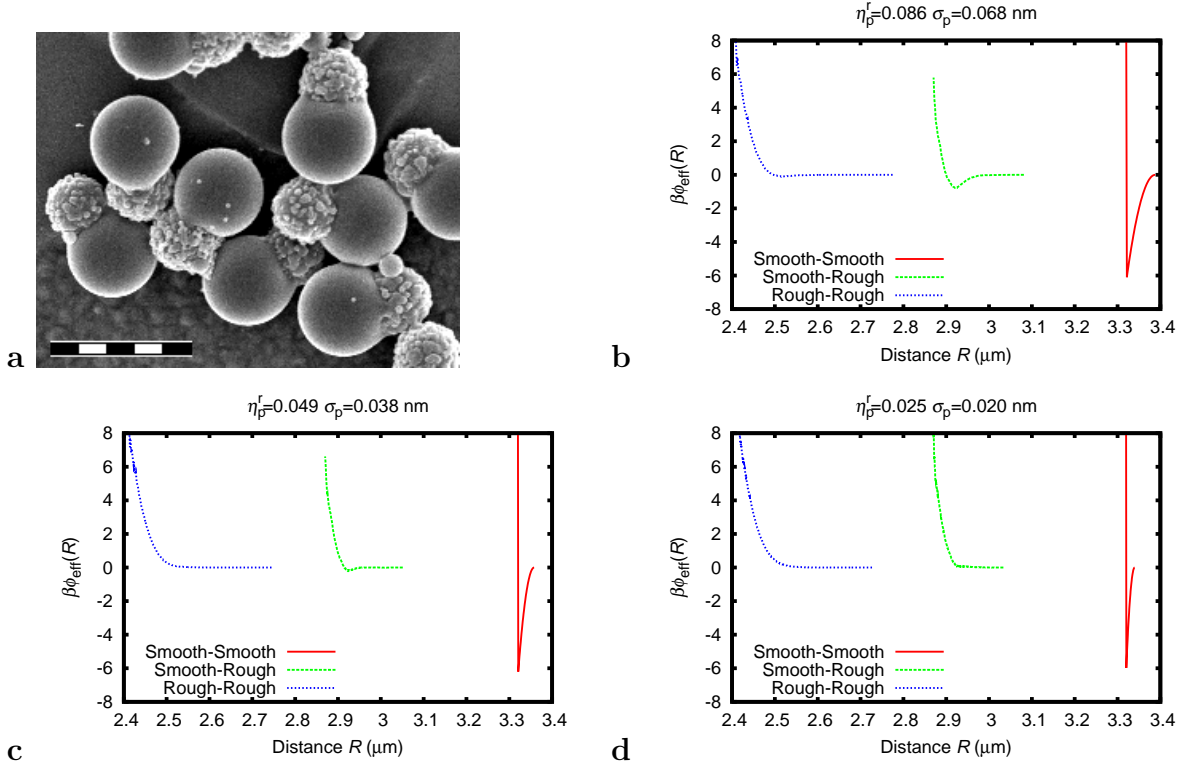


Figure 8.6: a) SEM image of the particles made by Kraft. The scalebar is 5 μm . b,c,d) The effective pair potentials $\beta\phi_{\text{eff}}(R)$ between various particles for varying polymer diameters σ_p and polymer reservoir packing fraction $\eta_p^r = z_p\pi\sigma^3/6$ with z_p the polymer fugacity. The smallest polymer with $\sigma_p = 20$ nm will most likely be of the same size as the stabilization layer and will therefore not work. The size ratio is 0.72, the large smooth spheres have a diameter of 3.32 μm , the rough spheres have a diameter of 2.4 μm including the small spheres and the small spheres have a diameter of 182 nm.

approximately $\eta_p^r = 0.09$. For the smaller polymers the effect becomes stronger. For the polymers with a diameter of 38 nm the attraction is 38 times stronger between the smooth particles than between a smooth and a rough particle, while the volume fraction required for $6 k_B T$ attraction is only $\eta_p^r = 0.05$. We have modeled the dumbbell particles as two separate disconnected spheres. When dumbbells touch at the connecting point (neck) the overlap of the excluded volume is larger than when they only connect sphere to sphere. We expect that this configuration is only favorable when the smooth sides feel a significant attraction towards the rough spheres.

We also calculated the effective pair potential for a second system synthesized by Kraft with large rough spheres and small smooth spheres. The results are similar as for the other system except for the size difference between the smooth and rough particles. The smooth spheres in this system have a diameter of 2.22 μm , the rough spheres have a diameter of 2.92 μm including the rough surface layer, the small spheres that form the roughness have a diameter of 185 nm and the polymers have diameters of 20, 38 and 68 nm. In Fig. 8.7 we plot the effective pair potential between the different sides of the dumbbell.

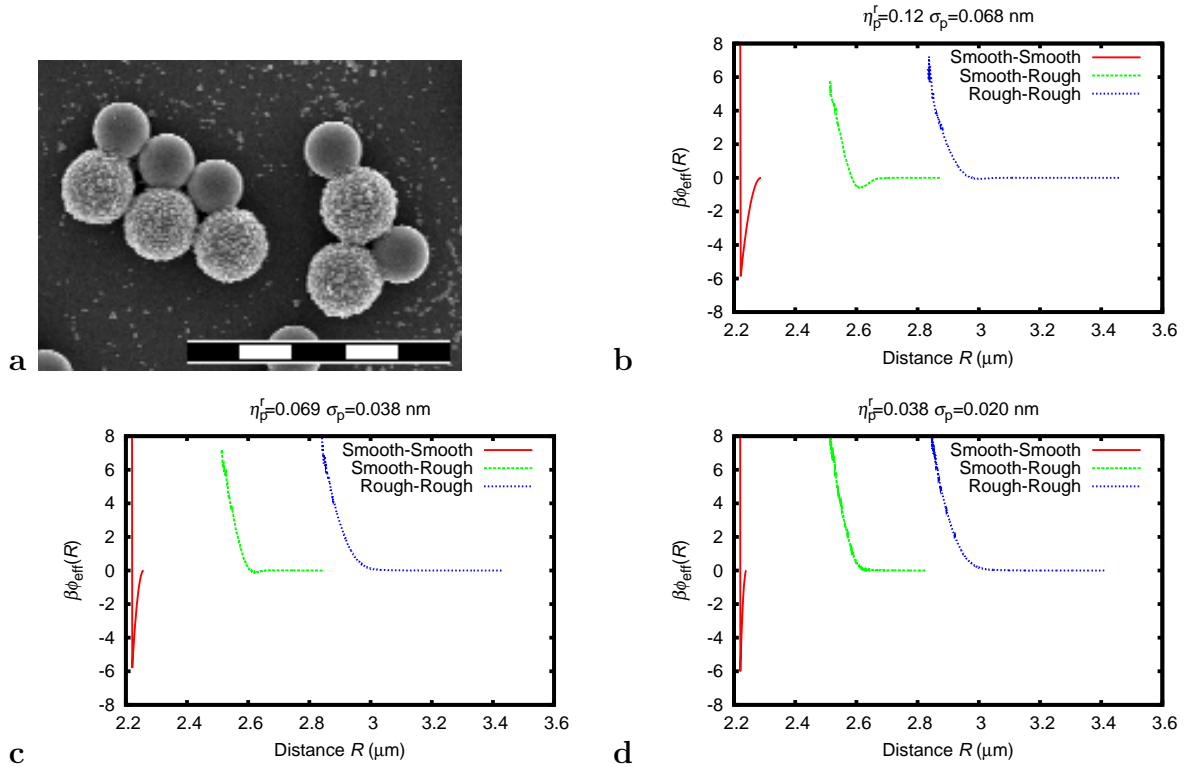


Figure 8.7: a) SEM image of the particles made by Kraft. The scalebar is 10 μm . b,c,d) The effective pair potentials $\beta\phi_{\text{eff}}(R)$ between various particles for varying polymer diameters σ_p and polymer reservoir packing fraction $\eta_p^r = z_p\pi\sigma_p^3/6$ with z_p the polymer fugacity. The size ratio is 1.32, the large rough spheres have a diameter of 2.92 μm including the rough particle.

8.3.4 Effect of charge stabilization

For charge stabilized particles there is a lower bound on the polymer size. If the polymer is smaller than the thickness of this stabilization layer the particles will aggregate irreversibly when they are pushed through the stabilization layer or will not feel the attraction at all when the charge keeps the colloids apart. Since the polymer is expected to feel little or no effect of the surface charge of the particles, charge stabilization will effectively increase the distance the particles can approach each other, while the polymers can still enter this exclusion layer. This has the same effect as the roughness of the particles: it will decrease the effective attraction. To investigate the effect of a thin double layer on the interaction we performed measurements of the pair potential between rough and smooth particles with differently sized exclusion layers. We assumed that the exclusion layers are hard for the hard core of other colloids (can not be penetrated) but not for the polymers and the stabilization layer of other colloids.

For sterically stabilized systems the situation is different since the dense steric layer is expected to exclude the polymer as well. The steric stabilization will only increase the size of the colloids slightly. When the steric layer is smaller than the coated particles that are used for the surface roughness, this should not have a significant effect. If the stabilization layer does not limit the size of the polymers the only remaining limitation

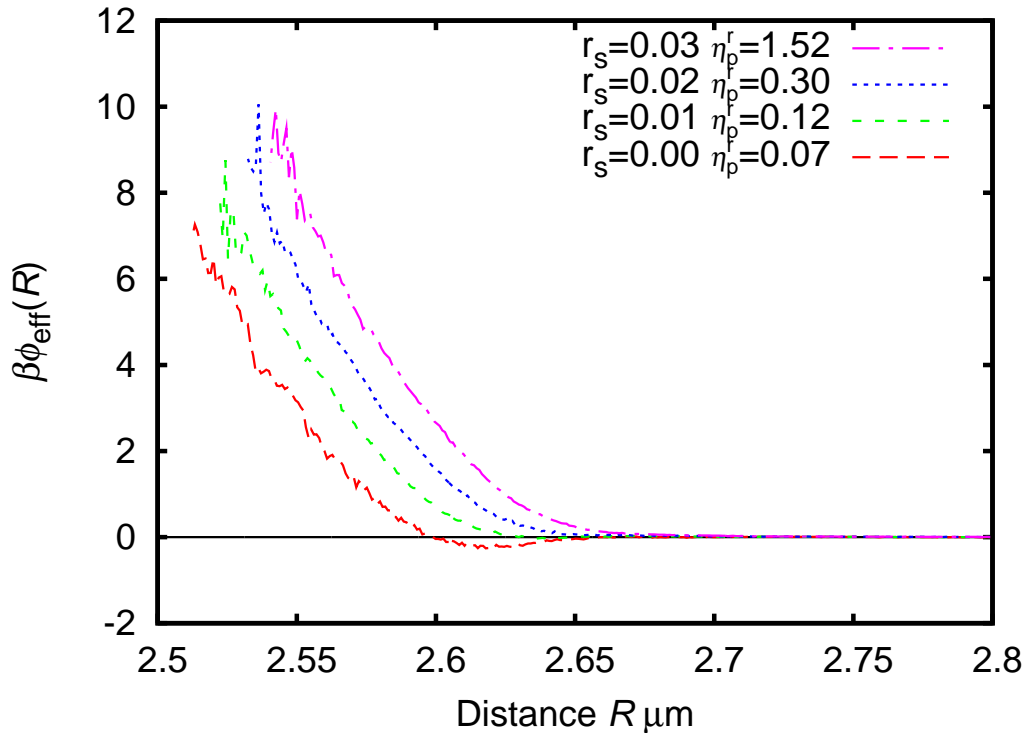


Figure 8.8: The effective pair potential between a smooth sphere with a diameter of $2.22 \mu\text{m}$ and a rough sphere with a diameter of $2.37 \mu\text{m}$ covered with 900 small spheres with diameter $\sigma_{\text{small}} = 0.18 \mu\text{m}$. The diameter of the polymers $\sigma_p = 38 \text{ nm}$. The thickness of the stabilization layer and the polymer reservoir packing fraction are varied as labeled. The polymer reservoir packing fraction is chosen such that the attraction between the smooth colloids is $6 k_B T$.

is the roughness of the colloidal spheres. The surface roughness of the colloids should be smaller than twice the radius of gyration of the polymers otherwise this roughness reduces the attraction.

We have used the parameters of an experimental system, which was recently synthesized by Kraft. In Fig. 8.8 we plot the effective pair potential between a smooth sphere with diameter $2.22 \mu\text{m}$ and a sphere of $2.37 \mu\text{m}$ covered with 900 small spheres with a diameter of $0.18 \mu\text{m}$ and a total diameter of $2.8\text{-}3.0 \mu\text{m}$. The polymer has a radius of gyration of 19 nm resulting in an effective diameter of diameter of 28 nm . The effective attraction between the smooth spheres is again fixed at $6 k_B T$. The small attractive well, that is visible for colloids without stabilization layer, slowly disappears when the stabilization layer is increased in thickness, however, the fugacity of the polymers required also increases dramatically. For the stabilization layer of $0.03 \mu\text{m}$ the polymer concentration would be so high that the volume fraction would be well inside the semi-dilute regime. For these high volume fractions our assumption of ideal polymers starts to fail. When the polymers are in the semi-dilute regime the range of the attraction will be less than expected from ideal polymers, which will increase the effect of the stabilization layer and the concentration of polymers required [148]. The stabilization does slightly increase the effect of the rough surface, however, the main effect of the stabilization layer is that it

will increase the concentration of polymers required.

Preliminary experiments performed by Kraft showed that there is a stronger attraction between the smooth sides than between the rough sides in agreement with these calculations. The best results were obtained with polymers with a diameter of 38 nm. When the smallest polymers were used they did not result in a significant attraction, so most likely the attraction is reduced by the steric layer. The experiments were performed at higher polymer concentration than the concentrations predicted here.

8.4 Conclusion

We show that surface roughness is a viable method to tune depletion attractions even between spheres. We show that coating a large sphere with small spheres is a good method to modify the surface roughness. The size of the small colloids should be chosen as small as possible while they are still larger than the polymers which should in turn be larger than the screening length and the roughness of the colloid surface. When the surface is covered with a half filled layer of particles the attraction is reduced most effectively. The smaller the polymers the stronger the effect of the roughness. However, the polymer has to be larger than the stabilization layer on the colloids otherwise the volume fraction of polymer required will be so high that the assumption of an ideal polymer will break down.

The experiments performed by Kraft and Van Kats show that the roughness can reduce the depletion attraction of spherical particles as predicted by the calculations performed here. However, the experiments required higher polymer concentrations than would be expected from our calculations. This is most likely caused by the charge of the particles. When we have a charged stabilization layer of 20 nm and a polymer with a diameter of 38 nm the volume fraction of the polymer required for significant attraction goes up by a factor of four. The knowledge of the pair interactions which have been calculated here makes it possible to perform coarse grained simulations to predict the phase behaviour of spherical particles with rough surfaces and smooth surfaces.

8.5 Acknowledgements

I would like to acknowledge C. van Kats and D. Kraft for particle synthesis.

References

- [1] W. Hoover and F. Ree, *Melting transition and communal entropy for hard spheres*, J. Chem. Phys. **49**, 3609 (1968).
- [2] A.-P. Hynninen and M. Dijkstra, *Phase diagram of dipolar hard and soft spheres: Manipulation of colloidal crystal structures by an external field*, Phys. Rev. Lett. **94**, 138303 (2005).
- [3] U. Dassanayake, S. Fraden, and A. van Blaaderen, *Structure of electrorheological fluids*, J. Chem. Phys. **112**, 3851 (2000).
- [4] M. Sullivan, K. Zhao, C. Harrison, R. H. Austin, M. Megens, A. Hollingsworth, W. B. Russel, Z. Cheng, T. Mason, and P. M. Chaikin, *Control of colloids with gravity, temperature gradients, and electric fields*, J. Phys. Cond. Matt. **15**, S11 (2003).
- [5] A. Ashkin, *Acceleration and trapping of particles by radiation pressure*, Phys. Rev. Lett. **24**, 156 (1970).
- [6] D. Frenkel and B. Smit, *Understanding molecular simulation: from algorithms to applications* (Academic Press, New York, 1996).
- [7] M. Allen and D. Tildesley, *Computer simulation of liquids* (Oxford University Press, USA, 1990).
- [8] G. M. Torrie and J. P. Valleau, *Monte carlo free energy estimates using non-boltzmann sampling: Application to the sub-critical lennard-jones fluid*, Chemical Physics Letters **28**, 578 (1974).
- [9] B. Cichocki and K. Hinsen, *Dynamic computer simulation of concentrated hard sphere suspensions : I. simulation technique and mean square displacement data*, Phys. A. **166**, 473 (1990).
- [10] P. G. Bolhuis, D. Frenkel, S. Mau, and D. A. Huse, *Entropy difference between crystal phases*, Nature **388**, 235 (1997).
- [11] C. A. Angell, K. L. Ngai, G. B. McKenna, P. F. McMillan, and S. W. Martin, *Relaxation in glassforming liquids and amorphous solids*, Journal of Applied Physics **88**, 3113 (2000).
- [12] J. Mattsson, H. Wyss, A. Fernandez-Nieves, K. Miyazaki, Z. Hu, D. Reichman, and D. Weitz, *Soft colloids make strong glasses*, Nature **462**, 83 (2009).
- [13] H. Osada, *Positivity of the self-diffusion matrix of interacting brownian particles with hard core*, Probability Theory and Related Fields **112**, 53 (1998).
- [14] P. J. Steinhardt, D. R. Nelson, and M. Ronchetti, *Bond-orientational order in liquids and glasses*, Phys. Rev. B **28**, 784 (1983).
- [15] P. R. ten Wolde, M. J. Ruiz-Montero, and D. Frenkel, *Numerical evidence for bcc ordering at the surface of a critical fcc nucleus*, Phys. Rev. Lett. **75**, 2714 (1995).
- [16] W. Lechner and C. Dellago, *Accurate determination of crystal structures based on averaged local bond order parameters*, J. Chem. Phys. **129**, 114707 (2008).
- [17] G. S. C., *Colloids reinforce glass theory*, Physics World **13**, 22 (2000).
- [18] A. P.W., *Through the glass lightly*, Science **267**, 1615 (1995).

-
- [19] W. Kauzmann, *The nature of the glassy state and the behavior of liquids at low temperatures.*, Chemical Reviews **43**, 219 (1948).
- [20] C. A. Angell, *The old problems of glass and the glass transition, and the many new twists*, Proc. Natl. Acad. Sci. of the United States of America **92**, 6675 (1995).
- [21] L. Woodcock, *Glass transition in the hard-sphere model*, J. Chem. Soc., Faraday Trans. 2 **72**, 1667 (1976).
- [22] R. J. Speedy, *On the reproducibility of glasses*, J. Chem. Phys. **100**, 6684 (1994).
- [23] M. D. Rintoul and S. Torquato, *Metastability and crystallization in hard-sphere systems*, Phys. Rev. Lett. **77**, 4198 (1996).
- [24] A. Donev, F. H. Stillinger, and S. Torquato, *Do binary hard disks exhibit an ideal glass transition?*, Phys. Rev. Lett. **96**, 225502 (2006).
- [25] L. Santen and W. Krauth, *Absence of thermodynamic phase transition in a model glass former*, Nature **405**, 550 (2000).
- [26] F. Z. Giorgio Parisi, *Mean field theory of hard sphere glasses and jamming*, arXiv **0802.2180**, (2008).
- [27] P. N. Pusey and W. van Meegen, *Phase behaviour of concentrated suspensions of nearly hard colloidal spheres*, Nature **320**, 340 (1986).
- [28] J. Zhu, M. Li, R. Rogers, W. Meyer, R. H. Ottewill, S. S. S. Crew, W. B. Russel, and P. M. Chaikin, *Crystallization of hard-sphere colloids in microgravity*, Nature **387**, 883 (1997).
- [29] N. B. Simeonova and W. K. Kegel, *Gravity-induced aging in glasses of colloidal hard spheres*, Phys. Rev. Lett. **93**, 035701 (2004).
- [30] W. van Meegen and S. M. Underwood, *Glass transition in colloidal hard spheres: Mode-coupling theory analysis*, Phys. Rev. Lett. **70**, 2766 (1993).
- [31] P. R. ten Wolde, M. J. Ruiz-Montero, and D. Frenkel, *Numerical evidence for bcc ordering at the surface of a critical fcc nucleus*, Phys. Rev. Lett. **75**, 2714 (1995).
- [32] S. R. Williams, I. K. Snook, and W. van Meegen, *Molecular dynamics study of the stability of the hard sphere glass*, Phys. Rev. E **64**, 021506 (2001).
- [33] M. Fasolo and P. Sollich, *Fractionation effects in phase equilibria of polydisperse hard-sphere colloids*, Phys. Rev. E **70**, 041410 (2004).
- [34] J. J. Erpenbeck and W. W. Wood, *Molecular dynamics calculations of the hard-sphere equation of state*, Journal of Statistical Physics **35**, 321 (1984).
- [35] S. R. Williams and A. P. Philipse, *Random packings of spheres and spherocylinders simulated by mechanical contraction*, Phys. Rev. E **67**, 051301 (2003).
- [36] B. D. Lubachevsky and F. H. Stillinger, *Geometric properties of random disk packings*, Journal of Statistical Physics **60**, 561 (1990).
- [37] N. F. Carnahan and K. E. Starling, *Equation of state for nonattracting rigid spheres*, J. Chem. Phys. **51**, 635 (1969).
- [38] G. Brambilla, D. El Masri, M. Pierno, L. Berthier, L. Cipelletti, G. Petekidis, and A. B. Schofield, *Probing the equilibrium dynamics of colloidal hard spheres above the mode-coupling glass transition*, Phys. Rev. Lett. **102**, 085703 (2009).

- [39] C. Bennemann, C. Donati, J. Baschnagel, and S. C. Glotzer, *Growing range of correlated motion in a polymer melt on cooling towards the glass transition*, Nature **399**, 246 (1999).
- [40] T. Hales, *A proof of the Kepler conjecture*, Annals of mathematics **162**, 1065 (2005).
- [41] A. van Blaaderen and P. Wiltzius, *Real-Space Structure of Colloidal Hard-Sphere Glasses*, Science **270**, 1177 (1995).
- [42] A. Liu and S. Nagel, *Jamming is not just cool any more*, Nature **396**, 21 (1998).
- [43] P. Ballesta, R. Besseling, L. Isa, G. Petekidis, and W. C. K. Poon, *Slip and flow of hard-sphere colloidal glasses*, Phys. Rev. Lett. **101**, 258301 (2008).
- [44] R. P. A. Dullens, D. G. A. L. Aarts, and W. K. Kegel, *Dynamic broadening of the crystal-fluid interface of colloidal hard spheres*, Phys. Rev. Lett. **97**, 228301 (2006).
- [45] G. Petekidis, A. Moussaïd, and P. N. Pusey, *Rearrangements in hard-sphere glasses under oscillatory shear strain*, Phys. Rev. E **66**, 051402 (2002).
- [46] W. K. Kegel and A. van Blaaderen, *Direct Observation of Dynamical Heterogeneities in Colloidal Hard-Sphere Suspensions*, Science **287**, 290 (2000).
- [47] R. D. Kamien and A. J. Liu, *Why is random close packing reproducible?*, Phys. Rev. Lett. **99**, 155501 (2007).
- [48] S. Torquato, T. Truskett, and P. Debenedetti, *Is Random Close Packing of Spheres Well Defined?*, Phys. Rev. Lett. **84**, 2064 (2000).
- [49] M. Rintoul and S. Torquato, *Computer simulations of dense hard-sphere systems*, J. Chem. Phys. **105**, 9258 (1996).
- [50] L. V. Woodcock and C. A. Angell, *Diffusivity of the hard-sphere model in the region of fluid metastability*, Phys. Rev. Lett. **47**, 1129 (1981).
- [51] R. Speedy, *The hard sphere glass transition*, Mol. Phys. **95**, 169 (1998).
- [52] R. Mari, F. Krzakala, and J. Kurchan, *Jamming versus glass transitions*, Phys. Rev. Lett. **103**, 025701 (2009).
- [53] I. Biazzo, F. Caltagirone, G. Parisi, and F. Zamponi, *Theory of amorphous packings of binary mixtures of hard spheres*, Phys. Rev. Lett. **102**, 195701 (2009).
- [54] L. Berthier and T. A. Witten, *Glass transition of dense fluids of hard and compressible spheres*, Phys. Rev. E **80**, 021502 (2009).
- [55] W. Schaertl and H. Sillescu, *Brownian dynamics of polydisperse colloidal hard spheres: Equilibrium structures and random close packings*, Journal of Statistical Physics **77**, 1007 (1994).
- [56] G. Nolan and P. Kavanagh, *Computer simulation of random packing of hard spheres*, Powder technology **72**, 149 (1992).
- [57] D. E. Masri, G. Brambilla, M. Pierno, G. Petekidis, A. B. Schofield, L. Berthier, and L. Cipelletti, *Dynamic light scattering measurements in the activated regime of dense colloidal hard spheres*, Journal of Statistical Mechanics **2009**, P07015 (28pp) (2009).
- [58] C. S. O'Hern, L. E. Silbert, A. J. Liu, and S. R. Nagel, *Jamming at zero temperature and zero applied stress: The epitome of disorder*, Phys. Rev. E **68**, 011306 (2003).
- [59] N. Xu, J. Blawdziewicz, and C. S. O'Hern, *Random close packing revisited: Ways to pack frictionless disks*, Phys. Rev. E **71**, 061306 (2005).

- [60] L. B. P. Chaudhuri and S. Sastry, *Jamming transitions in amorphous packings of frictionless spheres occur over a continuous range of volume fractions*, arXiv **0910:0364**, (2009).
- [61] R. Speedy, *On the reproducibility of glasses*, J. Chem. Phys. **100**, 6684 (1994).
- [62] A. Kansal, S. Torquato, and F. Stillinger, *Computer generation of dense polydisperse sphere packings*, J. Chem. Phys. **117**, 8212 (2002).
- [63] N. Carnahan and K. Starling, *Equation of State for Nonattracting Rigid Spheres*, J. Chem. Phys. **51**, 635 (1969).
- [64] W. Kauzmann, *The glassy state and the behaviour of liquids at low temperature*, Chem Rev **43**, 219 (1948).
- [65] S. Torquato and F. H. Stillinger, *Multiplicity of generation, selection, and classification procedures for jammed Hard-Particle packings*, J. Chem. Phys. B **105**, 11849 (2001).
- [66] A. Donev, S. Torquato, and F. H. Stillinger, *Pair correlation function characteristics of nearly jammed disordered and ordered hard-sphere packings*, Phys. Rev. E **71**, 011105 (2005).
- [67] Z. W. Salsburg and W. W. Wood, *Equation of state of classical hard spheres at high density*, J. Chem. Phys. **37**, 798 (1962).
- [68] S. Torquato and F. H. Stillinger, *Controlling the Short-Range order and packing densities of Many-Particle systems*, J. Chem. Phys. B **106**, 8354 (2002).
- [69] P. Bartlett, P. N. Pusey, and R. H. Ottewill, *Colloidal crystallization under time-averaged zero gravity*, Langmuir **7**, 213 (1991).
- [70] M. Dijkstra, *Capillary freezing or complete wetting of hard spheres in a planar hard slit?*, Phys. Rev. Lett. **93**, 108303 (2004).
- [71] M. T. Sullivan, K. Zhao, A. D. Hollingsworth, R. H. Austin, W. B. Russel, and P. M. Chaikin, *An electric bottle for colloids*, Phys. Rev. Lett. **96**, 015703 (2006).
- [72] M. Leunissen, Ph.D. thesis, Utrecht University, 2007.
- [73] A. van Blaaderen and P. Wiltzius, *Real-space structure of colloidal hard-sphere glasses*, Science **270**, 1177 (1995).
- [74] M. Hermes and M. Dijkstra, *Jamming of polydisperse hard spheres: The effect of kinetic arrest*, Europhys. Lett. **89**, 38005 (2010).
- [75] P. N. Pusey, E. Zaccarelli, C. Valeriani, E. Sanz, W. C. K. Poon, and M. E. Cates, *Hard spheres: crystallization and glass formation*, Royal Society of London Philosophical Transactions Series A **367**, 4993 (2009).
- [76] W. Kegel and A. van Blaaderen, *Direct Observation of Dynamical Heterogeneities in Colloidal Hard-Sphere Suspensions*, Science **287**, 290 (2000).
- [77] P. Bartlett and R. Ottewill, *Gravitational effects on the phase behaviour of dispersions*, Adv. Coll. Int. Sci. **50**, 39 (1994).
- [78] Y. Jin and H. Makse, *A first-order phase transition at the random close packing of hard spheres*, preprint , arXiv:1001.5287 (2010).
- [79] J. Crocker and D. Grier, *Methods of digital video microscopy for colloidal studies*, Journal of Colloid and Interface Science **179**, 298 (1996).

- [80] P. ten Wolde, M. Ruiz-Montero, and D. Frenkel, *Numerical calculation of the rate of crystal nucleation in a Lennard-Jones system at moderate undercooling*, J. Chem. Phys. **104**, 9932 (1996).
- [81] A. S. Clarke and H. Jónsson, *Structural changes accompanying densification of random hard-sphere packings*, Phys. Rev. E **47**, 3975 (1993).
- [82] J. Hoogenboom, P. Vergeer, and A. van Blaaderen, *A real-space analysis of colloidal crystallization in a gravitational field at a flat bottom wall*, J. Chem. Phys. **119**, 3371 (2003).
- [83] M. E. Leunissen and A. van Blaaderen, *Concentrating colloids with electric field gradients. ii. phase transitions and crystal buckling of long-ranged repulsive charged spheres in an electric bottle*, J. Chem. Phys. **128**, 164509 (2008).
- [84] A. Dinsmore, E. Weeks, V. Prasad, A. Levitt, and D. Weitz, *Three-dimensional confocal microscopy of colloids*, Applied Optics **40**, 4152 (2001).
- [85] A. Yethiraj, *Tunable colloids: control of colloidal phase transitions with tunable interactions*, Soft Matter **3**, 1099 (2007).
- [86] S. Lee, Y. Roichman, G. Yi, S. Kim, S. Yang, A. Van Blaaderen, P. Van Oostrum, and D. Grier, *Characterizing and tracking single colloidal particles with video holographic microscopy*, Opt. Express **15**, 18275 (2007).
- [87] T. Palberg, *Crystallization kinetics of repulsive colloidal spheres*, J. Phys. Cond. Matt. **11**, R323 (1999).
- [88] J. L. Harland and W. van Meegen, *Crystallization kinetics of suspensions of hard colloidal spheres*, Phys. Rev. E **55**, 3054 (1997).
- [89] C. Sinn, A. Heymann, A. Stipp, and T. Palberg, *Solidification kinetics of hard-sphere colloidal suspensions*, Progress in colloid & polymer science **118**, 266 (2001).
- [90] U. Gasser, E. R. Weeks, A. Schofield, P. N. Pusey, and D. A. Weitz, *Real-Space imaging of nucleation and growth in colloidal crystallization*, Science **292**, 258 (2001).
- [91] S. Auer and D. Frenkel, *Prediction of absolute crystal-nucleation rate in hard-sphere colloids*, Nature **409**, 1020 (2001).
- [92] R. J. Allen, P. B. Warren, and P. R. ten Wolde, *Sampling rare switching events in biochemical networks*, Phys. Rev. Lett. **94**, 018104 (2005).
- [93] C. Dellago, P. G. Bolhuis, F. S. Csajka, and D. Chandler, *Transition path sampling and the calculation of rate constants*, J. Chem. Phys. **108**, 1964 (1998).
- [94] J. S. van Duijneveldt and D. Frenkel, *Computer simulation study of free energy barriers in crystal nucleation*, J. Chem. Phys. **96**, 4655 (1992).
- [95] P. ten Wolde, M. Ruiz-Montero, and D. Frenkel, *Simulation of homogeneous crystal nucleation close to coexistence*, Faraday Discuss **104**, 93 (1996).
- [96] B. J. Alder and T. E. Wainwright, *Studies in molecular dynamics. i. general method*, J. Chem. Phys. **31**, 459 (1959).
- [97] S. Auer and D. Frenkel, *Line tension controls wall-induced crystal nucleation in hard-sphere colloids*, Phys. Rev. Lett. **91**, 015703 (2003).
- [98] R. L. Davidchack, J. R. Morris, and B. B. Laird, *The anisotropic hard-sphere crystal-melt interfacial free energy from fluctuations*, J. Chem. Phys. **125**, 094710 (2006).

- [99] B. O'Malley and I. Snook, *Crystal nucleation in the hard sphere system*, Phys. Rev. Lett. **90**, 085702 (2003).
- [100] Y. He, B. Olivier, and B. J. Ackerson, *Morphology of crystals made of hard spheres*, Langmuir **13**, 1408 (1997).
- [101] E. Zaccarelli, C. Valeriani, E. Sanz, W. C. K. Poon, M. E. Cates, and P. N. Pusey, *Crystallization of hard-sphere glasses*, Phys. Rev. Lett. **103**, 135704 (2009).
- [102] A. van Blaaderen, R. Ruel, and P. Wiltzius, *Template-directed colloidal crystallization*, Nature **385**, 321 (1997).
- [103] D. Vossen, A. van der Horst, M. Dogterom, and A. van Blaaderen, *Optical tweezers and confocal microscopy for simultaneous three-dimensional manipulation and imaging in concentrated colloidal dispersions*, Review of Scientific Instruments **75**, 2960 (2004).
- [104] P. Lodahl, A. van Driel, I. Nikolaev, A. Irman, K. Overgaag, D. Vanmaekelbergh, and W. Vos, *Controlling the dynamics of spontaneous emission from quantum dots by photonic crystals*, Nature **430**, 654 (2004).
- [105] J. P. Hoogenboom, A. K. van Langen-Suurling, J. Romijn, and A. van Blaaderen, *Hard-sphere crystals with hcp and non-close-packed structure grown by colloidal epitaxy*, Phys. Rev. Lett. **90**, 138301 (2003).
- [106] P. Schall, I. Cohen, D. A. Weitz, and F. Spaepen, *Visualization of Dislocation Dynamics in Colloidal Crystals*, Science **305**, 1944 (2004).
- [107] V. W. A. de Villeneuve, R. P. A. Dullens, D. G. A. L. Aarts, E. Groeneveld, J. H. Scherff, W. K. Kegel, and H. N. W. Lekkerkerker, *Colloidal Hard-Sphere Crystal Growth Frustrated by Large Spherical Impurities*, Science **309**, 1231 (2005).
- [108] A. Cacciuto, S. Auer, and D. Frenkel, *Onset of heterogeneous crystal nucleation in colloidal suspensions*, Nature **428**, 404 (2004).
- [109] G. H. Gelinck, H. E. A. Huitema, E. van Veenendaal, E. Cantatore, L. Schrijnemakers, J. B. P. H. van der Putten, T. C. T. Geuns, M. Beenhakkers, J. B. Giesbers, B. Huisman, E. J. Meijer, E. M. Benito, F. J. Touwslager, A. W. Marsman, B. J. E. van Rens, and D. M. de Leeuw, *Flexible active-matrix displays and shift registers based on solution-processed organic transistors*, Nat Mater **3**, 106 (2004).
- [110] S. Auer and F. D. *Advanced Computer Simulation, Approaches for Soft Matter Sciences I*, volume 173 of *Advances in Polymer Science*, chapter Numerical Simulations of Crystal Nucleation in Colloids, pages 149–208. Springer Berlin / Heidelberg, (2005).
- [111] A. Cacciuto and D. Frenkel, *Simulation of colloidal crystallization on finite structured templates*, Phys. Rev. E **72**, 041604 (2005).
- [112] P. N. Pusey, W. van Meegen, P. Bartlett, B. J. Ackerson, J. G. Rarity, and S. M. Underwood, *Structure of crystals of hard colloidal spheres*, Phys. Rev. Lett. **63**, 2753 (1989).
- [113] C. Graf, D. L. J. Vossen, A. Imhof, and A. van Blaaderen, *A general method to coat colloidal particles with silica*, Langmuir **19**, 6693 (2003).
- [114] J. S. van Duijneveldt and D. Frenkel, *Computer simulation study of free energy barriers in crystal nucleation*, J. Chem. Phys. **96**, 4655 (1992).
- [115] G. Bosma, C. Pathmamanoharan, E. de Hoog, W. Kegel, A. van Blaaderen, and H. Lekkerkerker, *Preparation of monodisperse, fluorescent PMMA-latex colloids by dispersion polymerization*, Journal of colloid and interface science **245**, 292 (2002).

- [116] Y. L. Wu, Ph.D. thesis, Utrecht University, 2007.
- [117] S. Kumar and R. G. Larson, *Shear banding and secondary flow in viscoelastic fluids between a cone and plate*, Journal of Non-Newtonian Fluid Mechanics **95**, 295 (2000).
- [118] R. Blaak, S. Auer, D. Frenkel, and H. Löwen, *Crystal nucleation of colloidal suspensions under shear*, Phys. Rev. Lett. **93**, 068303 (2004).
- [119] J. J. Erpenbeck, *Shear viscosity of the hard-sphere fluid via nonequilibrium molecular dynamics*, Phys. Rev. Lett. **52**, 1333 (1984).
- [120] S. Butler and P. Harrowell, *Shear induced ordering in simulations of colloidal suspensions: Oscillatory shear and computational artefacts*, J. Chem. Phys. **105**, 605 (1996).
- [121] J. Delhomelle, J. Petracic, and D. J. Evans, *Reexamination of string phase and shear thickening in simple fluids*, Phys. Rev. E **68**, 031201 (2003).
- [122] Y. L. Wu, D. Derks, A. van Blaaderen, and A. Imhof, *Melting and crystallization of colloidal hard-sphere suspensions under shear*, Proc. Natl. Acad. Sci. **106**, 10564 (2009).
- [123] G. Bossis and J. F. Brady, *Dynamic simulation of sheared suspensions. i. general method*, J. Chem. Phys. **80**, 5141 (1984).
- [124] R. C. Ball and J. R. Melrose, *Lubrication breakdown in hydrodynamic simulations of concentrated colloids*, Adv. Coll. Int. Sci. **59**, 19 (1995).
- [125] J. F. Brady, *Computer simulation of viscous suspensions*, Chemical Engineering Science **56**, 2921 (2001).
- [126] G. D. Scott, A. M. Charlesworth, and M. K. Mak, *On the random packing of spheres*, J. Chem. Phys. **40**, 611 (1964).
- [127] N. Duff and D. J. Lacks, *Shear-induced crystallization in jammed systems*, Phys. Rev. E **75**, 031501 (2007).
- [128] P. A. Smith, G. Petekidis, S. U. Egelhaaf, and W. C. K. Poon, *Yielding and crystallization of colloidal gels under oscillatory shear*, Phys. Rev. E **76**, 041402 (2007).
- [129] B. J. Ackerson and P. N. Pusey, *Shear-induced order in suspensions of hard spheres*, Phys. Rev. Lett. **61**, 1033 (1988).
- [130] B. J. Ackerson, *Shear induced order and shear processing of model hard sphere suspensions*, Journal of Rheology **34**, 553 (1990).
- [131] M. D. Haw, W. C. K. Poon, and P. N. Pusey, *Direct observation of oscillatory-shear-induced order in colloidal suspensions*, Phys. Rev. E **57**, 6859 (1998).
- [132] W. Xue and G. S. Grest, *Shear-induced alignment of colloidal particles in the presence of a shear flow*, Phys. Rev. Lett. **64**, 419 (1990).
- [133] H. Komatsugawa and S. Nosé, *Nonequilibrium phase diagram of a polydisperse system: A molecular dynamics study*, J. Chem. Phys. **112**, 11058 (2000).
- [134] G. Ciccotti, R. Kapral, and A. Sergi, *Non-Equilibrium Molecular Dynamics*, Handbook of Materials Modeling , 745 (2005).
- [135] J. Weeks, D. Chandler, and H. Andersen, *Role of repulsive forces in determining the equilibrium structure of simple liquids*, J. Chem. Phys. **54**, 5237 (1971).
- [136] Y. Yan, J. Dhont, C. Smits, and H. Lekkerkerker, *Oscillatory-shear-induced order in non-aqueous dispersions of charged colloidal spheres*, Phys. A. **202**, 68 (1994).

- [137] S. E. Paulin, B. J. Ackerson, and M. S. Wolfe, *Equilibrium and shear induced nonequilibrium phase behavior of pmma microgel spheres*, Journal of Colloid and Interface Science **178**, 251 (1996).
- [138] J. Delhomelle, J. Petracic, and D. J. Evans, *Non-newtonian behavior in simple fluids*, J. Chem. Phys. **120**, 6117 (2004).
- [139] K. Strandburg and D. Nelson, *Bond orientational order in condensed matter systems* (New York, NY (United States); Springer-Verlag New York Inc., 1992).
- [140] D. Derks, Y. Wu, A. Blaaderen, and A. Imhof, *Dynamics of colloidal crystals in shear flow*, Soft Matter **5**, 1060 (2009).
- [141] S. Asakura and F. Oosawa, *On Interaction between Two Bodies Immersed in a Solution of Macromolecules*, J. Chem. Phys. **22**, 1255 (1954).
- [142] A. Vrij, *Polymers at interfaces and the interactions in colloidal dispersions*, Pure and Applied Chem. **48**, 471 (1976).
- [143] A. A. Louis, P. G. Bolhuis, E. J. Meijer, and J. P. Hansen, *Polymer induced depletion potentials in polymer-colloid mixtures*, J. Chem. Phys. **117**, 1893 (2002).
- [144] H. N. W. Lekkerkerker, W. C.-K. Poon, P. N. Pusey, A. Stroobants, and P. B. Warren, *Phase behaviour of colloid + polymer mixtures*, Europhys. Lett. **20**, 559 (1992).
- [145] D. G. A. L. Aarts, M. Schmidt, and H. N. W. Lekkerkerker, *Direct Visual Observation of Thermal Capillary Waves*, Science **304**, 847 (2004).
- [146] T. Eckert and E. Bartsch, *Re-entrant glass transition in a colloid-polymer mixture with depletion attractions*, Phys. Rev. Lett. **89**, 125701 (2002).
- [147] W. Poon, J. Selve, M. Robertson, S. Ilett, A. Pirie, and P. Pusey, *An experimental study of a model colloid-polymer mixture*, Journal de Physique II **3**, 1075 (1993).
- [148] P. G. Bolhuis, A. A. Louis, and J.-P. Hansen, *Influence of polymer-excluded volume on the phase-behavior of colloid-polymer mixtures*, Phys. Rev. Lett. **89**, 128302 (2002).
- [149] E. Meijer and D. Frenkel, *Colloids dispersed in polymer solutions. A computer simulation study*, J. Chem. Phys. **100**, 6873 (1994).
- [150] J. Y. Walz and A. Sharma, *Effect of long range interactions on the depletion force between colloidal particles*, Journal of Colloid and Interface Science **168**, 485 (1994).
- [151] R. Tuinier, J. Rieger, and C. G. de Kruif, *Depletion-induced phase separation in colloid-polymer mixtures*, Adv. Coll. Int. Sci. **103**, 1 (2003).
- [152] W. C. K. Poon, *The physics of a model colloid-polymer mixture*, J. Phys. Cond. Matt. **14**, R859 (2002).
- [153] A. Dinsmore, A. Yodh, and D. Pine, *Entropic control of particle motion using passive surface microstructures*, Nature **383**, 239 (1996).
- [154] K. Zhao and T. G. Mason, *Directing colloidal self-assembly through roughness-controlled depletion attractions*, Phys. Rev. Lett. **99**, 268301 (2007).
- [155] S. Badaire, C. Cottin-Bizonne, and A. D. Stroock, *Experimental Investigation of Selective Colloidal Interactions Controlled by Shape, Surface Roughness, and Steric Layers*, Langmuir **24**, 11451 (2008).
- [156] S. Harley, D. W. Thompson, and B. Vincent, *The adsorption of small particles onto larger particles of opposite charge direct electron microscope studies*, Colloids and Surfaces **62**, 163 (1992).

-
- [157] M. Dijkstra, R. van Roij, and R. Evans, *Direct simulation of the phase behavior of binary hard-sphere mixtures: Test of the depletion potential description*, Phys. Rev. Lett. **82**, 117 (1999).
- [158] M. Dijkstra, R. van Roij, and R. Evans, *Phase diagram of highly asymmetric binary hard-sphere mixtures*, Phys. Rev. E **59**, 5744 (1999).
- [159] M. Dijkstra, R. van Roij, and R. Evans, *Phase behavior and structure of binary hard-sphere mixtures*, Phys. Rev. Lett. **81**, 2268 (1998).
- [160] M. Dijkstra, J. M. Brader, and R. Evans, *Phase behaviour and structure of model colloid-polymer mixtures*, J. Phys. Cond. Matt. **11**, 10079 (1999).
- [161] J. M. Brader, R. Evans, and M. Schmidt, *Statistical mechanics of inhomogeneous model colloid-polymer mixtures*, Mol. Phys. **101**, 3349 (2003).
- [162] J. M. Brader, M. Dijkstra, and R. Evans, *Inhomogeneous model colloid-polymer mixtures: Adsorption at a hard wall*, Phys. Rev. E **63**, 041405 (2001).
- [163] A. P. Gast, C. K. Hall, and W. B. Russel, *Polymer-induced phase separations in nonaqueous colloidal suspensions*, Journal of Colloid and Interface Science **96**, 251 (1983).
- [164] S. Asakura and F. Oosawa, *Interaction between particles suspended in solutions of macromolecules*, Journal of Polymer Science **33**, 183 (1958).
- [165] D. Nagao, C. M. van Kats, K. Hayasaka, M. Sugimoto, M. Konno, A. Imhof, and A. van Blaaderen, *Synthesis of hollow asymmetrical silica dumbbells with a movable inner core*, Langmuir **26**, 5208 (2010).

Summary

Hard spheres are conceptually a very simple model system. Hard spheres have no interaction when they are not in contact and when they make contact they repel each other so that they never overlap. Aside from their theoretical simplicity and the relative ease with which the system can be simulated, there is another advantage of hard spheres, namely that colloids can be experimentally realized such that they are approximately hard spheres. The model hard sphere colloids used in this thesis are very small plastic (perspex) marbles colored with a fluorescent dye. The advantage of making them so small is that they move on their own because of their thermal motion. This thermal motion allows the particles to move around and reach thermal equilibrium. In this thesis we study the road towards equilibrium and examine why this road is sometimes long and sometimes short.

Hard sphere systems have a single first order phase transition between a fluid and solid phase. For a gas-liquid transition, attractions are required. When less than 49.4% of the volume is occupied by the spheres, the equilibrium phase of the system is a fluid phase. This fluid phase does not have any long range order. When hard spheres occupy more than 54.5% of the volume the equilibrium state is a crystal. The equilibrium hard sphere crystal is a face-centered-cubic crystal. This means that the unit cell of the crystal is cubic and has a particles on each of the 8 corners and one in the middle. However, hard spheres have a second crystal phase that is nearly as stable as the face-centered-cubic crystal: the hexagonal close packed crystal. As a result of the competition between these two phases many hard sphere crystals form a mixture of both phases. The amount of face centered cubic crystal that is formed depends on the speed at which the crystal is grown. A slowly grown crystal contains more face-centered-cubic parts, whereas a rapidly grown crystal contains a mixture of both.

The easiest method to bring a hard sphere system out of equilibrium is to change its density. When hard spheres are compressed fast they can end up in a glass state. This glass state looks just like the fluid phase except that it does not flow. The particles still move but on short time scales they rattle around in the cages built by the neighboring particles. When a glass is studied for long times it becomes apparent that the particles still move longer distances. Their movement is different from what it would be in a fluid in which particles move individually. In a glass the particles move collectively; whole groups of particles rearrange as if they are attached to each other. The denser the glass the larger the groups of collectively moving particles become.

In chapter 2, we use Molecular Dynamics simulations to study the properties of hard sphere glasses. We determine the pressure as a function of density for the metastable fluid for hard spheres with a size polydispersity of 10%. Polydisperse spheres were used to hinder the formation of crystals. We find a jump in the slope of the isothermal compressibility. This is interesting because the isothermal compressibility is a thermodynamic quantity that changes abruptly at the dynamic fluid to glass transition. Such a signature of a dynamic transition has also been observed for molecular liquids at the glass transition.

When these hard sphere glasses are compressed past the transition described in chapter 2 the pressure increases steeply until the system becomes completely jammed. In chapter 3, we study the jammed configurations of polydisperse colloidal hard spheres as a function of compression speed and size polydispersity. We find that the system does not jam at one specific point, but rather somewhere in an entire regime of densities (at which the system can become stuck). The density at which the system jams is determined by the compression speed.

In chapter 4, we experimentally examine configurations that contain both crystalline and glassy parts. We study the effects of different compression rates induced by electric field gradients and a gravitational field on the crystallization and glass formation. We show that the glass transition becomes intermixed with the processes of crystal nucleation and growth and thus strongly depends on the compression rate. We show that gravity has an influence on the glass transition by increasing the compression rate.

The aim of chapter 5 is to test two different simulation techniques to calculate the rate at which a system nucleates. One simulation technique measures the nucleation rate directly while the other is more efficient but requires additional assumptions. This study is inspired by a difference of several orders of magnitude between nucleation rates obtained from experiments and previous simulations. We find that the two techniques yield similar results for the nucleation rate as well as the critical nucleus shape. From this we conclude that the simulation techniques are valid and that the cause of the discrepancy between experiments and simulations has to be found elsewhere.

Nucleation is a rare event and therefore difficult to study. To be able to investigate nucleation we studied seeded crystal growth with a template of particles trapped with optical tweezers. In addition we performed molecular dynamics simulations on an identical template. We initiate the nucleation process with the template and show that the template shape determines the final crystal shape and orientation. Furthermore we show that defects can play an important role in the growth of the crystal. This part of our research is described in chapter 6.

In chapter 7, we investigated the non-equilibrium phase behaviour of colloidal hard spheres in oscillatory shear. We perform experiments on an equilibrium fluid phase below the coexistence density of the fluid. We show that we can induce order in an equilibrium fluid using oscillatory shear. We find five different phases for varying frequency and amplitude: four known phases and one new phase. The formation of all phases occurs via nucleation and growth and the melting, when the shear is stopped, starts on the edges and the defects of the crystal phases. Some phases are very unstable without shear and melt very quickly, whereas others melt very slowly.

In chapter 8 we investigate the interactions between rough colloidal particles in the presence of polymers. Polymers cause effective attractions between the colloidal particles: the depletion interaction. Here we investigate whether surface roughness can be used to reduce depletion attraction. We find that when the polymer is smaller than the surface roughness the attraction can be reduced significantly. The exact numbers depend on the details of the system, however, for particles that were recently synthesized by Van Kats and Kraft we expect that a reduction of one order of magnitude can be obtained easily.

Samenvatting

Harde bollen vormen een van de eenvoudigste modelsystemen. Harde bollen hebben net als knikkers geen interactie wanneer ze geen contact maken en wanneer ze contact maken duwen ze elkaar zo hard weg dat ze nooit zullen overlappen. Door deze eenvoudige interactie zijn computersimulaties relatief eenvoudig. Een ander voordeel van harde bollen als modelsysteem is dat colloïden zo gemaakt kunnen worden dat ze heel erg op harde bollen lijken. De colloïden die in dit proefschrift gebruikt worden zijn hele kleine plastic (perspex) knikkers die gekleurd zijn met een fluorescente kleurstof. Doordat ze zo klein zijn, zijn de thermische fluctuaties voldoende om ze uit zichzelf te laten bewegen. Deze beweging, ook Brownse beweging genoemd, zorgt ervoor dat de colloïden thermodynamisch evenwicht kunnen bereiken en niet zoals knikkers gewoon blijven liggen waar ze liggen.

Harde bollen hebben een eerste-orde faseovergang tussen een vloeistof en een vaste stof. Wanneer van het totale volume minder dan 49.4% wordt ingenomen door de harde bollen dan is de evenwichtsfase een vloeistof. Wanneer meer dan 54.5% van het volume wordt ingenomen door de harde bollen dan is de evenwichtsfase een kristal. Dit kristal is een kubisch vlakgecentreerd kristal. Dit houdt in dat het kristal is opgebouwd uit kubussen met deeltjes op de hoekpunten en in het midden van de vlakken.

Vele materialen die we dagelijks tegen komen zijn niet in evenwicht. Honing bijvoorbeeld is vloeibaar wanneer je het koopt, maar wanneer honing een lange tijd in de kast heeft gestaan is de kans groot dat die gekristalliseerd is. Een ander voorbeeld van een materiaal dat niet in evenwicht is, is glas. Glas wordt, wanneer het lang genoeg met rust gelaten wordt, een kwartskristal. Terwijl er heel veel materialen niet in evenwicht zijn, is er niet zo veel bekend over het uiteenwichtgedrag en over waarom sommige materialen heel makkelijk uit evenwicht te brengen zijn en andere erg lastig. Om hier verandering in te brengen, bestuderen we in dit proefschrift hoe harde bollen zich gedragen wanneer ze uit evenwicht worden gebracht.

De eenvoudigste manier om harde bollen uit evenwicht te brengen is om de dichtheid te veranderen. Wanneer door een snelle compressie de dichtheid in korte tijd snel toeneemt tot boven de glasovergangsdichtheid kunnen harde bollen een glas vormen. De glasovergang van harde bollen heeft plaats wanneer ongeveer 58% van het volume wordt ingenomen door de bollen. Een harde-bollenglas ziet er op het eerste gezicht hetzelfde uit als een vloeistof, maar de deeltjes in een glas bewegen nauwelijks. Ze lijken alleen te trillen in een kooi van buurdeeltjes. Wanneer lang genoeg naar een harde-bollenglas gekeken wordt, valt op dat de deeltjes nog wel bewegen, maar dit niet individueel doen: op lange tijdschalen bewegen de deeltjes collectief. Hoe hoger de dichtheid des te groter de groepen deeltjes die collectief bewegen en des te trager het glas stroomt.

In hoofdstuk 2 gebruiken we moleculaire-dynamicsimulaties om de eigenschappen van harde-bollenglazen te bestuderen. We bepalen de druk en zijn afgeleides als functie van de dichtheid. In dit hoofdstuk gebruiken we bollen die niet precies even groot zijn maar een grootteverdeling hebben met een standaarddeviatie van 10% van de diameter. Dit doen we om nucleatie zo goed als onmogelijk te maken. We laten zien dat er een sprong in de afgeleide van de druk zichtbaar is op het moment dat het systeem uit evenwicht valt en een

glas wordt. Een dergelijke sprong is eerder waargenomen voor moleculaire systemen en toont aan dat een dynamische overgang zoals de glasovergang ook een thermodynamische component kan hebben.

Wanneer harde-bollenglazen verder gecomprimeerd worden, blijft de druk toe nemen totdat deze divergeert. Dit gebeurt wanneer de bollen vast komen te zitten doordat ze geen ruimte meer hebben om te bewegen. In hoofdstuk 3 bestuderen wij deze configuraties met hele hoge druk voor verschillende compressiesnelheden en grootteverdelingen van de bollen. We laten zien dat de dichtheid waarop het systeem vast komt te zitten, in tegenstelling tot wat vaak wordt aangenomen, afhankelijk is van de compressiesnelheid.

In hoofdstuk 4 maken we in experimenten met harde bollen configuraties die half uit glas bestaan en half uit kristal. We kijken wat het effect van compressie door zwaartekracht en door elektrische velden is op de fractie deeltjes in een kristallijne omgeving. We laten zien dat de glasovergang en het percentage kristal sterk afhangen van de compressiesnelheid en dat zwaartekracht door zijn extra compressie de glasovergang opschuift.

Het doel van hoofdstuk 5 is om twee verschillende simulatietechnieken om de nucleatiesnelheid uit te rekenen met elkaar te vergelijken. In eerdere studies is er een grote discrepantie tussen de nucleatiesnelheid uit experimenten en uit computer simulaties gevonden. Wij laten zien dat beide simulatietechnieken dezelfde nucleatiesnelheid geven en dat deze overeenkomen met bestaande simulatieresultaten indien deze op de juiste manier worden geschaald.

We hebben in hoofdstuk 6 de nucleatie van een harde-bollenkristal bekeken op een kiem van bollen die door lasers op hun plek werden gehouden. We hebben deze experimenten vergeleken met simulaties en laten zien dat deze goed met elkaar in overeenstemming zijn. We vergelijken de resultaten ook met de voorspellingen van klassieke nucleatietheorie en laten zien die goed werkt voor sommige kiemen maar niet voor andere. Verder laten we zien dat defecten in het kristal een belangrijke rol spelen bij de groei van het kristal.

In hoofdstuk 7 bekijken we een andere manier om harde bollen uit evenwicht te brengen. Ditmaal leggen we een laminaire stroming aan door de twee platen waar de bollen tussen zitten in tegengestelde richting te laten bewegen. We doen experimenten op een dichtheid waarbij de bollen in rust een vloeistof vormen. We laten zien dat er vijf verschillende fasen kunnen ontstaan afhankelijk van de oscillatiesnelheid en amplitude van de platen. Al deze fasen lijken zich te vormen door nucleatie gevolgd door groei.

In hoofdstuk 8 bekijken we de interactie tussen ruwe bollen in de aanwezigheid van polymeren. Polymeren zorgen voor attractie tussen colloïden. Wanneer het oppervlak van de colloïden ruw wordt gemaakt door er kleinere colloïden op te plakken neemt de kracht van de attractie af. Dit werkt optimaal wanneer de kleine colloïden een stuk kleiner zijn dan de grote en wanneer het polymeer nog kleiner is dan de kleine colloïden. We eindigen met het uitrekenen van de attractiesterkte voor het experimentele systeem dat recent is gemaakt door D. Kraft en C. Kats.

Dankwoord

Allereerst wil ik Marjolein bedanken die als dagelijkse begeleider een grote rol heeft gespeeld bij het tot stand komen van dit proefschrift. Als tweede natuurlijk Alfons die als begeleider ook een grote rol heeft gespeeld bij alle experimenten. Ook Arnout wil ik bedanken aangezien hij altijd klaar stond om te helpen; vooral bij de shear-experimenten heb ik veel aan hem gehad.

Johan Stiefelhagen wil ik graag bedanken voor het maken van het grootste deel van de in dit proefschrift gebruikte deeltjes. Zonder hem waren de experimenten met de *dielectrophoretic bottle* en de *shear cell* niet mogelijk geweest. Ook wil ik Johan verder nog bedanken voor alle niet-wetenschappelijke gesprekken en de gezelligheid rondom werktijd.

Mijn kamergenoten: Matthieu Marechal, Andrea Fortini en Djamel el Masri wil ik bedanken voor alle gesprekken over de meest uiteenlopende onderwerpen. Andrea en Matthieu wil ik speciaal bedanken voor de hulp bij mijn eerste simulaties. Matthieu wil ik verder bedanken voor het doorlezen van vele stukken tekst en code.

Dan wil ik graag María Delgado bedanken die eigenlijk onmisbaar en toch te vaak afwezig was de afgelopen 4 jaar.

Esther Vermolen wil ik vooral bedanken voor alle discussies over wetenschap en andere zaken maar ook voor de plezierige samenwerking bij de tweezereperimenten. Mirjam Leunissen wil ik bedanken voor het uitleggen van de methode om *dielectrophoretic bottles* te maken en haar aanstekelijk enthousiasme. Yu Ling Wu wil ik bedanken voor het uitleggen van de werking van de shear cell en hoe aluminiumfolie te gebruiken is om de platen precies parallel te krijgen. Laura Filion wil ik bedanken voor de samenwerkingen over nucleatie en over binaire kristallen maar natuurlijk ook voor alle discussies, het corrigeren van mijn teksten, voor de spelletjes squash, voor de paar dagen vakantie in Zwitserland en voor alle gezelligheid. Teun Vissers wil ik bedanken voor zijn enthousiasme en opgewektheid zelfs wanneer het tegen zat. Verder wil ik Teun bedanken voor het onderzoek met damstenen aan rijvorming. I would like to thank Rao Vutukuri for our work together on making permanent nucleation seeds. Dan wil ik graag Ran Ni en Frank Smalenburg bedanken voor alle discussies over simulaties en nucleatie. Peter Helfferich wil ik bedanken voor het overnemen van alle kleine ict-taken en voor het binnenkort overnemen van de twee linux servers. Peter van Oostrum wil ik bedanken voor het uitlijnen van de tweezers en voor de gezelligheid maar ook voor het samen stoeien met niet-meewerkende camera'software.

Mijn studenten: Marjolein, Tristan en Thijs wil ik graag bedanken voor al het onderzoek dat ze gedaan hebben maar ook voor het enthousiasme waarmee ze hun onderzoek deden en voor de bugs die ze uit mijn codes gehaald hebben.

Dan wil ik ook nog graag de rest van de Soft-Condensed-Mattergroep die ik niet al genoemd heb bedanken voor de fijne samenwerking maar ook voor alle bizarre gesprekken aan de koffietafel en buiten in de zon.

Dan als laatste wil ik graag Eva, Dora en mijn ouders heel erg bedanken voor alles!

Curriculum Vitae

Michiel Hermes was born on the seventh of October in 1980 in Nijmegen. He finished high school at HAVO level in 1998. In 1999, he participated in the high school olympiads for physics and informatics and scored within the top 20 percent of both olympiads. He finished high school at VWO level and started studying physics at Utrecht University in 1999. He performed an experimental bachelor's project in the soft condensed matter group of Alfons van Blaaderen on the self-assembly of binary colloidal crystal of silica colloids. After that he did his master's in theoretical physics at Utrecht University. During his master's, he completed a research project on the phase behavior of charged colloidal rods with Rene van Roij of the theoretical physics group. During his studies he has been an active member of the student campus's internet help desk. In 2006, he started his PhD project with Marjolein Dijkstra and Alfons van Blaaderen in the soft condensed matter group at Utrecht University which resulted in this thesis. During his PhD he has supervised various bachelor and master courses and supervised three master students.